UNIVERSITY OF OKLAHOMA

GRADUATE COLLEGE

SELECTIVE CHELATION OF METAL SPECIES TO FOSSIL PORPHYRINS AND THEIR PALEOENVIRONMENTAL SIGNIFICANCE: INSIGHTS FROM VANADYL, NICKEL, GALLIUM, AND IRON PORPHYRINS DISTRIBUTIONS IN BLACK SHALES

A DISSERTATION

SUBMITTED TO THE GRADUATE FACULTY

in partial fulfillment of the requirements for the

Degree of

DOCTOR OF PHILOSOPHY

By
DEREK RUSSELL PARKS
Norman, Oklahoma
2026

Downloaded from SHAREOK. Persistent Handle URL: https://hdl.handle.net/11244/342505

SELECTIVE CHELATION OF METAL SPECIES TO FOSSIL PORPHYRINS AND THEIR PALEOENVIRONMENTAL SIGNIFICANCE: INSIGHTS FROM VANADYL, NICKEL, GALLIUM, AND IRON PORPHYRINS DISTRIBUTIONS IN BLACK SHALES

A DISSERTATION APPROVED FOR THE

SCHOOL OF GEOSCIENCES

BY THE COMMITTEE CONSISTING OF

Dr. Xiao-Lei Liu, Chair

Dr. Michael H. Engel

Dr. Caitlin Hodges

Dr. Bor-Jier Shiau

© Copyright by Derek Russel Parks 2026
All Rights Reserved.

Abstract

An integrated geochemical investigation of sedimentary porphyrin biomarkers reveals critical insights into metal chelation preferences and their implications for reconstructing paleoenvironmental conditions of black shale deposits. Using reverse-phase liquid chromatography quadrupole time-of-flight mass spectrometry (RPLC-ESI-qTOF-MS), this research examines the distributions of vanadyl (VO), nickel (Ni), gallium (Ga), and iron (Fe) porphyrins in some representative shale sequences, including the late Devonian – early Mississippian Woodford Shale, mid Cretaceous – mid Paleogene Demerara Rise, and the late Cretaceous Eagle Ford Formation. The work identifies a pervasive metal chelation bias, notably VO favoring bicycloalkanoporphyrins (BiCAP) versus Ni complexing with etioporphyrins (Etio), which has the possibility to affect interpretations of the redox-sensitive metal ratios commonly used in paleoenvironmental reconstructions. Further, the study elaborates on the geochemical behavior of gallium and iron porphyrins, explores the geochemical conditions inferred from the occurrence of metalloporphyrins and carotenoids, and expands the understanding of the mechanisms of metalloporphyrin chelation. These findings revise metalloporphyrin based proxies by demonstrating metal and porphyrin chelation selectivity which can potentially affect environmental interpretations of the sedimentary record.

Table of Contents

Abstract ..... **iv**

List of Figures ..... **viii**

List of Tables ..... **x**

Acknowledgements ..... **xi**

Introduction **1**

What is a lipid biomarker? 1

Why study sedimentary porphyrins? 4

What controls the chelation of metal ions in porphyrins? 5

Study novelty, objectives, and outline 7

References 11

Chapter 1 Distributions of vanadyl and nickel porphyrins in the Woodford Shale and selective chelation of metal species by different tetrapyrrole configurations **15**

1.1 Introduction 15

1.2 Materials and Methods 18

1.2.1 Site of study and rock sample preparation 18

1.2.2 Total organic carbon measurements 20

1.2.3 Extraction for lipid biomarker analysis 20

1.2.4 RPLC-ESI-qTOF-MS 21

1.2.5 Lipid biomarker identification and quantification 22

1.3 Results and discussions 23

1.3.1 The occurrence of C_{40} aromatic carotenoids and PZE 23

1.3.2 The distributions of VO- and Ni-porphyrins and redox variation 23

1.3.3 The role of tetrapyrrole configuration and selective metalation 26

1.4 Conclusion 28

1.5 References 29

1.6 Figures 33

1.7 Supplemental 37

Chapter 2 Distribution of Vanadyl and Nickel metalloporphyrins in the OAE-2 Black Shales of Demerara Rise: selective metal chelation across tetrapyrrole configurations and revised VO/(VO+Ni) proxy **39**

2.1 Introduction 39

2.2 Materials and Methods 42
2.2.1 Site of study 42
2.2.2 Lipid Biomarker Extraction 42
2.2.3 LC-ESI-qTOF-MS Analysis 43
2.2.4 Biomarker Identification and Quantification 43
2.3 Results and Discussion 44
2.3.1 C_{40} Aromatic Carotenoids and Photic Zone Euxinia (PZE) 44
2.3.2 Distribution of VO-, Ni- porphyrins 44
2.3.3 Free-Base porphyrin distribution 46
2.3.4 Selective Chelation and Proposed DPEP-focused Ratio 48
2.4 Conclusions 49
2.5 References 50
2.6 Figures 52
2.7 Supplemental 58
Chapter 3 The occurrence of diverse metalloporphyrins in the Eagle Ford and their geochemical significance 59
3.1 Introduction 59
3.2 Materials and Methods 63
3.2.1 Site of study and rock sample preparation 63
3.2.2 Extraction for lipid biomarker analysis 63
3.2.3 RPLC-ESI-qTOF-MS 64
3.2.4 Lipid biomarker identification and quantification 65
3.3 Results and Discussions 66
3.3.1 C_{40} aromatic carotenoids and PZE 66
3.3.2 The distributions of VO- and Ni-porphyrins and redox variation 67
3.3.3 Ga- and Fe-porphyrins 70
3.3.4 Metalloporphyrin relative abundance and the implications 72
3.3.5 Ash bed indications and the biologic response 74
3.4 Conclusions 74
3.5 References 76
3.6 Figures 79

3.7 Supplemental 87
Chapter 4 Integrative discussion of selective bias observed in metalloporphyrin chelation ... **88**
4.1 Introduction 88
4.2 Conceptual Integration 90
4.3 Mechanistic and Structural Implications 92
4.4 Outlook and Future Directions 94
4.5 Summary 96
4.6 References 98
4.7 Figures 100
Concluding Remarks and Future Work **104**

List of Figures

Figure 1.1 The proposed production of BiCAP, DPEP and Etio porphyrins through biological and chemical degradations on chlorophyll-α and heme-b (modified from Kashiyama et al., 2010). 15-OH-lactone-pheophytin-α is one of the major oxidized allomers of chlorophyll-α. Dashed line arrows represent possible, but yet unverified, production of C_{32}-Etios from chlorophylls. The letter 'M' in the molecule represents the metal species, specifically VO and Ni for this study, chelated to porphyrins. 33

Figure 1.2 Extracted ion chromatograms (EICs) show the detection of artificial standards, isorenieratane, paleorenieratane and major VO- and Ni-porphyrins in the Woodford Shale sample, Wch-10 (91.5 ft). (a) Combined EICs of C_{46} GTGT, VO-TPP, Ni-TPP, isorenieratane and paleorenieratane. (b) Combined EICs of 12 major VO-porphyrins detected. (c) Combined EICs of 12 major Ni-porphyrins detected. (d) EICs show the detection of multiple isomers of each VO-porphyrin. $C_{33:1}$-VO-BiCAPs are VO-BiCAPs with an extra unsaturation equivalence, likely the preserved double bond on C3 ethyl group of chlorophyll-α (see molecular structure in Figure 1.1). $C_{33:1}$-Ni-BiCAPs only occur in a few samples with very low abundance, thus are not included in the analysis. (e) EICs show the detection of multiple isomers of each Ni-porphyrin. There are some other VO- and Ni-porphyrins detected in a few specific samples, but not presented and analyzed in this work. 34

Figure 1.3 Depth profiles of the isorenieratane, paleorenieratane, VO- and Ni-porphyrins concentrations and the VO/(VO+Ni) ratio. 35

Figure 1.4 The relative abundance of BiCAP, DPEP and Etio configurations in VO- and Ni-porphyrins. 36

Figure 1.5 Cross plot shows the correlations between VO/Ni and BiCAP/Etio separated into each of the three sections of the Woodford Shale. 36

Figure 2.1 Depth profiles of isorenieratane, VO-, Ni-, and FB-porphyrins concentrations and the VO/(VO+Ni) ratio. 52

Figure 2.2 Extracted ion chromatograms (EICs) show the detection of the artificial standard, isorenieratane, major VO-, Ni-, and FB- porphyrins in the Demerara Rise. Sample 207-1258A 43-2 39-41 was used since it had relatively high curve areas across all measured molecules. (a) Combined EICs of C_{46}GTGT and isorenieratane. (b) Combined EICs of the 15 major VO-porphyrins detected. (c) Combined EICs of the 12 major Ni-porphyrins detected. (d) Combined EICs of the 9 major Free Base(FB)-porphyrins detected. (e) EICs show the detection of multiple isomers of VO-porphyrin. (f) EICs show the detection of multiple isomers of Ni-porphyrin. (g) EICs show the detection of multiple isomers of FB-porphyrin. 53

Figure 2.3 The relative abundance of BiCAP, DEPE, and Etio configurations in VO-, Ni-, and FB-porphyrins. 54

Figure 2.4 Cross plot show the correlations between VO/Ni and BiCAP/Etio for the Demerara Rise separated into the three sections pre- during and post- OAE-2 in the Demerara Rise. 55

Figure 2.5 VO/(VO+Ni) ratios for both total porphyrin and DPEP porphyrin for the Woodford Shale and Demerara Rise 56

Figure 2.6 Cross plot shows the correlation between the VO/(VO+Ni) ratio and the DPEP VO/(VO+Ni) ratio for the Demerara Rise. 57

Figure 3.1 Map of Texas showing the locations for the Shell Iona-1 and USGS Gulf Coast-3 (GC-3) cores overlayed on the Eagle Ford Shale outcrop..... 79

Figure 3.2 Extracted ion chromatograms (EICs) show the detection of artificial standards, isorenieratane, major VO-, Ni-, Ga- and Fe- porphyrins in the Eagle ford. The artificial standards and isorenieratane used sample EF022, VO- and Ni- porphyrins used sample EF025, Ga-porphyrins used sample EF012, and Fe-porphyrins used sample EF004. (a) Combined EICs of C_{46} GTGT, VO-TPP, Ni-TPP, and isorenieratane. (b) Combined EICs of the 14 major VO-porphyrins detected. (c) Combined EICs of the 12 major Ni-porphyrins detected. (d) Combined EICs of the 6 major Ga-porphyrins detected. (e) Combined EICs of the 14 major Fe-porphyrins detected. (f) EICs show the detection of multiple isomers of VO-porphyrins. (g) EICs show the detection of multiple isomers of Ni-porphyrin. (h) EICs show the detection of multiple isomers of Ga-porphyrins. (i) EICs show the detection of multiple isomers of Fe-porphyrin..... 81

Figure 3.3 Depth profiles of Isorenieratane (with a zoom in to see OAE-2 easier), VO-porphyrin, Ni-porphyrin, Ga-porphyrin, Fe-porphyrin, the VO/(VO+Ni) ratio, and total porphyrin. TOC wt%, δ^{13} OM%, and Pr/Ph ratios are data sourced from (French et al., 2024)..... 82

Figure 3.4 Depth profiles of C_{32}-Etio derived from the degradation of heme-b and the C_{32}Etio(heme)/total porphyrin ratio. 83

Figure 3.5 Depth profiles of Fe-porphyrin, the S/Fe ratio (French et al., 2024), the Fe-BiCAP/Fe-porphyrin ratio, and the VO/(VO+Ni) ratio. The dotted line on the S/Fe ratio represents the pyrite ratio at 1.15 where pyrite is formed..... 84

Figure 3.6 The relative abundance of BiCAP, DPEP, and Etio configurations for VO-, Ni-, Ga-, and Fe-porphyrins. 85

Figure 3.7 Depth profiles of the TOC wt% (French et al., 2024) and Fe-porphyrin with reported ash beds marked by orange lines..... 86

Figure 4.1 Relative percent of vanadyl (VO) and nickel (Ni) porphyrin for A) the Woodford Shale, B) the Demerara Rise, and C) the Eagle Ford. 100

Figure 4.2 Cross plots showing the relationship between the VO/Ni ratio and the BiCAP/Etio ratio for A) the Woodford Shale, B) the Demerara Rise, C) the Eagle Ford, and D) the Eagle Ford with samples EF001 (64ft)-EF012 (140ft), EF021 (206ft), and EF024 (206ft) removed. 101

Figure 4.3 Relative percent of all metalloporphyrins detected in the Eagle Ford consisting of iron (Fe), gallium (Ga), vanadyl (VO), and nickel (Ni). 102

Figure 4.4 Shows the stick structure of Ni-Etio and VO-BiCAP and the theoretical structure of Ni-Etio and the structure of VO chelated to a simple porphyrin (Munoz et al., 2019). 102

Figure 4.5 General structures and labeled rings for BiCAP, DPEP, and Etio 103

List of Tables

Supplementary 1.1 Depth profiles of isorenieratane and paleorenieratane show the consistency of data produced by LC-MS (this work) and GC-MS (Connock et al., 2018). 37

Supplementary 1.2 The raw data of depth profiles presented in Figure 1.3. 38

Supplementary 2.1 The raw data of depth profiles presented in Figure 2.1. 58

Supplementary 3.1 The raw data of depth profiles presented in Figure 3.3 87

Acknowledgements

I would like to express my gratitude to my advisor, Dr. Xiao-Lei Liu, for everything he has done for me for the past seven years. You have shown incredible guidance, mentorship, and support to me during my time working with you. You helped push me past imposter syndrome by often deferring to me on topics of chemistry and supporting my analysis of our investigated proxies through the lens of my chemistry background. The collaborative relationship you fostered has been invaluable and has shaped me into a better scientist. Thank you.

I would also like to thank Dr. Michael Engel for his help pushes I sometimes needed. I actively looked forward to running into you in the hallways of Sarkeys for nothing more than our talks. You showed real interest in my progress as well as are able to talk at great length on a variety of topics I find incredibly interesting. It is unfortunate that these talks will no longer be possible after I am gone.

I also greatly appreciate my committee members Dr. Caitlin Hodges and Dr. Bor-Jier Shiau for agreeing to serve on my committee. Dr. Hodges, I greatly enjoyed your class and apologize for often getting side tracked on disparate topics, thank you for entertaining them while still guiding me to learn. Dr. Shiau I realize you were a late addition to the committee but thank you for agreeing to join the committee on such short notice.

I would like to thank Dr. Katherine French for providing the Eagle Ford samples we examined. You saw my interest in my work at the GRC and graciously sent me samples that I needed to expand my work. Additionally, the help you provided in understanding the setting of these samples was instrumental in the conclusions we were able to produce with them.

Thank you to Dr. Greggory Connock for his guidance in the lab during my Masters and for providing the data utilized for the Demerara Rise. The guidance allowed me to operate effectively in the lab without which I would not have had the excellent data that I now have. The data you provided on the Demerara Rise also allowed me to more effectively back up the claims I made in the way VO and Ni porphyrins chelate.

I extend my appreciation to Dr. Olawale Alo, Chenxi Xu, Fred Zhao, and Junpeng Fu for our conversations both professional and outside of academics. You were instrumental to be able to bounce ideas off during group meetings as well as keeping burn out away when taking breaks to have random conversations in the office.

The geology department at OU is also deserving of my gratitude. The generosity in providing funding and scholarships for my research allowed for my academic life and research to be possible. I would also like to thank the office staff on the 7th floor especially Rebecca Fay for always cheerfully aiding with anything I needed no matter how trivial the question.

I very much appreciate the constant support provided by my family. They have encouraged my interests in science and especially geology from a young age. They have pushed me to achieve this illustrious level of academia by always supporting me and my ambitions. Their love and moral support has kept me driven to achieve this goal, I am forever grateful.

Finally, I would like to thank my fiancé, Amy Pham. She has provided emotional and moral support through all these years. The distance we have endured during this time will always be difficult but you have always been there for me and made time to support me.

My deepest appreciation to you all.

Introduction

What is lipid biomarker

Understanding the environmental proxies preserved in sedimentary rocks provides a crucial foundation for addressing modern challenges related to environmental change and ecosystem resilience. Evidence from the geological record offers a framework for anticipating present-day environmental dynamics by identifying patterns documented in Earth's history (Smith and McGowan, 2011; Naresh, 2024; Turner et al., 2025). Although future conditions will not replicate the past exactly, the geological record remains our most reliable basis for evaluating potential trajectories of change. Geologists integrate proxy data with stratigraphic and environmental context to reconstruct both past and ongoing environmental transitions. These proxies are indispensable tools for paleoenvironmental reconstruction and for assessing potential future impacts. Accordingly, rigorous interpretation of proxy records and a clear understanding of the mechanisms that govern their formation, preservation, and alteration are essential. Misinterpretation or incomplete mechanistic understanding can lead to biased reconstructions or inaccurate predictions. This work focuses on the processes controlling the preservation and interpretation of geochemical proxies derived from microbial life, commonly referred to as biomarkers.

Biomarkers are complex organic molecules derived from specific biological precursors that become preserved in sediments and petroleum systems, providing a molecular record of past organisms and depositional environments. After burial, these compounds undergo diagenesis, which alters their original molecular structures while typically preserving diagnostic

features that reflect their biological origins (Volkman, 1988; Peters and Moldowan, 1993; Eganhouse, 1997). Despite subsequent diagenesis, biodegradation, and catagenesis, many biomarkers retain characteristic molecular motifs linked to the metabolic pathways of their source organisms, making them powerful tools for reconstructing ancient ecosystems and environmental conditions (Peters and Moldowan, 1993).

Lipid biomarkers represent a subset of biomarkers derived specifically from biological lipids, including fatty acids, phospholipids, sphingolipids, and sterols. Lipids are amphipathic compounds characterized by a polar head group and a nonpolar hydrocarbon tail, functioning in energy storage, membrane structure, and cellular signaling. The preservation of lipid-derived molecular frameworks enables differentiation among biological inputs from bacteria, algae, vascular plants, and animals. This molecular specificity allows reconstruction of interactions among the biosphere, geosphere, atmosphere, and hydrosphere, thereby improving our understanding of past environmental and climatic dynamics (Brassell et al., 1986; Brocks and Summons, 2003; Luo et al., 2019). Lipid biomarkers are preferentially preserved in anoxic depositional environments, where limited oxygen availability suppresses oxidative degradation and microbial remineralization, enhancing long-term preservation in the geological record (Sinninghe Damsté et al., 2002). Consequently, lipid biomarker analysis provides critical insights into paleoenvironments, sediment provenance, diagenetic processes, thermal maturity, and biodegradation histories.

This study examines several key lipid biomarkers, beginning with the carotenoid-derived hydrocarbon isorenieratane. Carotenoids are pigments synthesized by diverse photosynthetic organisms (Hartgers et al., 1994). Isorenieratane is a diagenetic derivative of isorenieratene and

is taxonomically linked to members of the family Chlorobiaceae (Koopmans et al., 1996), commonly known as green sulfur bacteria (GSB). The GSB are obligate phototrophic, strictly anaerobic autotrophs that utilize hydrogen sulfide (H_2S) as an electron donor (Van Gemerden, 1983; Frigaard and Bryant, 2004; Frigaard et al., 2004). They synthesize distinctive carotenoids including isorenieratene, chlorobactene, and paleorenieratane and possess specialized light-harvesting organelles (chlorosomes) containing bacteriochlorophylls c, d, and e (Hartgers et al., 1994; Koopmans et al., 1996; Frigaard and Bryant, 2004; French et al., 2015). Isorenieratane forms through hydrogenation of isorenieratene double bonds during diagenesis (Hartgers et al., 1994). Because GSB inhabit sulfide-rich zones within the photic zone, the occurrence of their diagnostic carotenoid derivatives such as isorenieratane, chlorobactane, and paleorenieratane serve as strong evidence for photic zone euxinia.

Another major biomarker class investigated in this study is metalloporphyrins. Although their biological precursor, chlorophyll, is not a lipid, it exhibits lipid-like behavior due to its amphipathic structure, consisting of a hydrophobic phytol tail and a polar porphyrin ring. During diagenesis, the central magnesium ion of chlorophyll can be replaced by transition metals such as nickel or vanadium, forming metalloporphyrins that are commonly preserved in sediments and crude oils. These compounds retain structural elements of their biological precursors and provide valuable information about primary productivity, redox conditions, and depositional environments.

Why study sedimentary porphyrins?

Porphyrins were the first biomarkers identified in sedimentary organic matter by Treibs (1936). These tetrapyrrolic macrocycles, derived primarily from chlorophylls, bacteriochlorophylls, and hemes, undergo a series of diagenetic transformations that yield geoporphyrins that fall into three structural classes, bicycloalkanoporphyrins (BiCAP), deoxophylloerythroetioporphyrin (DPEP), and etioporphyrin (Etio) (Huseby et al., 1996; Turner, 1998; Callot and Ocampo, 2000; Stuart Walker and Keely, 2004). These compounds are remarkably stable and can persist through geologic time scales in sediments, fossil fuels, and sedimentary rocks being detectable for up to 1.1 billion years (Gueneli et al., 2018). Their enduring chemical structure allows them to act as molecular fossils, providing insights into the biological sources, depositional environments and diagenetic processes affecting ancient organic matter in geological systems (Tahoun et al., 2021).

In geology, porphyrins help trace the biological origins of petroleum and fossil fuels through the preservation of metal-porphyrin complexes, such as nickel and vanadyl porphyrins, which serve as fossil molecular fingerprints indicating specific chlorophyll precursors (Quirke et al., 1979). The study of these fossil porphyrins contributes to organic geochemistry by revealing the pathways of transformation from biomass of living organisms to sedimentary organic matter, aiding in reconstructing paleoenvironmental conditions and the evolution of Earth's biosphere.

Porphyrins, as molecular fossils derived from chlorophyll, serve as geochemical indicators for reconstructing historical primary productivity in sedimentary environments

(Gueneli et al., 2018). These tetrapyrrolic macrocycles persist in ancient sediments due to their chemical stability and can be detected in a wide range of geologic settings, providing a direct molecular record of the abundance and activity of photosynthetic organisms at the time of deposition. Their elevated concentrations in sediment are interpreted to reflect intervals of enhanced primary productivity by phytoplankton and other photosynthetic primary producers that produced the parent chlorophyll molecule (Callot et al., 1990; Huseby et al., 1996).

Porphyrins are also instrumental in recording information about their depositional environment. They provide data on depositional redox conditions (Callot et al., 1990), biogeochemical cycling of metals (Elderfield et al., 1985), and the interactions between organic molecules and mineral matrices (De et al., 2023), offering an unparalleled window into the environmental dynamics that shaped ancient ecosystems. Their distribution and structural modification through geologic time make them vital contributors to the toolkit of geochemical proxies, with each preservation or alteration recording a signature of the prevailing environmental conditions.

What controls the chelation of metal ions in porphyrins

Porphyrins lose the magnesium metal at the center of the chlorophyll. They are then free base porphyrins and have the potential to chelate to many different transition metals with a 2+ charge. These transition metals they can complex to include Fe^{2+}, Ga^{2+}, Cu^{2+}, Mn^{2+}, Co^{2+}, Ti^{2+}, Zn^{2+}, V^{2+}(as vanadyl, VO^{2+}), and Ni^{2+} (Callot and Ocampo, 2000; Junium et al., 2008; Woltering et al., 2016). This wide range of metals makes them exceptionally valuable for

reconstructing paleoredox states, depositional chemistry, and organic matter provenance. Variations in metal coordination and molecular structure record the interplay among biological production, water-column redox gradients, and post-depositional alteration.

Metal chelation by porphyrins is governed by a combination of chemical and environmental factors. One primary control is the availability of metal ions in the surrounding medium. The concentration of a given metal directly influences its likelihood of incorporation into the porphyrin macrocycle. Metals present at higher concentrations are more likely to form stable complexes than those available in trace amounts (Falk, 1964). Another important factor is the kinetics of metal insertion. Metals that insert rapidly into the tetrapyrrole ring can outcompete those with slower insertion rates under similar conditions (Lipiner et al., 1988; Funahashi et al., 2001; Shen and Ryde, 2005). The thermodynamic stability of the resultant metalloporphyrin complex also plays a critical role, as more stable metal-nitrogen coordination bonds favor persistence during diagenetic and catagenetic processes (Baker and Louda, 1986; Büchner et al., 2021). Although individual metal-nitrogen bonds are relatively weak, being π bonds, the cumulative coordination of four nitrogen donors provides substantial chelation stability within the planar macrocycle. Finally, the ionic radius of the metal ions determines how well it fits within the porphyrin cavity. Mismatched ionic sizes can lead to steric strain or insufficient coordination, reducing complex stability (Kingsbury and Senge, 2021).

A ratio of vanadyl-to-nickel in geoporphyrins (VO/(VO+Ni)) has been widely employed as a proxy for assessing depositional redox conditions in sedimentary environments. High VO/(VO+Ni) ratios (>0.50) with elevated sulfur (>1 wt%), are typically interpreted to indicate anoxic or euxinic depositional settings, whereas lower ratios (<0.50) are indicative of more

oxygenated conditions (Lewan and Maynard, 1982; Lewan, 1984). This proxy relies on the geochemical behavior of Ni^{2+}, which precipitates as nickel sulfide under euxinic conditions, thereby increasing the relative abundance of VO^{2+} complexed within the porphyrin fraction (Lewan and Maynard, 1982; Lewan, 1984; Huseby et al., 1996; Junium et al., 2008, 2015). However, studies have demonstrated that there is a differential chelation, or selectivity, between VO and Ni for specific porphyrin structures BiCAP and Etio, respectively, potentially biasing redox interpretations based on this ratio (Sundararaman and Boreham, 1993). Despite the observation of this selective chelation effect, the mechanism and quantitative impact remain poorly understood. The present study addresses these uncertainties by systematically evaluating chelation selectivity in sedimentary porphyrins and proposing revised approaches to improve the proxy's robustness in reconstructing paleoredox conditions.

Study novelty, objectives, and outline

The chapters in this work were developed using a novel analytical approach introduced by Liu (2023). This technique integrates reverse phase liquid chromatography – electrospray ionization – quadrupole time-of-flight – mass spectrometry (RPLC-ESI-qTOF-MS) to enable rapid detection and quantification of large, often polar organic molecules that have proven challenging to analyze using traditional GC-MS methodologies. This advancement in detection sensitivity and chromatographic resolution has enabled the detailed characterization of distinct porphyrin classes and other large organic molecules, facilitating lines of investigation that were

previously inaccessible. This resolution has been important when investigating geoporphyrins since the different classes are formed through different diagenetic pathways.

The initial objective of this study was to explore the changes in detected geoporphyrins in black shales and report them at a resolution previously incapable. Quickly though an issue was discovered when investigating the geoporphyrins and their chelated metals. In the Woodford Shale (see chapter 1) only vanadyl and nickel porphyrins are detected, when exploring the relationship of the metals and their associated porphyrins, a bias in chelation was observed. Vanadyl seemed to have an affinity to chelating to BiCAP and did not chelate to Etio in large quantities whereas nickel was the inverse; it chelated to Etio in greater quantities than it did to BiCAP. This discovery had been previously reported (Sundararaman and Boreham, 1993) but not explained or validated so this set us on the path to determine if this purported chelation bias was consistent in multiple black shale members or was unique to the Woodford Shale. Understanding the association between the metals and the geoporphyrins was important since each class of porphyrin is produced through a different pathway and if the metals that chelate to them are used as a proxy for redox that proxy has the potential to be influenced by processes creating the geoporphyrins. The key questions were:

1. What is the depositional context of metalloporphyrins, and to what extent does the VO/(VO+Ni) ratio serve as a robust indicator of redox conditions when compared with other established geochemical proxies?
2. How do different depositional settings and redox conditions influence the observed bias in chelation?

3. Is the application of metalloporphyrins as a proxy valid, despite the discovered chelation bias?

Chapter 1 investigates the distribution of vanadyl (VO) and nickel (Ni) porphyrins in the Woodford Shale spanning the late Devonian to early-Mississippian, highlighting the discovery of a chelation bias in which VO preferentially complexes with BiCAP structures, whereas Ni more commonly associates with Etio configurations. This study validates the application of the novel RPLC-ESI-qTOF-MS analytical method for the rapid and sensitive detection of metalloporphyrins and carotenoids extracted from black shales. Furthermore, it explores the relationship between the VO/Ni metalation ratio and the BiCAP/Etio structural ratio, demonstrating that selective metal chelation based on porphyrin molecular configuration significantly influences metalloporphyrin distributions. These findings emphasize that both metal availability and tetrapyrrole structure govern the observed chelation patterns, providing crucial insights for using metalloporphyrins as proxies for paleoenvironmental redox conditions and biological processes in sedimentary systems.

Chapter 2 examines the distribution of vanadyl (VO) and nickel (Ni) porphyrins in the Demerara Rise black shales spanning the mid-Cretaceous to mid-Paleogene, including the Oceanic Anoxic Event 2 (OAE-2). Using the same RPLC-ESI-qTOF-MS method, this study confirms the selective chelation bias first observed in the Woodford Shale, where vanadyl preferentially complexes with BiCAP porphyrins and nickel associates more with Etio porphyrins. Recognizing the limitations this bias imposes on traditional VO/Ni ratios as paleoredox proxies, Chapter 2 proposes a refined VO/Ni ratio focused exclusively on the DPEP porphyrin class, which is

expected to minimize chelation bias an improve the sensitivity of redox reconstructions in euxinic black shale settings.

Chapter 3 examines the distribution of multiple metalloporphyrin species in the Eagle Ford Formation, a late Cretaceous black shale sequence from the Western Interior Seaway of North America deposited under variable redox conditions. In addition to vanadyl and nickel porphyrins gallium and iron porphyrins were also detected. The VO/Ni chelation bias is observed here along with selective chelation between gallium and iron and associated porphyrin classes. This chapter aims to assess if redox conditions play a role in the observed chelation bias of vanadyl and nickel porphyrins as well as recording other metalloporphyrins detected in the Eagle Ford.

Chapter 4 compares the findings from preceding chapters to provide a unified interpretation of the geochemical and paleoenvironmental significance of porphyrin and biomarker distributions across the Woodford Shale, Demerara Rise, and Eagle Ford Formation. This chapter integrates data on vanadyl and nickel porphyrins to evaluate the influence of depositional redox conditions, diagenetic processes, and organic matter sources on biomarker signatures in marine black shales. It highlights the importance of selective metal chelation and structural diversity in shaping metalloporphyrin distributions and demonstrates how refined analytical approaches can improve paleoredox reconstructions. It explores how other metalloporphyrins or even unchelated free base porphyrins can obscure the relationship of the chelation bias despite the bias being visually obvious. It also describes the structural mechanism proposed to explain the chelation bias.

References

Baker, E.W., Louda, J.W., 1986. Porphyrins in the geological record, in: Johns, R.B. (Ed.), Biological Markers in the Sedimentary Record. Elsevier, pp. 125–225.

Brassell, S.C., Eglinton, G., Marlowe, I.T., Pflaumann, U., Sarnthein, M., 1986. Molecular stratigraphy: a new tool for climatic assessment. Nature 320, 129–133.

Brocks, J., Summons, R., 2003. Sedimentary Hydrocarbons, Biomarkers for Early Life. Treatise on Geochemistry 8, 63–115.

Büchner, R., Fondell, M., Haverkamp, R., Pietzsch, A., Cruz, V.V. da, Föhlisch, A., 2021. The porphyrin center as a regulator for metal–ligand covalency and π hybridization in the entire molecule. Physical Chemistry Chemical Physics 23, 24765–24772.

Callot, H.J., Ocampo, R., 2000. Geochemistry of Porphyrins. The Porphyrin Handbook, Academic Press.

Callot, H.J., Ocampo, R., Albrecht, P., 1990. Sedimentary porphyrins: correlations with biological precursors. Energy & Fuels 4, 635–639.

De, S., Mouchaham, G., Liu, F., Affram, M., Abeykoon, B., Guillou, N., Jeanneau, E., Grenèche, J.-M., Khrouz, L., Martineau-Corcos, C., Boudjema, L., Salles, F., Salcedo-Abraira, P., Valente, G., Souto, M., Fateeva, A., Devic, T., 2023. Expanding the horizons of porphyrin metal–organic frameworks via catecholate coordination: exploring structural diversity, material stability and redox properties. Journal of Materials Chemistry A 11, 25465–25483.

Eganhouse, R.P., 1997. Molecular Markers and Environmental Organic Geochemistry: An Overview, in: Molecular Markers in Environmental Geochemistry, ACS Symposium Series. American Chemical Society, pp. 1–20.

Elderfield, H., Mackenzie, A.S., Berner, R.A., Meadows, P.S., Jones, J.G., Clemmey, H., Murchison, D.G., Durand, B., Eglinton, G., Sarnthein, M., 1985. Element Cycling in Bottom Sediments [and Discussion]. Philosophical Transactions of the Royal Society of London. Series A, Mathematical and Physical Sciences 315, 19–23.

Falk, J.E., 1964. Porphyrins and Metalloporphyrins: Their General, Physical and Coordination Chemistry, and Laboratory Methods. Elsevier Publishing Company.

French, K.L., Rocher, D., Zumberge, J.E., Summons, R.E., 2015. Assessing the distribution of sedimentary C40 carotenoids through time. Geobiology 13, 139–151.

Frigaard, N.-U., Bryant, D.A., 2004. Seeing green bacteria in a new light: genomics-enabled studies of the photosynthetic apparatus in green sulfur bacteria and filamentous anoxygenic phototrophic bacteria. Archives of Microbiology 182, 265–276.

Frigaard, N.-U., Maresca, J.A., Yunker, C.E., Jones, A.D., Bryant, D.A., 2004. Genetic Manipulation of Carotenoid Biosynthesis in the Green Sulfur Bacterium Chlorobium tepidum. Journal of Bacteriology 186, 5210–5220.

Funahashi, S., Inada, Y., Inamo, M., 2001. Dynamic Study of Metal-Ion Incorporation into Porphyrins Based on the Dynamic Characterization of Metal Ions and on Sitting-Atop Complex Formation. Analytical Sciences 17, 917–927.

Gueneli, N., McKenna, A.M., Ohkouchi, N., Boreham, C.J., Beghin, J., Javaux, E.J., Brocks, J.J., 2018. 1.1-billion-year-old porphyrins establish a marine ecosystem dominated by bacterial primary producers. Proceedings of the National Academy of Sciences 115, E6978–E6986.

Hartgers, W.A., Sinninghe Damsté, J.S., Requejo, A.G., Allan, J., Hayes, J.M., Ling, Y., Xie, T.-M., Primack, J., de Leeuw, J.W., 1994. A molecular and carbon isotopic study towards the origin and diagenetic fate of diaromatic carotenoids. Organic Geochemistry 22, 703–725.

Huseby, B., Barth, T., Ocampo, R., 1996. Porphyrins in Upper Jurassic source rocks and correlations with other source rock descriptors. Organic Geochemistry, Organic Geochemistry 25, 273–294.

Junium, C.K., Freeman, K.H., Arthur, M.A., 2015. Controls on the stratigraphic distribution and nitrogen isotopic composition of zinc, vanadyl and free base porphyrins through Oceanic Anoxic Event 2 at Demerara Rise. Organic Geochemistry 80, 60–71.

Junium, C.K., Mawson, D.H., Arthur, M.A., Freeman, K.H., Keely, B.J., 2008. Unexpected occurrence and significance of zinc alkyl porphyrins in Cenomanian–Turonian black shales of the Demerara Rise. Organic Geochemistry, Advances in Organic Geochemistry 2007 39, 1081–1087.

Kingsbury, C.J., Senge, M.O., 2021. The shape of porphyrins. Coordination Chemistry Reviews 431, 213760.

Koopmans, M.P., Köster, J., Van Kaam-Peters, H.M.E., Kenig, F., Schouten, S., Hartgers, W.A., de Leeuw, J.W., Sinninghe Damsté, J.S., 1996. Diagenetic and catagenetic products of isorenieratene: Molecular indicators for photic zone anoxia. Geochimica et Cosmochimica Acta 60, 4467–4496.

Lewan, M.D., 1984. Factors controlling the proportionality of vanadium to nickel in crude oils. Geochimica et Cosmochimica Acta 48, 2231–2238.

Lewan, M.D., Maynard, J.B., 1982. Factors controlling enrichment of vanadium and nickel in the bitumen of organic sedimentary rocks. Geochimica et Cosmochimica Acta 46, 2547–2560.

Lipiner, G., Willner, I., Aizenshtat, Z., 1988. Correlation between geochemical environments and controlling factors in the metallation of porphyrins. Organic Geochemistry, Proceedings of the 13th International Meeting on Organic Geochemistry 13, 747–756.

Liu, X.-L., 2023. Collision-induced dissociation as “mass spectrometric filter” for rapid screening of tetrapyrrole derivatives and their chelated metal species in complex biological and environmental samples. Rapid Communications in Mass Spectrometry 37, e9413.

Luo, G., Yang, H., Algeo, T.J., Hallmann, C., Xie, S., 2019. Lipid biomarkers for the reconstruction of deep-time environmental conditions. Earth-Science Reviews, Sedimentology as a Key to Understanding Earth and Life Processes 189, 99–124.

Naresh, P., 2024. Sedimentary Stories: How Rock Layers Reveal Earth's Past. Journal of Earth Science & Climatic Change 15, 1–3.

Peters, K.E. (Kenneth E., Moldowan, J.M., 1993. The biomarker guide : interpreting molecular fossils in petroleum and ancient sediments. Englewood Cliffs, N.J. : Prentice Hall.

Quirke, J.M.E., Eglinton, G., Maxwell, J.R., 1979. Petroporphyrins. 1. Preliminary characterization of the porphyrins of gilsonite. Journal of the American Chemical Society 101, 7693–7697.

Shen, Y., Ryde, U., 2005. Reaction mechanism of porphyrin metallation studied by theoretical methods. Chemistry (Weinheim an Der Bergstrasse, Germany) 11, 1549–1564.

Sinninghe Damsté, J.S., Rijpstra, W.I.C., Reichart, G., 2002. The influence of oxic degradation on the sedimentary biomarker record II. Evidence from Arabian Sea sediments. Geochimica et Cosmochimica Acta 66, 2737–2754.

Smith, A.B., McGowan, A.J., 2011. The ties linking rock and fossil records and why they are important for palaeobiodiversity studies. Geological Society, London, Special Publications 358, 1–7.

Stuart Walker, J., Keely, B.J., 2004. Distribution and significance of chlorophyll derivatives and oxidation products during the spring phytoplankton bloom in the Celtic Sea April 2002. Organic Geochemistry, Advances in Organic Geochemistry 2003. Proceedings of the 21st International Meeting on Organic Geochemistry 35, 1289–1298.

Sundararaman, P., Boreham, C.J., 1993. Comparison of nickel and vanadyl porphyrin distributions of sediments. Geochimica et Cosmochimica Acta 57, 1367–1377.

Tahoun, M., Gee, C.T., McCoy, V.E., Sander, P.M., Müller, C.E., 2021. Chemistry of porphyrins in fossil plants and animals. RSC Advances 11, 7552–7563.

Treibs, A., 1936. Chlorophyll- und Häminderivate in organischen Mineralstoffen. Angewandte Chemie.

Turner, A., 1998. Recognition of photic zone anoxia from LC-MS studies of porphyrin distributions in ancient sediments (Doctoral dissertation). University of Bristol, Bristol, UK.

Turner, M.L., Khan, S.Y., Lewis, K.W., Noblet, A., Kite, E.S., 2025. Early thinning, late persistence, diachronous boundaries, and a regional dichotomy in Mars' young sedimentary rocks. Communications Earth & Environment 6, 869.

Van Gemerden, H., 1983. Physiological ecology of purple and green bacteria. Annales de l'Institut Pasteur / Microbiologie 134, 73–92.

Volkman, J., 1988. Biological marker compounds as indicators of the depositional environments of petroleum source rocks. Geological Society of London Special Publications 40, 103–122.

Woltering, M., Tulipani, S., Boreham, C.J., Walshe, J., Schwark, L., Grice, K., 2016. Simultaneous quantitative analysis of Ni, VO, Cu, Zn and Mn geoporphyrins by liquid chromatography-high resolution multistage mass spectrometry: Method development and validation. Chemical Geology 441, 81–91.

Chapter 1 The distribution of vanadyl and nickel porphyrins in Woodford Shale and a selective chelation of metal species to different tetrapyrrole configurations

Authors: Derek Parks[1*], Xiao-Lei Liu[1]

Affiliations: [1]School of Geosciences, University of Oklahoma, Norman, Oklahoma 73019, USA.

Published in Organic Geochemistry, 2023

https://doi.org/10.1016/j.orggeochem.2023.104693

Abstract: Abundant vanadyl (VO) and nickel (Ni) porphyrins were detected in the Late Devonian–Early Mississippian Woodford formation shales using a recently developed reverse-phase liquid chromatography quadrupole time-of-flight mass spectrometry with electrospray ionization (RPLC-ESI-qTOF-MS). This Woodford shale sequence is characterized by the presence of sustained photic zone euxinia (PZE), as indicated by the occurrence of green sulfur bacteria-produced isorenieratane. The distribution of VO- and Ni-porphyrins, expressed as the VO/(VO+Ni) ratio, reflects a generally reducing/sulfidic condition throughout most of the Woodford deposition. However, in the later Upper Woodford, there is a significant drop in the VO/(VO+Ni) ratio, marking the collapse of anoxia/euxinia due to gradual oxygenation. All three categories of porphyrin structures, namely bicycloalkanoporphyrin (BiCAP), deoxophylloerythroethioporphyrin (DPEP), and etioporphyrin (Etio), occurred in VO- and Ni-porphyrins. VO exhibits a preferential chelation to BiCAP over the other two types of porphyrins. In contrast, Ni-porphyrins are predominantly composed of Etio structures. Due to such selective binding of metal species to specific porphyrin structures, the relative abundance of VO- and Ni-porphyrins (VO/(VO+Ni)) exhibits a strong logarithmic correlation (R^2=0.83) with the proportion of BiCAP to other structures (BiCAP/(BiCAP+DPEP+Etio)). These findings suggest that the distribution of VO- and Ni-porphyrins in sediments is not solely controlled by the availability of metal ions. Further investigations into the influence of biological and chemical processes on the composition of BiCAP and ETIO are crucial and warrant future research endeavors.

1.1 Introduction

Sedimentary porphyrins, or so called geoporphyrins, were the first set of biomarkers identified in petroleum organic matter (Treibs, 1936). Geoporphyrins are degradation products of chlorophyll, bacteriochlorophylls, and hemes, with three major structural classes (Figure 1.1), BiCAP, DPEP, and Etio, occurring in nature (Callot and Ocampo, 2000; David, 1998; Huseby et al., 1996; Stuart Walker and Keely, 2004). Generally, these geoporphyrin molecules are formed

when chlorophylls, the precursor molecules, lose their chelated magnesium and ester-bonded isoprenoids, and some functionalized side chains, such as vinyl, hydroxyethyl, and acetyl groups, are cleaved or reduced in the environment. Further diagenesis can cause dealkylation of the cyclic tetrapyrrole core and result in porphyrins with less carbon (Callot and Ocampo, 2000). Specifically, it is believed that grazing of phytoplankton by herbivorous organisms initiates the production of tetrapyrroles with the BiCAP structure. This is supported by the discovery of cyclopheophorbide-an-enol in fecal pellets of benthic macro-invertebrates and planktonic protists (Goericke et al., 2000; Kashiyama et al., 2012). Although the DPEP series is commonly considered as the direct degradation product of chlorophylls through diagenesis (the Treibs scheme, see discussion in Keely et al., 1990), biological alteration of chlorophylls through grazing by zooplanktons could also contribute DPEP in sediment. Chlorophyll pyro-derivatives, such as pyropheophytin and pyropheophorbide, which have a tetrapyrrole core resembling the DPEP structure, have been identified as the most common products of grazing when the carboxy methyl ester group at the C_{13} position of the E ring of chlorophylls (Figure 1.1) is cleaved (Nguyen et al., 2022; Itoh et al., 2007). Etio porphyrins, lacking both the E and F rings (Figure 1.1), especially for those with less than 32 carbons, are mainly derived from the chlorophyll allomers (Naylor and Keely, 1998; Louda et al., 1998; 2000; 2011) formed by oxidation of chlorophylls through either chemical (Walker et al., 2003) or biological (Maroneze et al., 2019) processes. However, the distinct isotope composition of C_{32} Etio compared to other porphyrins in various deposits suggests a predominant contribution of C_{32} Etio from heme rather than chlorophyll degradation (Boreham et al., 1989; Ocampo et al., 1989).

Metalation of geoporphyrins leads to the formation of metalloporphyrins, a diagenetic process occurring after deposition. The production of metalloporphyrins during early diagenesis depends on the availability of metals in the surrounding sediments (Huseby et al., 1996; Junium et al., 2008, 2015). After a free based porphyrin complexes with a metal, the porphyrin macrocyclic core is flattened, significantly reducing its reactivity and making it geologically stable (Junium et al., 2015). Free based geoporphyrins can chelate various metal ions in sediment, including Fe, Ga, Cu, Mn, Co, Ti, Zn, V, and Ni (Callot and Ocampo, 2000; Junium et al., 2008; Woltering et al., 2016). Among these, coordination with nickel (Ni^{2+}) and vanadium in the form of vanadyl (VO^{2+}) are the most commonly observed in sediment, while Fe-, Ga-, Cu-, Mn- and Co-porphyrins are less frequently reported.

Metalloporphyrins have demonstrated their potential in recording the redox state of the depositional environment. For instance, the ratio of VO- and Ni-porphyrins has been proposed as an indicator of the Eh/ pH conditions during deposition (Lewan and Maynard, 1982; Lewan, 1984). When vanadium is the dominant coordinated metal, it is an indication of anoxic or euxinic conditions. This occurs due to the presence of hydrogen sulfide that causes Ni^{2+} to precipitate as nickel sulfide. This removal of Ni^{2+} from the solution prevents its coordination with free based porphyrins (Lewan and Maynard, 1982; Lewan, 1984; Huseby et al., 1996; Junium et al., 2008, 2015). Consequently, VO^{2+} porphyrin complexes are favored. In a more oxidative environment, where Ni^{2+} is not removed by sulfide, both Ni^{2+} and VO^{2+} ions are present in the solution, competing for chelation with porphyrins. In this case, nickel predominates the competition due to the higher equilibrium constant of Ni-porphyrins compared to VO-porphyrins. As a result, an increase in Ni-porphyrins relative to vanadyl

complexes is observed in more oxidative environments (Moldowan et al., 1985; Chen and Philp, 1991). Therefore, the ratio of VO-porphyrins to the total VO- and Ni-porphyrins, represented as VO/(VO+Ni), was proposed as a proxy to assess the degree of anoxia in water. According to Lewan (1984), a ratio of < 0.10 indicates Regime I, characterized by pH values greater than 7 and organic matter with low sulfur content. A ratio ranging from 0.10 to 0.90 with sulfur content <1wt% represents Regime II. In this regime, there is a more balanced availability of vanadyl and nickel as the conditions become more acidic. Regime III is only present in highly reducing environments with high concentrations of sulfide, which is usually characterized with a VO/(VO+Ni) ratio > 0.50 and high sulfur content > 1wt%.

Applying a newly developed RPLC-ESI-qTOF-MS method (Liu, 2023), we measured the distribution of VO- and Ni-porphyrins in black shales of the Late Devonian–Early Mississippian Woodford formation. Our data reveal a characteristic distribution of VO- and Ni-porphyrins in the black shales that resulted from both redox variation and selective chelation of metal species to different tetrapyrrole structures.

1.2. Materials and methods

1.2.1. Site of study and rock sample preparation

The Woodford Shale is Late Devonian-Early Mississippian (Comer, 1991) and records an estimated 29 myr of deposition (Johnson et al., 1985) when significant variations in the depositional environment occurred. Sedimentation rate, redox conditions, light intensity, and water chemistry experienced strong fluctuation, resulting in changes of the planktonic microbial communities. The Woodford Shale is conventionally divided into three sections, the Lower,

Middle, and Upper Woodford. Previous studies on the Woodford Shale, specifically the Wyche-1 core used for this study, show that it is characterized by episodic photic zone euxinia during the Lower Woodford deposition and sustained photic zone euxinia in the Middle Woodford attributed to stagnant circulation within a restricted basin, and the deepening of chemocline and subsequent breakdown of water column stratification in the Upper Woodford (Turner and Slatt, 2016; Connock et al., 2018). The Wyche-1 core was taken from the Wyche Shale Pit located at UTM: 14S X = 716339 Y = 3839956 (34.67875◦N, -96.63864◦W). Wyche-1 was drilled as a research well, producing core and log data for the OU-Devon-Schlumberger enterprise. Total core length is approximately 200 ft. (~61 m) long, comprising Woodford and pre-Welden formations. The Woodford deposit of this core is thermally immature, which is evidenced by the Rock Eval analyzed T_{max} values and the stereochemistry of sterane and hopane biomarkers (Connock et al., 2018). Sixty-one Woodford Shale samples were directly collected from the Wyche-1 core for this study. Rock samples were taken from the core by breaking off portions with a rock hammer while the sample was wrapped in combusted aluminum foil. The samples were rinsed with deionized water to remove any dust on their outside, then rinsed with a 1:4 solution of dichloromethane (DCM) and methanol (MeOH) to remove any residual contaminants from handling, plastics, drilling mud, or other samples. The samples were then left to dry completely before being crushed. Rock samples were crushed into a fine powder using a clean porcelain mortar and pestle which was cleaned between each sample by first rinsing with deionized water, grinding combusted sand, and finally rinsing with 1:1 DCM:MeOH. The crushed rock powder was then stored in combusted glass jars for subsequent analysis.

1.2.2. Total organic carbon measurement

All total organic carbon (TOC) measurements were performed by the Reservoir Technology Center Lab at Chesapeake Energy Corporation. A combusted ceramic crucible was loaded with 25 mg of rock powder followed by addition of 1 mL of 5 N HCl. The crucible was then heated to 115 °C. Once the 5 N HCl evaporated, 1 mL of 5 N HCl was added which was then left to dry. The treated sample was then washed with 2 mL of distilled deionized water and left to dry completely. Prior to sample analysis, the LECO C-230 Carbon Determinator was calibrated using five blanks and two carbon standards (5.02 %, part no. 502–319 and 1.89 %, part no. 502–320) with identical accelerants used in sample measurements. One LECO metal scoop (part no. 733–579) of copper metal (part no. 501–263) and Lecocell II (part no. 501–008) accelerants were added to each sample before being loaded onto the C-230 instrument. The two carbon standards were analyzed every 10 sample runs.

1.2.3. Extraction for lipid biomarker analysis

Approximately 500 mg of crushed Woodford shale was transferred into a combusted 4 mL vial, and then spiked with artificial standards, 100 ng of C_{46} glycerol trialkyl glycerol tetraether (C_{46} GTGT), 1000 ng of β-carotene, 1000 ng of VO-tetraphenylporphyrin (VO-TPP), and 1000 ng of Ni-TPP. We intended to utilize β-carotene as the internal standard for quantitative analysis of aromatic carotenoids, but struggled to detect it, and TPP for metalloporphyrins. Despite the absence of glycerol tetraether lipids in the Woodford shale, we routinely included C_{46} GTGT as an internal standard to monitor the general lipid recovery of extraction. The samples then had 1.5 mL of DCM and MeOH solution (1:1, v/v) added to them and mixed with a vortexer for a few seconds, and then sonicated in a water bath for 20 min for

lipid extraction. After the extraction, samples were centrifuged for 5 min at 3000 rpm. The solvent extract was transferred into a combusted and weighted 4 mL vial which was then concentrated under a gentle N_2 stream. The same extraction process was repeated for a total of two times, then it was repeated for another two times using acetone for a total of four extractions. After the fourth extraction, the solvents of the combined extracts dried completely and the vial and the total lipid extract (TLE) were weighed. After weighing the TLE, 1 mL of 1:1 Acetone:MeOH was added to the 4 mL vial to dissolve the TLE and 500 µL was transferred to a 2 mL vial. The 2 mL vial was then placed under N_2 until the sample was completely dried. Then 1 mL of MeOH was added into the dried 2 mL vial, and the vial was then ultrasonicated for 5 min and centrifuged for 5 min at 3000 rpm. The clear supernatant was then transferred into a new clean 2 mL vial for injection.

1.2.4. RPLC-ESI-qTOF-MS

Analysis was done on an Agilent 1290 series UPLC system coupled with an Agilent 6530 qTOF mass spectrometer through an Agilent jet stream dual electrospray ionization (AJS-ESI) interface. The LC-MS setup follows method description reported in Liu (2023). Briefly, as an ESI drying gas N_2 was used with a temperature set to 300 °C, the flow rate of N_2 was 8 L min^{-1} with the nebulizer gas (N_2) pressure at 35 psi. The qTOF parameters were set to: capillary voltage 3.5 kV, fragmentor voltage 175 V, skimmer voltage 65 V, and octupole voltage 750 V in auto MS/MS scanning mode with an MS range of *m/z* 50–2000 and an MS/MS range of *m/z* 20–2000. The collision gas used for collision induced dissociation (CID) was N_2. Depending on the application of the CID, voltage of collision cell was set at 40 or 200 eV. Compound separation was achieved by injecting 10 µL of sample onto an ACE UtraCore Super C_{18} column (5 µm, 2.1x250 mm, ACE,

Aberdeen, UK) maintained at 45 °C. The LC program was set to have a flow rate of 0.2 mL min^{-1}, from 95 % A and 5 % B to 40 % A and 60 % B in 35 min and then re-equilibrated with 95 % A and 5 % B at a flow rate of 0.4 mL min^{-1} for 5 min. Eluent A was 95:5:0.04:0.10 of methanol/H_2O/formic acid/14.8 M NH_3(aq.), eluent B was 50:50:0.04:0.10 of hexane/2-propanol/formic acid/14.8 M NH_3(aq.).

1.2.5. Lipid biomarker identification and quantification

Data analyses were performed using Agilent MassHunter Qualitative Analysis software (version B.08.00). The C_{40} aromatic carotenoids and metalloporphyrins were identified by their accurate masses, characteristic MS_2 fragmentation patterns, and relative retention times. The occurrence of isorenieratane and paleorenieratane in Woodford Shale has been reported in Connock et al. (2018), and their identification is confirmed in this study. The identification of VO- and Ni-porphyrins is further verified by the direct detection of chelated-to-porphyrin metal ions, V^+ and Ni^+, under 200 eV CID (see discussion in Liu, 2023). For quantification, targeted biomarker peaks were extracted and then integrated in EIC (extracted ion chromatogram). Concentrations of metalloporphyrins in samples were normalized to TOC and calculated using the injected internal standards, VO-TPP for VO-porphyrins and Ni-TPP for Ni-porphyrins, by assuming the same response factor of analytes as their corresponding artificial standards. However, the Woodford shale extracts showed a very poor recovery of β-carotene, likely due to its multiple conjugated double bonds, which are prone to react with the abundant organic sulfur in shale (LaLonde et al., 1987; Wakeham et al., 1995). As an alternative approach, we utilized C_{46} GTGT to estimate the concentration variation of C_{40} aromatic carotenoids.

1.3. Results and Discussions

1.3.1. The occurrence of C_{40} aromatic carotenoids and PZE

Isorenieratane and paleorenieratane are the two C_{40} aromatic carotenoids detected in the Woodford Shales (Figure 1.2, also see Connock et al., 2018). The depth profiles of isorenieratane and paleorenieratane generated with LC-MS are consistent with those reported by Connock et al. (2018) using GC-MS (see Supplementary 1.1). In the Lower Woodford, a substantial amount of isorenieratane and paleorenieratane is detected, although their concentrations are relatively low compared to the Middle Woodford. Notably, a significant increase in isorenieratane and paleorenieratane concentration in the Middle Woodford occurs around 170 ft and remains high until approximately 130 ft. This suggests the development of sustained intensive PZE during this interval of the Middle Woodford. In contrast, the Upper Woodford is characterized by consistently low abundance of C_{40} aromatic carotenoids, one order of magnitude lower in concentration compared to the two bottom sections, indicating a relatively less reducing depositional environment, likely associated with seasonal PZE or mixing of signals from small isolated sub-basins (Turner et al., 2016).

1.3.2. The distributions of VO- and Ni-porphyrins and redox variation

In the analyzed Woodford shales all geoporphyrins are associated with VO^{2+} and Ni^{2+}; no free base porphyrins were detected. Both VO-and Ni-porphyrins consist of tetrapyrrole cores of BiCAP, DPEP, and ETIO configurations. For each of the three categories of VO- and Ni-porphyrins multiple tetrapyrrole derivatives were detected (See Figure 1.2 for major metalloporphyrins detected). The VO-porphyrins contain carbon numbers of C_{31}-C_{33} BiCAP, C_{29}-C_{32} DPEP, and

C_{29}-C_{32} Etio. The Ni-porphyrins comprise C_{31}-C_{33} BiCAP, C_{30}-C_{32} DPEP, and C_{27}-C_{32} Etio. In both VO- and Ni-porphyrins, the predominant compounds within each category are C_{33} BiCAP, C_{32} DPEP and C_{32} and C_{31} Etio (Figure 1.2). The dominance of C_{33}-BiCAP and C_{32}-DPEP within each category of porphyrins is consistent with their proposed origin from chlorophyll-α (Figure 1.1). However, Etio porphyrins can be contributed by the degradation of both chlorophylls and hemes. The reduction and decarboxylation of heme-*b* do result in the C_{32}-Etio structure. The degradation of chlorophyll-α allomers, such as 15-OH-lactone-pheophytin-α (as depicted in Figure 1.1), predominantly yields C_{31}-Etio, which accounts for its relatively high abundance in most samples (as indicated by the signal intensity of C_{31}-Etio in Figure 1.2). It is worth noting that the production of C_{32}-Etio from chlorophylls through complex diagenetic processes cannot be completely ruled out. Porphyrin derivatives with fewer carbon atoms within each category likely result from further dealkylation during diagenesis.

The concentration of VO-porphyrins is generally low in the Lower Woodford with a peak right before the Lower/Middle Woodford boundary at 186.42 ft (Figure 1.3). Their concentration then decreases and remains low through most of the Middle Woodford before an increase at 160.17 ft, peaking at 146 ft, and then returns to low concentration at 130 ft. In the Upper Woodford, the concentration of VO-porphyrins increases dramatically corresponding to the oxic/suboxic conditions seen in the Upper Woodford (Turner and Slatt, 2016). The Ni-porphyrins show a similar depth profile as VO-porphyrins except for the topmost part of the Upper Woodford where Ni-porphyrins remain in high abundance while VO-porphyrins drop (Figure 1.3). The Ni-porphyrins are low in concentration in the Lower Woodford with a peak at 186.42 ft across the Lower/Middle Woodford boundary. In the Middle Woodford Shale, concentrations

stay low until at 153.58 ft, then their concentration increases and peaks at 147.08 ft before dropping at 131.75 ft. In the Upper Woodford, the abundance of Ni-porphyrins has a peak at the same depth as VO-porphyrins but then dropped at 91.50 ft, and continues to increase with a peak concentration at 78.00 ft.

The VO/(VO+Ni) ratio in the Woodford shale exhibits consistently high values (>0.5) throughout the Lower and Middle Woodford sections, as well as the bottom sequence of the Upper Woodford (Figure 1.3). This high VO/(VO+Ni) ratio indicates a sustained reducing or sulfidic deposition environment (Lewan,1984). In the lower Upper Woodford, where C_{40} aromatic carotenoids are already scarce, the VO/(VO + Ni) ratio remains high, suggesting persistent anoxia in the bottom water despite the collapse of photic zone euxinia at the top of the Middle Woodford. Notably, a significant drop in the VO/(VO+Ni) ratio to 0.21 occurs only in the very late Upper Woodford, from 80.67 to 74 ft, reflecting the eventual oxygenation of the whole water column.

Despite the high VO/(VO+Ni) ratio in the Middle Woodford, there is a distinct increase of Ni-porphyrins concentration between 169.33 and 131.75 ft, which coincides with the peak of isorenieratane and paleorenieratane or intensified PZE. The abundant Ni-porphyrins occurring during the peak of PZE implies that thermodynamic limitation of Ni^{2+} through the formation of Ni sulfide (Lewan, 1984) is not a primary control of Ni-porphyrin abundance during this PZE interval of Woodford. Junium et al. (2015) observed similar metalloporphyrin distributions in the OAE-2 black shales, the occurrence of Ni- and Zn-porphyrins within euxinic deposition. It is worth noting that Ni^{2+} can still be available under sulfidic condition (Algeo and Maynard, 2004)

and the chelation of Ni by porphyrin could happen during late diagenesis in subsurface sediment (Junium et al., 2015; Prowse et al., 1990).

1.3.3. The role of tetrapyrrole configuration and selective metalation

There is a strong preference for Ni to be chelated to Etio compared to BiCAP and a strong preference for VO to be associated with BiCAP compared to Etio (Figure 1.4). Ni-porphyrins in the Middle Woodford Shale even have Ni-BiCAP being undetectable in some samples. Similarly, it has been reported in previous studies (Qian et al., 2010; Sundararaman and Boreham, 1993) that Etio is favored relative to BiCAP to form a nickel complex, conversely BiCAP is favored relative to Etio in vanadyl complexes. The bias of formation of the Ni^{2+} and VO^{2+} chelation to BiCAP and Etio is clearly determined by the structural features of BiCAP and Etio. The Ni^{2+} ions have a very strong preference for square-planar binding with the Ni atom in the plane of the four porphyrin N atoms (Kim et al., 1996). The VO-porphyrin complexes on the other hand have a five-coordinate square-pyramidal geometry, with the V atom sitting above the plane of the four porphyrin N atoms and the O atom bound in the axial position (Drew et al., 1984; Zhang et al., 2019). Since Etio is the least constrained in its ring flexibility as a result of its lack of the E and F ring structures, it is more easily to adopt a conformation in which the four N atoms form a perfect square-planar coordination environment to chelate Ni^{2+}. The increased rigidity caused by the extra E and F ring structures in BiCAP and DPEP might prevent them from adopting such a geometry leading to puckering of the porphyrin macrocycle and a non-ideal arrangement for Ni. Since VO does not reside in the plane of the porphyrin, it might be less constrained to coordinating to a perfect porphyrin configuration compared to the Ni.

As a result of selective metal chelation, a strong positive correlation is observed in the cross plot of BiCAP/Etio vs VO/Ni in each section of the Upper, Middle, and Lower Woodford Shale, with respective R^2 values of 0.85, 0.85, and 0.83 (Figure 1.5). Linear regression of the Lower and Middle Woodford sections exhibits the same slope value of 1.24, which is lower than that of the Upper Woodford (1.8). As mentioned above, both the Lower and Middle Woodford sections are characterized by the presence of a significant amount of aromatic carotenoids and low porphyrin concentrations (Figure 1.3), indicating persistent anoxic/stratified conditions. In contrast, the increased porphyrin concentrations in the Upper Woodford are associated with a decrease in the VO/(VO+Ni) ratio and aromatic carotenoid levels approximately one order of magnitude lower than the lower sections, indicating subsequent oxygenation and recovery of primary productivity. The higher regression slope of the Upper Woodford compared to the Middle and Lower sections in the cross plot (Figure 1.5) suggests that the BiCAP/Etio ratio could be influenced by both water column redox conditions and phytoplankton activity. A comprehensive discussion on how phytoplankton metabolism determines porphyrin compositions will be presented in a separate work. In general, the strong correlation between BiCAP/Etio and VO/Ni confirms that both the availability of metal ions and the tetrapyrrole configurations play significant roles in the distribution of VO- and Ni-porphyrins within sediment. When thermodynamic limitation of Ni^{2+} is not predominant during deposition, the molecular configurations of porphyrins, particularly the relative abundance of Etio compared to BiCAP, becomes crucial in determining the ratio of VO/Ni. As BiCAP and Etio porphyrins can be associated with distinct biological processes like herbivorous grazing (Goericke et al., 2000; Kashiyama et al., 2012) and chlorophyll metabolism (Maroneze et al., 2019), the potential of

BiCAP/ Etio ratio as proxy for such biological processes warrants further exploration in future studies. An understanding of the biological and environmental factors influencing the distribution of porphyrin configurations will also broaden the applicability of porphyrin-based proxies, such as the BiCAP/Etio ratio, in specific geological settings where metalloporphyrins are absent.

1.4. Conclusion

The depth profiles of isorenieratane and paleorenieratane align with previous findings, showing substantial amounts in the Lower Woodford and a significant increase in concentration during the Middle Woodford, indicative of intensified PZE. The scarcity of C_{40} aromatic carotenoids in the Upper Woodford suggests the collapse of sustained PZE and transition to a less reducing deposition environment. The concentrations and depth profiles of VO- and Ni-porphyrins varied throughout the Woodford shale, reflecting changes in primary productivity and water column redox conditions. The persistent high VO/(VO+Ni) ratio in the Lower and Middle Woodford suggests a sustained reducing or sulfidic deposition environment, while the significant drop in the ratio in the late Upper Woodford indicates eventual oxygenation of the water column. Notably, the Middle Woodford exhibited slightly increased concentrations of both VO- and Ni-porphyrins, overlapping with the peak abundance of C_{40} aromatic carotenoids. The observed increase in Ni-porphyrin concentration during the PZE interval suggests that thermodynamic limitation of Ni^{2+} through the formation of nickel sulfide is not the primary control for their abundance in this interval.

The selective metal chelation of porphyrins contributes to a strong correlation between BiCAP/Etio and VO/Ni ratios. This finding emphasizes the combined influence of metal ion availability and tetrapyrrole configurations on the distribution patterns of VO- and Ni-porphyrins within the sediment. The structural composition, particularly the relative abundance of Etio compared to BiCAP, must be considered as a critical factor in determining the ratio of VO- versus Ni-porphyrins. Since BiCAP and Etio porphyrins have been associated with distinct biological processes, such as herbivorous grazing and chlorophyll metabolism, our findings suggest the potential use of BiCAP and Etio distribution as proxies for these processes. Further investigations are warranted to explore the full potential of these biomarker compounds as indicators of biological activities in deep time.

1.5 References

Algeo, T.J., Maynard, J.B., 2004. Trace-element behavior and redox facies in core shales of Upper Pennsylvanian Kansas-type cyclothems. Chemical Geology 206, 289–318. Boreham, C.J., Fookes, C.J.R., Popp, B.N., Hayes, J.M., 1989. Origins of etioporphyrins in sediments: Evidence from stable carbon isotopes. Geochimica et Cosmochimica Acta 53, 2451–2455.

Boreham, C.J., Fookes, C.J.R., Popp, B.N., Hayes, J.M., 1989. Origins of etioporphyrins in sediments: Evidence from stable carbon isotopes. Geochimica et Cosmochimica Acta 53, 2451–2455.

Callot, H.J., Ocampo, R., 2000. Geochemistry of Porphyrins. The Porphyrin Handbook. Academic Press, pp. 349–398.

Chen, J.H., Philp, R.P., 1991. Porphyrin distributions in crude oils from the Jianghan and Biyang basins, China. Chemical Geology 91, 139–151.

Comer, J., 1991. Stratigraphic Analysis of the Upper Devonian Woodford Formation, Permian Basin, West Texas and southeastern New Mexico (Report Investigation), Report Investigation. University of Texas at Austin, Bureau of Economic Geology. https://doi.org/10.23867/RI0201D.

Connock, G.T., Nguyen, T.X., Philp, R.P., 2018. The development and extent of photic-zone euxinia concomitant with Woodford Shale deposition. AAPG Bulletin 102, 959–986.

David, A., 1998. Recognition of Photic Zone Anoxia from LC-MS Studies of Porphyrin Distributions in Ancient Sediment. Doctoral Thesis. University of Bristol, p. 245.

Drew, M.G.B., Mitchell, P.C.H., Scott, C.E., 1984. Crystal and molecular structure of three oxovanadium(IV) porphyrins: oxovanadium tetraphenylporphyrin(I), oxovanadium (IV) etioporphyrin(II) and the 1:2 adduct of (II) with 1,4-dihydroxybenzene(III). Hydrogen bonding involving the VO group. Relevance to catalytic demetallisation. Inorganica Chimica Acta 82, 63–68.

Goericke, R., Strom, S.L., Bell, M.A., 2000. Distribution and sources of cyclic pheophorbides in the marine environment. Limnology and Oceanography 45, 200–211.

Huseby, B., Barth, T., Ocampo, R., 1996. Porphyrins in Upper Jurassic source rocks and correlations with other source rock descriptors. Organic Geochemistry 25, 273–294.

Itoh, S., Mino, H., Itoh, K., Shigenaga, T., Uzumaki, T., Iwaki, M., 2007. Function of chlorophyll d in reaction centers of photosystems I and II of the oxygenic photosynthesis of Acaryochloris marina. Biochemistry 46, 12473–12481.

Johnson, J.G., Klapper, G., Sandberg, C.A., 1985. Devonian eustatic fluctuations in Euramerica. GSA Bulletin 96, 567–587.

Junium, C.K., Mawson, D.H., Arthur, M.A., Freeman, K.H., Keely, B.J., 2008. Unexpected occurrence and significance of zinc alkyl porphyrins in Cenomanian-Turonian black shales of the Demerara Rise. Organic Geochemistry 1081–1087.

Junium, C.K., Freeman, K.H., Arthur, M.A., 2015. Controls on the stratigraphic distribution and nitrogen isotopic composition of zinc, vanadyl and free base porphyrins through Oceanic Anoxic Event 2 at Demerara Rise. Organic Geochemistry 80, 60–71.

Kashiyama, Y., Yokoyama, A., Kinoshita, Y., Shoji, S., Miyashiya, H., Shiratori, T., Suga, H., Ishikawa, K., Ishikawa, A., Inouye, I., Ishida, K., Fujinuma, D., Aoki, K., Kobayashi, M., Nomoto, S., Mizoguchi, T., Tamiaki, H., 2012. Ubiquity and quantitative significance of detoxification catabolism of chlorophyll associated with protistan herbivory. Proceedings of the National Academy of Sciences 109, 17328–17335.

Kashiyama, Y., Ogawa, N.O., Kitazato, H., Ohkouchi, N., 2010. Nitrogen and carbon isotopic compositions of copper, nickel, and vanadyl porphyrins in Cretaceous black shales. In: Ohkouchi, N., Tayasu, I., Koba, K. (Eds.), Earth, Life, and Isotopes. Kyoto University Press, pp. 313–335.

Keely, B.J., Prowse, W.G., Maxwell, J.R., 1990. The Treibs hypothesis: an evaluation based on structural studies. Energy & Fuels 4, 628–634.

Kim, J.S., Reibenspies, J.H., Darensbourg, M.Y., 1996. Characteristics of nickel(0), nickel (I), and nickel(II) in phosphino thioether complexes: Molecular structure and S-dealkylation of (Ph2P(o-C6H4)SCH3)2Ni0. Journal of the American Chemical Society 118, 4115–4123.

LaLonde, R.T., Ferrara, L.M., Hayes, M.P., 1987. Low-temperature, polysulfide reactions of conjugated ene carbonyls: A reaction model for the geologic origin of S-heterocycles. Organic Geochemistry 11, 563–571.

Lewan, M.D., 1984. Factors controlling the proportionality of vanadium to nickel in crude oils. Geochimica et Cosmochimica Acta 48, 2231–2238.

Lewan, M.D., Maynard, J.B., 1982. Factors controlling enrichment of vanadium and nickel in the bitumen of organic sedimentary rocks. Geochimica et Cosmochimica Acta 46, 2547–2560.

Liu, X.-L., 2023. Collision-induced dissociation as “mass spectrometric filter” for rapid screening of tetrapyrrole derivatives and their chelated metal species in complex biological and environmental samples. Rapid Communications in Mass Spectrometry 37, e9413.

Louda, J.W., Li, J., Liu, L., Winfree, M.N., Baker, E.W., 1998. Chlorophyll-a degradation during cellular senescence and death. Organic Geochemistry 29, 1233–1251.

Louda, J.W., Loitz, J.W., Rudnick, D.T., Baker, E.W., 2000. Early diagenetic alteration of chlorophyll-a and bacteriochlorophyll-a in a contemporaneous marl ecosystem; Florida Bay. Organic Geochemistry 31, 1561–1580.

Louda, J.W., Mongkhonsri, P., Baker, E.W., 2011. Chlorophyll degradation during senescence and death-III: 3–10yr experiments, implications for ETIO series generation. Organic Geochemistry 42, 688–699.

Maroneze, M.M., Zepka, L.Q., Lopes, E.J., P´erez-Ga´lvez, A., Roca, M., 2019. Chlorophyll oxidative metabolism during the phototrophic and heterotrophic growth of Scenedesmus obliquus. Antioxidants 8, 600.

Moldowan, J.M., Seifert, W.K., Gallegos, E.J., 1985. Relationship between petroleum composition and depositional environment of petroleum source rocks. AAPG Bulletin 69, 1255–1268.

Naylor, C.C., Keely, B.J., 1998. Sedimentary purpurins: Oxidative transformation products of chlorophylls. Organic Geochemistry 28, 417–422.

Nguyen, D.D., Sauer, J.S., Camarda, L.P., Sherman, S.L., Prather, K.A., Golden, S.S., Pomeroy, R., Dorrestein, P.C., Simkovsky, R., 2022. Grazer-induced changes in molecular signatures of cyanobacteria. Algal Research 61, 102575.

Ocampo, R., Callot, H.J., Albrecht, P., Popp, B.N., Horowitz, M.R., Hayes, J.M., 1989. Different isotope compositions of C32 DPEP and C32 etioporphyrin III in oil shale - Origin of etioporphyrin III from heme? Die Naturwissenschaften 76, 419–421.

Prowse, W.G., Keely, B.J., Maxwell, J.R., 1990. A novel sedimentary metallochlorin. Organic Geochemistry 16, 1059–1065.

Qian, K., Edwards, K.E., Mennito, A.S., Walters, C.C., Kushnerick, J.D., 2010. Enrichment, resolution, and identification of nickel porphyrins in petroleum asphaltene by cyclograph

separation and atmospheric pressure photoionization Fourier transform ion cyclotron resonance mass spectrometry. Analytical Chemistry 82, 413–419.

Stuart Walker, J., Keely, B.J., 2004. Distribution and significance of chlorophyll derivatives and oxidation products during the spring phytoplankton bloom in the Celtic Sea April 2002. Organic Geochemistry 35, 1289–1298.

Sundararaman, P., Boreham, C.J., 1993. Comparison of nickel and vanadyl porphyrin distributions of sediments. Geochimica et Cosmochimica Acta 57, 1367–1377.

Treibs, A., 1936. Chlorophyll- und H¨aminderivate in organischen Mineralstoffen. Angewandte Chemie 49, 682–686.

Turner, B.W., Slatt, R.M., 2016. Assessing bottom water anoxia within the Late Devonian Woodford Shale in the Arkoma Basin, southern Oklahoma. Marine and Petroleum Geology 78, 536–546.

Turner, B.W., Tre´anton, J.A., Slatt, R.M., 2016. The use of chemostratigraphy to refine ambiguous sequence stratigraphic correlations in marine mudrocks. An example from the Woodford Shale, Oklahoma, USA. Journal of the Geological Society 173, 854–868.

Wakeham, S.G., Sinninghe Damste´, J.S., Kohnen, M.E.L., De Leeuw, J.W., 1995. Organic sulfur compounds formed during early diagenesis in Black Sea sediments. Geochimica et Cosmochimica Acta 59, 521–533.

Walker, J.S., Jie, C., Keely, B.J., 2003. Identification of diastereomeric chlorophyll allomers by atmospheric pressure chemical ionisation liquid chromatography/ tandem mass spectrometry. Rapid Communications in Mass Spectrometry 17, 1125–1131.

Woltering, M., Tulipani, S., Boreham, C.J., Walshe, J., Schwark, L., Grice, K., 2016. Simultaneous quantitative analysis of Ni, VO, Cu, Zn and Mn geoporphyrins by liquid chromatography-high resolution multistage mass spectrometry: Method development and validation. Chemical Geology 441, 81–91.

Zhang, Y., Schulz, F., Rytting, B.M., Walters, C.C., Kaiser, K., Metz, J.N., Harper, M.R., Merchant, S.S., Mennito, A.S., Qian, K., Kushnerick, J.D., Kilpatrick, P.K., Gross, L., 2019. Elucidating the geometric substitution of petroporphyrins by spectroscopic analysis and atomic force microscopy molecular imaging. Energy & Fuels 33, 6088–6097.

1.6 Figures

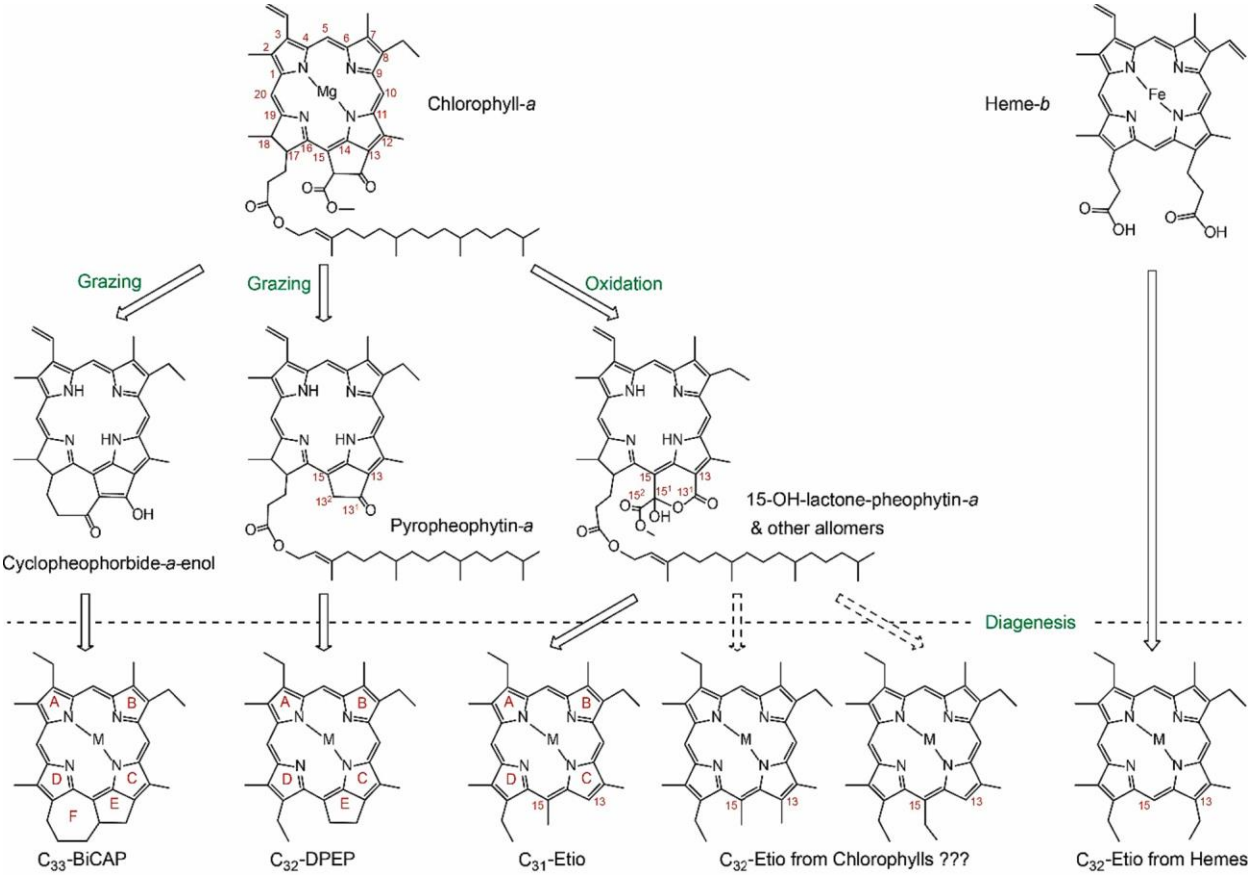


Figure 1.1 The proposed production of BiCAP, DPEP and Etio porphyrins through biological and chemical degradations on chlorophyll-α and heme-*b* (modified from Kashiyama et al., 2010). 15-OH-lactone-pheophytin-α is one of the major oxidized allomers of chlorophyll-α. Dashed line arrows represent possible, but yet unverified, production of C_{32}-Etios from chlorophylls. The letter 'M' in the molecule represents the metal species, specifically VO and Ni for this study, chelated to porphyrins.

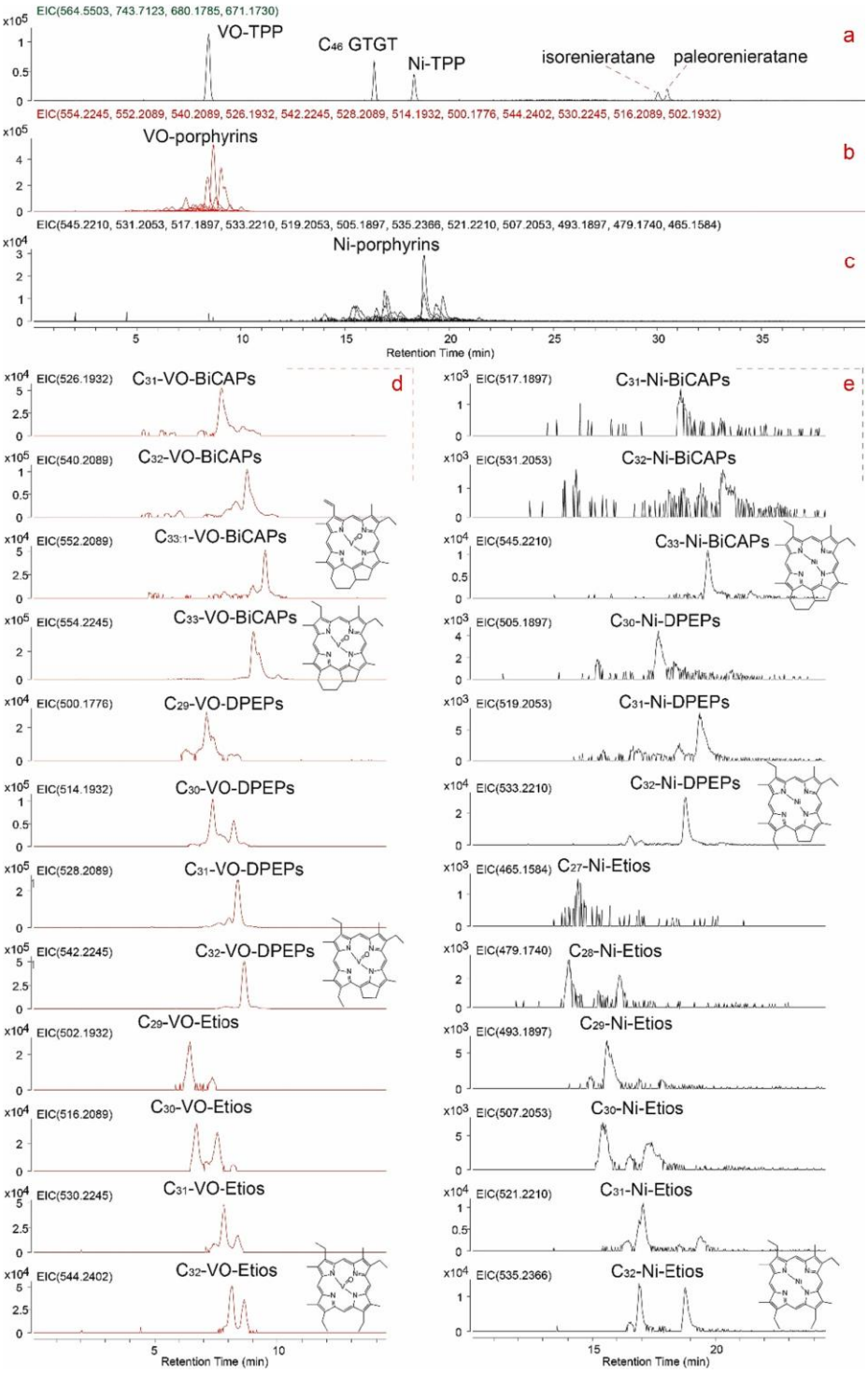


Figure 1.2 Extracted ion chromatograms (EICs) show the detection of artificial standards, isorenieratane, paleorenieratane and major VO- and Ni-porphyrins in the Woodford Shale sample, Wch-10 (91.5 ft). (a) Combined EICs of C_{46} GTGT, VO-TPP, Ni-TPP, isorenieratane and paleorenieratane. (b) Combined EICs of 12 major VO-porphyrins detected. (c) Combined EICs of 12 major Ni-porphyrins detected. (d) EICs show the detection of multiple isomers of each VO-porphyrin. $C_{33:1}$-VO-BiCAPs are VO-BiCAPs with an extra unsaturation equivalence, likely the preserved double bond on C3 ethyl group of chlorophyll-α (see molecular structure in Figure 1.1). $C_{33:1}$-Ni-BiCAPs only occur in a few samples with very low abundance, thus are not included in the analysis. (e) EICs show the detection of multiple isomers of each Ni-porphyrin. There are some other VO- and Ni-porphyrins detected in a few specific samples, but not presented and analyzed in this work.

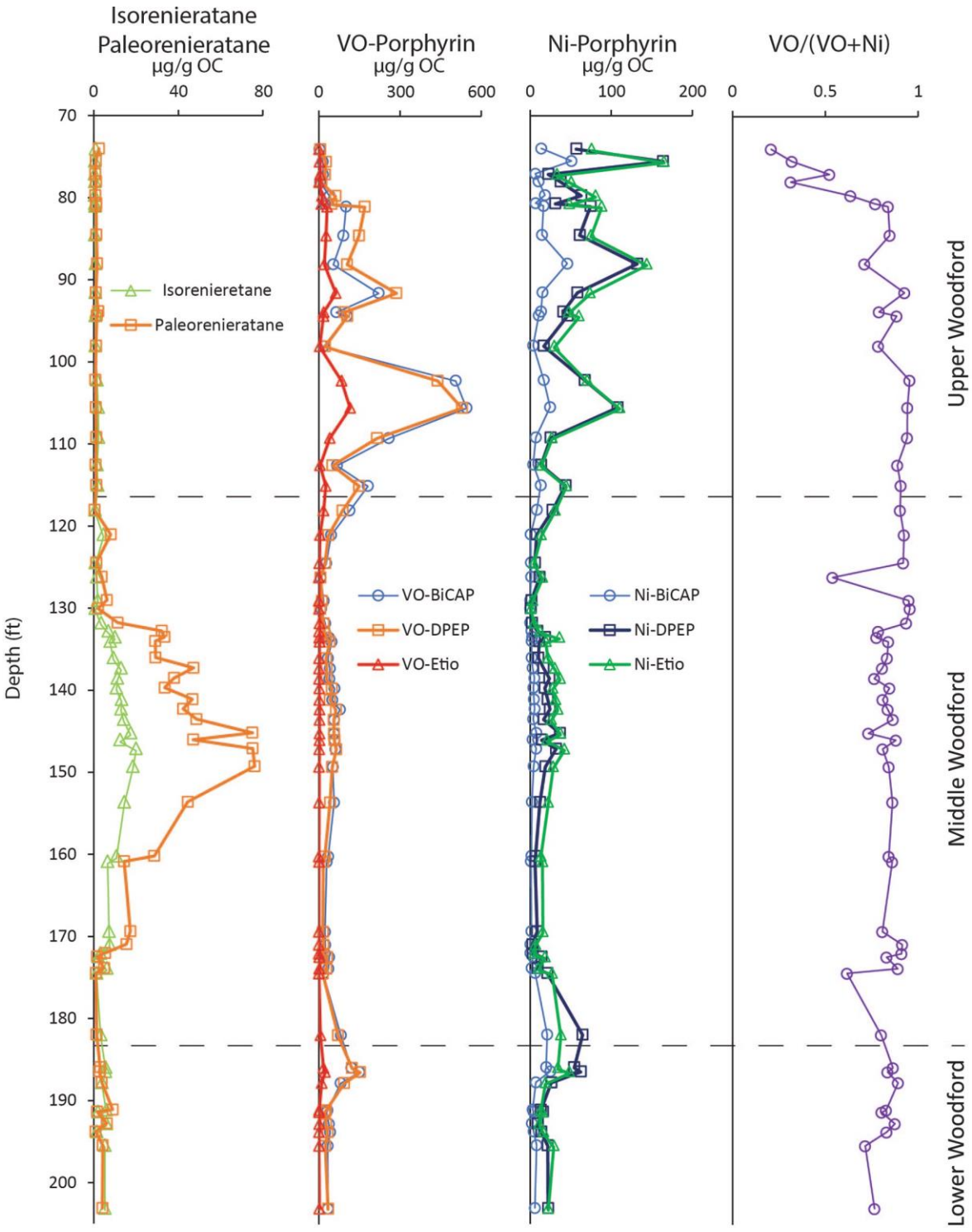


Figure 1.3 Depth profiles of the isorenieratane, paleorenieratane, VO- and Ni-porphyrins concentrations and the VO/(VO+Ni) ratio.

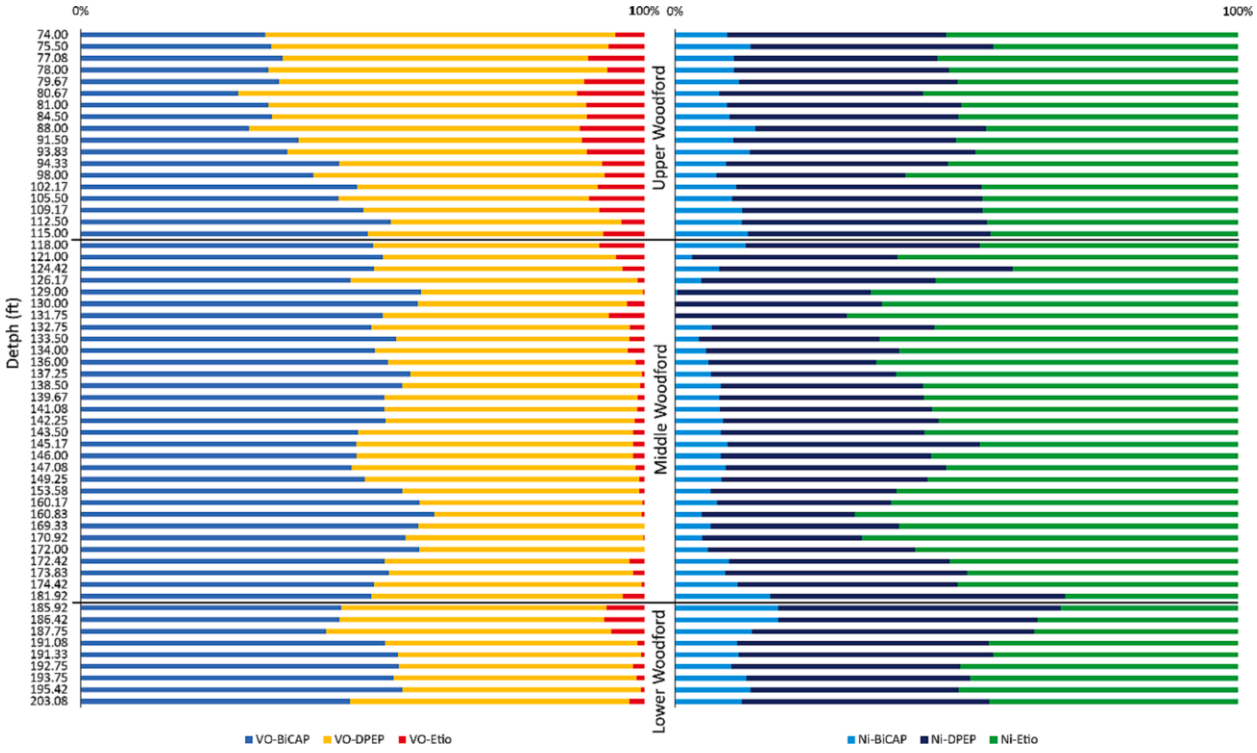


Figure 1.4 The relative abundance of BiCAP, DPEP and Etio configurations in VO- and Ni-porphyrins.

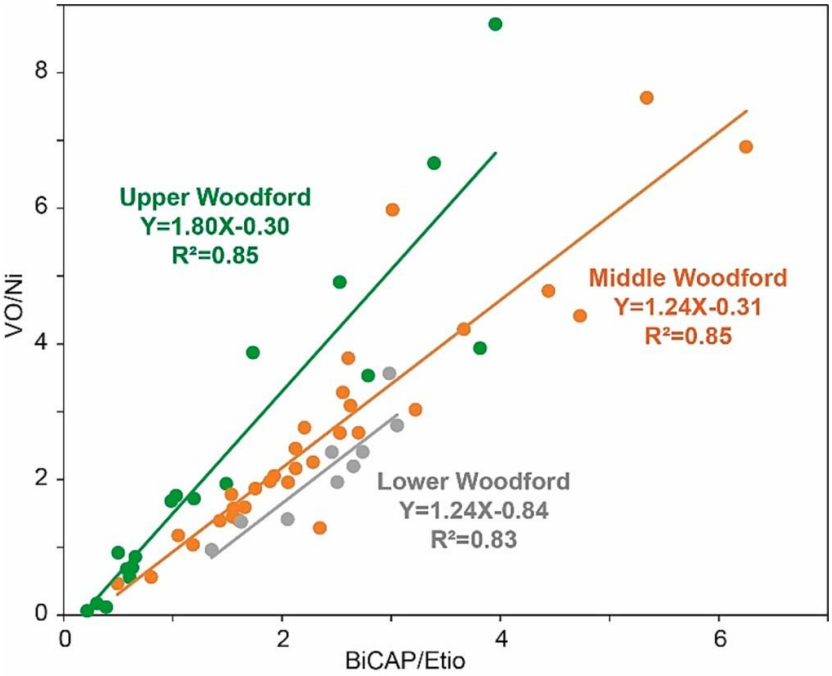
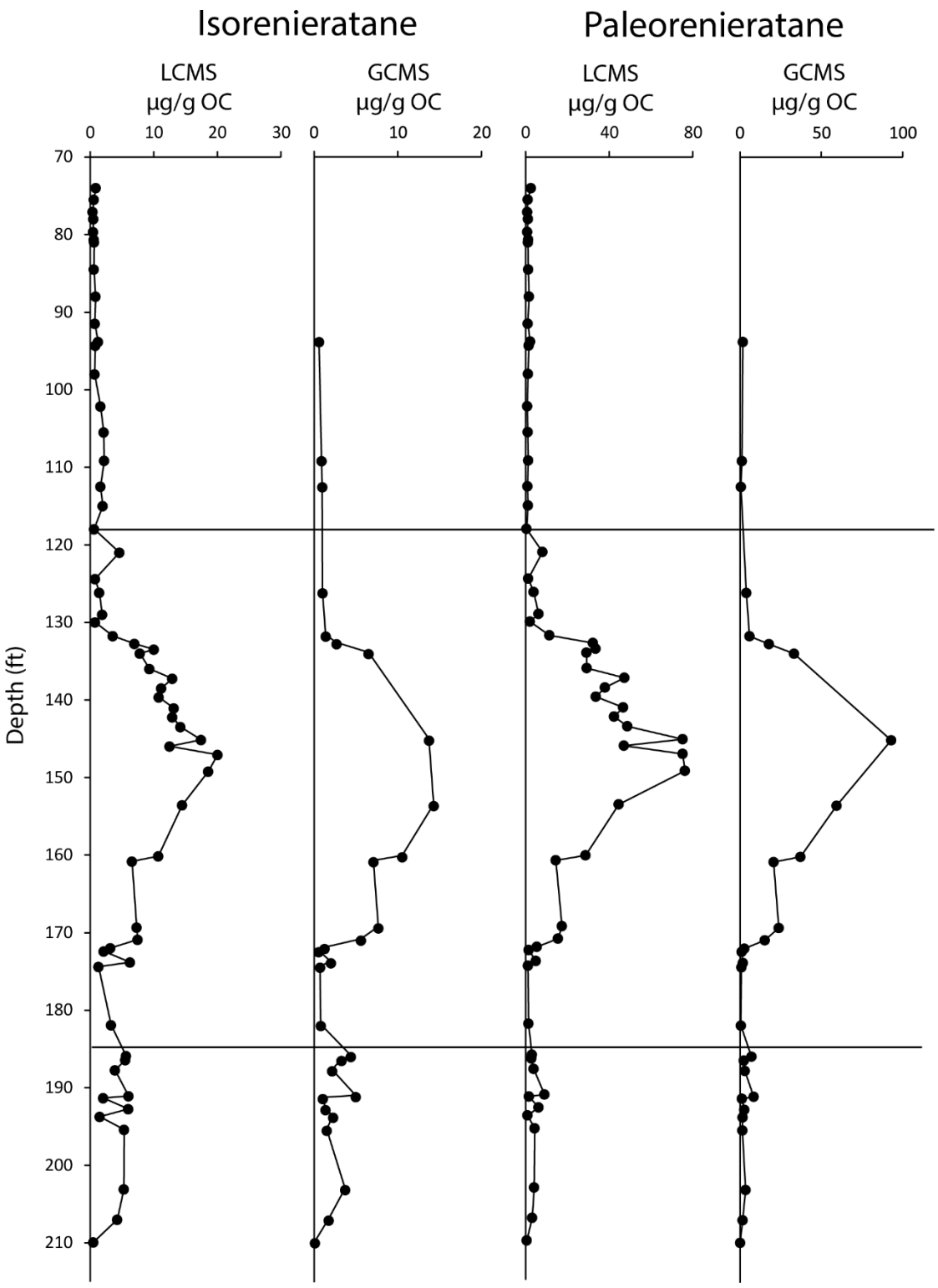


Figure 1.5 Cross plot shows the correlations between VO/Ni and BiCAP/Etio separated into each of the three sections of the Woodford Shale.

1.7 Supplemental



Supplementary 1.1 Depth profiles of isorenieratane and paleorenieratane show the consistency of data produced by LC-MS (this work) and GC-MS (Connock et al., 2018).

Sample	Depth	rock	TOC wt%	OC wt	Isorenieratane	Paleorenieratane	VO-BiCAP	VO-DPEP	VO-ETIO	Sum VO porphyrin	Ni-BiCAP	Ni-DPEP	Ni-ETIO	Sum Ni porphyrin
	(ft)	(g)		(g)	(ng/g OC)	(ng/g OC)	(ng/g OC)	(ng/g OC)	(ng/g OC)	(ng/g OC)	(ng/g OC)	(ng/g OC)	(ng/g OC)	(ng/g OC)
Wch-1	74.00	0.4800	3.00	0.0144	4.31	12.31	14.17	26.88	2.16	43.21	67.87	284.41	378.36	730.64
Wch-2	75.50	0.4253	7.79	0.0331	2.73	4.95	72.66	128.51	13.33	214.50	254.30	818.68	824.46	1897.44
Wch-3	77.08	0.4066	11.50	0.0468	1.85	3.61	74.92	113.48	20.61	209.02	32.26	111.66	164.58	308.50
Wch-4	78.00	0.4435	3.48	0.0154	2.49	5.73	27.28	49.30	5.27	81.86	51.51	188.03	252.39	491.93
Wch-5	79.67	0.4902	8.67	0.0425	2.25	3.89	198.57	305.66	59.58	563.81	91.89	314.26	402.15	808.31
Wch-6	80.67	0.4548	5.08	0.0231	2.70	6.26	110.08	236.69	46.66	393.43	33.61	155.32	240.28	429.21
Wch-7	81.00	0.4395	8.89	0.0391	3.03	5.66	501.30	848.16	152.82	1502.27	82.41	372.23	439.75	894.39
Wch-8	84.50	0.4738	8.04	0.0381	2.83	6.29	450.41	741.08	133.48	1324.97	72.80	305.75	374.18	752.74
Wch-9	88.00	0.4236	4.30	0.0182	4.17	8.02	265.52	520.79	100.85	887.16	229.46	659.15	717.98	1606.59
Wch-10	91.50	0.4634	10.20	0.0473	3.59	4.92	1103.10	1433.82	312.02	2848.93	76.34	291.24	368.50	736.08
Wch-40	93.83	0.4416	4.66	0.0206	6.00	10.94	321.59	465.75	88.13	875.47	67.70	204.45	237.97	510.12
Wch-11	94.33	0.4218	6.93	0.0292	3.95	7.20	517.43	526.79	83.02	1127.24	52.86	229.62	299.83	582.31
Wch-12	98.00	0.4197	3.25	0.0136	3.43	5.36	88.56	110.99	14.85	214.40	18.31	84.05	147.97	250.32
Wch-13	102.17	0.4475	8.14	0.0364	7.97	3.86	2527.05	2194.27	418.54	5139.86	83.87	336.15	351.14	771.17
Wch-14	105.50	0.4339	4.80	0.0208	10.47	5.07	2729.17	2645.73	577.05	5951.94	122.95	539.05	550.85	1212.85
Wch-41	109.17	0.4872	9.32	0.0454	10.96	5.91	1290.30	1075.76	201.54	2567.60	35.07	126.06	133.56	294.69
Wch-42	112.50	0.4044	10.60	0.0429	8.03	4.51	333.06	248.32	23.59	604.97	18.20	67.07	68.51	153.78
Wch-15	115.00	0.4348	8.83	0.0384	9.67	5.76	906.39	743.79	127.31	1777.49	65.18	217.52	221.17	503.86
Wch-16	118.00	0.4391	11.40	0.0501	3.05	1.80	567.16	438.68	85.58	1091.42	41.78	138.35	152.52	332.65
Wch-17	121.00	0.4402	8.77	0.0386	22.99	40.05	225.58	173.65	20.73	419.96	3.33	40.48	67.08	110.89
Wch-18	124.42	0.4064	11.20	0.0455	3.66	6.06	137.05	116.10	9.80	262.95	4.31	28.68	22.03	55.02
Wch-43	126.17	0.4024	3.47	0.0140	6.94	18.82	30.90	32.74	0.79	64.42	6.57	58.16	75.30	140.04
Wch-19	129.00	0.3983	11.20	0.0446	9.28	31.05	89.37	58.11	0.34	147.82	0.08	7.36	13.97	21.41
Wch-20	130.00	0.4527	11.50	0.0521	3.81	10.09	40.31	25.02	1.97	67.29	0.00	3.24	5.58	8.82
Wch-60	131.75	0.4246	10.00	0.0425	17.64	56.67	117.01	87.70	13.48	218.19	0.00	11.15	25.36	36.51
Wch-61	132.75	0.4762	8.63	0.0411	34.62	160.57	108.53	96.51	5.15	210.18	7.36	44.61	60.82	112.79
Wch-21	133.50	0.4214	7.05	0.0297	50.02	167.20	186.08	137.14	8.44	331.65	12.05	90.74	180.29	283.09
Wch-44	134.00	0.4168	8.66	0.0361	38.97	145.43	232.78	200.07	12.57	445.43	8.91	55.38	97.04	161.32
Wch-22	136.00	0.4313	7.01	0.0302	46.47	145.96	165.98	133.42	4.74	304.14	10.14	51.09	109.88	171.12
Wch-23	137.25	0.4348	5.78	0.0251	64.41	235.66	204.02	142.49	1.65	348.16	15.92	82.38	152.08	250.38
Wch-24	138.50	0.4571	4.81	0.0220	55.73	189.66	195.06	143.96	2.57	341.60	26.83	118.62	184.65	330.09
Wch-25	139.67	0.4410	7.14	0.0315	53.82	167.56	287.77	239.14	6.56	533.47	19.42	89.70	137.93	247.06
Wch-26	141.08	0.4940	4.86	0.0240	65.61	233.17	246.59	204.70	5.92	457.21	22.90	108.57	156.34	287.80
Wch-27	142.25	0.4406	6.80	0.0300	64.57	211.13	388.23	315.79	12.62	716.64	27.11	121.87	169.25	318.23
Wch-28	143.50	0.4416	8.04	0.0355	70.84	242.77	278.97	276.22	11.51	566.70	18.78	83.44	128.67	230.89
Wch-45	145.17	0.3816	6.48	0.0247	87.08	374.85	279.69	279.88	11.31	570.89	38.09	182.66	187.07	407.81
Wch-29	146.00	0.4429	7.37	0.0326	62.39	234.88	287.49	287.19	11.77	586.44	15.37	70.91	103.53	189.82
Wch-30	147.08	0.4462	5.62	0.0251	100.03	375.40	306.80	320.99	10.15	637.94	36.56	159.38	210.77	406.71
Wch-31	149.25	0.4709	5.83	0.0275	92.71	380.15	255.50	245.91	4.82	506.23	21.17	94.18	141.60	256.94
Wch-46	153.58	0.4337	6.79	0.0294	72.28	222.09	281.36	205.91	4.61	491.88	11.59	60.46	111.20	183.25
Wch-47	160.17	0.4107	7.14	0.0293	53.41	143.08	170.52	111.60	1.07	283.19	7.87	32.55	65.00	105.42
Wch-48	160.83	0.4047	7.55	0.0306	32.70	71.73	143.70	83.75	1.24	228.69	5.28	30.33	76.05	111.65
Wch-49	169.33	0.4216	5.86	0.0247	36.41	86.46	112.53	74.98	0.00	187.51	8.19	43.27	77.98	129.45
Wch-50	170.92	0.4160	8.02	0.0334	37.13	77.24	117.17	85.50	0.41	203.09	2.31	13.72	32.18	48.20
Wch-51	172.00	0.4373	11.10	0.0485	15.80	26.66	110.98	73.43	0.00	184.41	2.45	15.39	23.98	41.81
Wch-52	172.42	0.4472	6.59	0.0295	10.47	7.53	188.33	151.70	8.71	348.74	17.17	69.97	91.19	178.33
Wch-53	173.83	0.4275	10.30	0.0440	31.19	24.35	176.06	139.21	6.45	321.73	9.46	45.70	51.13	106.29
Wch-54	174.42	0.4424	3.90	0.0173	6.44	5.41	78.95	71.70	0.81	151.45	30.12	106.10	135.32	271.54
Wch-32	181.92	0.4298	5.12	0.0220	16.28	6.71	408.91	353.03	29.34	791.28	104.20	323.12	189.25	616.56
Wch-33	185.92	0.4493	9.72	0.0437	28.07	15.18	602.30	612.77	85.48	1300.55	99.05	271.50	170.66	541.21
Wch-34	186.42	0.4316	8.35	0.0360	27.47	13.50	746.38	762.44	113.36	1622.18	123.84	311.47	240.86	676.18
Wch-35	187.75	0.4817	11.80	0.0568	19.36	18.95	402.23	467.74	53.02	922.99	35.50	129.84	93.77	259.11
Wch-36	191.08	0.4031	9.20	0.0371	30.08	44.67	156.59	129.27	3.65	289.51	16.32	66.10	65.34	147.75
Wch-55	191.33	0.3977	4.29	0.0171	10.19	8.04	138.84	105.93	1.44	246.21	19.63	78.90	75.84	174.36
Wch-37	192.75	0.4322	11.10	0.0480	29.92	30.92	182.66	133.72	6.57	322.95	11.53	47.07	57.02	115.62
Wch-38	193.75	0.4976	6.15	0.0306	7.41	4.34	208.66	161.46	5.21	375.34	21.70	67.99	81.56	171.25
Wch-39	195.42	0.4030	6.95	0.0280	26.54	21.31	160.64	118.58	1.87	281.10	39.28	108.33	145.56	293.17
Wch-56	203.08	0.4255	7.61	0.0324	26.42	20.35	164.78	170.59	8.71	344.08	29.76	110.31	110.88	250.94

Supplementary 1.2 The raw data of depth profiles presented in Figure 1.3.

Chapter 2 Distribution of Vanadyl and Nickel metalloporphyrins in the OAE-2 Black Shales of Demerara Rise: selective metal chelation across tetrapyrrole configurations and revised VO/(VO+Ni) proxy

Authors: Derek Parks[1*], Gregory T. Connock[1], Xiao-Lei Liu[1]

Affiliations: [1]School of Geosciences, University of Oklahoma, Norman, Oklahoma 73019, USA.

Abstract: Geoporphyrins, derived from chlorophylls, and hemes, serve as critical biomarkers for assessing paleoenvironmental redox conditions. The ratio of vanadyl (VO) to total vanadyl and nickel (Ni) porphyrins, VO/(VO+Ni), is widely used to infer depositional redox states. However, recent studies, including analysis of the Woodford Shale, have identified a chelation bias between VO and Ni with specific porphyrin classes (BiCAP and Etio), potentially skewing redox interpretations. This study examines the distribution of VO- and Ni- porphyrins in mid-Cretaceous to mid-Paleogene black shales from the Demerara Rise, utilizing the previously reported LC-ESI-qTOF-MS method. We confirm the chelation bias observed in the Woodford Shale, with VO preferentially chelating to BiCAP and Ni to Etio porphyrins proving, despite the younger age, oceanic upwelling depositional setting, and the presence of free base porphyrins in the Demerara Rise, the bias holds true. The bias between the metalloporphyrins present in the Demerara Rise eliminates the possibility of the bias being a result of differential degradation of VO- and Ni-porphyrins and supports that the bias reflects a difference in primary chelation. To address this bias, we propose a refined DPEP-focused VO/(VO+Ni) ratio, which exhibits reduced chelation bias and greater variability, enhancing its utility as a redox proxy in euxinic black shales. Our findings suggest sustained anoxic conditions at the Demerara Rise, with implications for refining paleoenvironmental reconstructions.

2.1. Introduction

Sedimentary porphyrins, or geoporphyrins, are among the earliest identified biomarkers in petroleum organic matter (Treibs, 1936). These compounds, degradation products of chlorophylls, bacteriochlorophylls, and hemes, are classified into three structural groups: bicycloalkanoporphyrins (BiCAP), deoxophylloerythroetioporphyrin (DPEP), and etioporphyrin (Etio) (Huseby et al., 1996; Turner, 1998; Callot and Ocampo, 2000; Stuart Walker and Keely, 2004). Geoporphyrins form through the loss of chelated magnesium or iron, ester-bonded isoprenoids, and functionalized side chains (e.g., vinyl, hydroxyethyl, acetyl), with further dealkylation during diagenesis reducing carbon content (Callot and Ocampo, 2000). Each

porphyrin class originates from distinct processes, complicating their use as a unified proxy for paleoenvironmental conditions. Free-base (FB) porphyrins can undergo metalation during diagenesis, forming metalloporphyrins with metals such as Fe^{2+}, Ga^{2+}, Cu^{2+}, Mn^{2+}, Co^{2+}, Ti^{2+}, Zn^{2+}, V^{2+} (as vanadyl, VO^{2+}), and Ni^{2+} (Callot and Ocampo, 2000; Junium et al., 2008; Woltering et al., 2016). Nickel and vanadyl complexes predominate, with metalation stabilizing the porphyrin macrocycle and reducing reactivity (Junium et al., 2015). The VO/(VO+Ni) ratio is a well-established proxy for depositional redox conditions, with high ratios (>0.50) indicating anoxic or euxinic environments due to Ni^{2+} precipitation as nickel sulfide under sulfidic conditions, favoring VO^{2+} chelation (Lewan and Maynard, 1982; Lewan, 1984; Huseby et al., 1996; Junium et al., 2008, 2015).

Recent studies on the Woodford Shale revealed a chelation bias between VO^{2+} and Ni^{2+} with BiCAP and Etio porphyrins, potentially compromising the VO/(VO+Ni) ratio's reliability (Parks and Liu, 2023) had confirmed observations by Sundararaman and Boreham (1993) of this bias. This study investigates the Demerara Rise black shales (mid-Cretaceous to mid-Paleogene) using the previously reported LC-ESI-qTOF-MS method (Liu, 2023) to validate this bias and to evaluate a DPEP-focused VO/(VO+Ni) ratio to improve redox assessments.

The Demerara Rise, located along the South American margin in the equatorial Atlantic, represents a classic open-ocean upwelling site and contains a stratigraphically continuous record of mid-Cretaceous to Paleogene sedimentation (Erbacher et al., 2005; Forster et al., 2007). Black shales deposited at the Demerara Rise during OAE-2 are globally recognized for high organic carbon content and exceptional preservation, reflecting sustained marine anoxia on the open continental margin in contrast to the restricted, epeiric Woodford basin. The

Demerara OAE-2 interval thus offers a key opportunity to evaluate metal chelation behavior and redox signals under distinct palaeoceanographic conditions from the Woodford Shale.

Oceanic Anoxic Event 2 (OAE-2; Cenomanian-Turonian boundary, ca. 94 Ma) is marked by globally increased organic carbon burial and profound changes in marine redox conditions (Jenkyns, 2010; Owens et al., 2016). At the Demerara Rise, OAE-2 shales are characterized by type II kerogen and low thermal maturity, preserving primary biomarker and transition metal distributions with minimal overprinting from catagenesis (Forster et al., 2004, 2007). This provides an ideal case for examining early diagenetic processes and testing the fidelity of porphyrin redox proxies.

Redox variations during OAE-2 at the Demerara rise have been extensively studied using a range of geochemical proxies, including Fe speciation, trace metals (Mo, U, V), Nitrogen isotopes, and tocopherols (Hetzel et al., 2009; Owens et al., 2012; Junium et al., 2018; Connock and Liu, 2023). While these studies document persistent water column anoxia, the reliability of porphyrin-based redox indicators remains debated due to potential chelation biases between VO^{2+} and Ni^{2+} among porphyrin structural classes. This study investigates the porphyrin-based VO/(VO+Ni) proxy within the Demerara Rise OAE-2 shales to assess the extent of such chelation bias and evaluate alternative approaches, included DPEP-focused analysis, that may provide a more accurate representation of depositional redox conditions.

2.2. Materials and Methods

2.2.1 Site of Study

The Demerara Rise, a submarine plateau off the coasts of Suriname and French Guiana, spans ~380 km and lies at depths of 700-4000 m. Ocean Drilling Program (ODP) Leg 207 recovered mid-Cretaceous (Albian) to mid-Paleogene (Lutetian) strata, including laminated black shales with thermally immature marine organic matter, particularly at Site 1258 (>3000 m depth). These shales span ~30 Ma, encompassing the Oceanic Anoxic Event 2 (OAE-2), identified by a global positive carbon isotope excursion (Scholle and Arthur, 1980; Erbacher et al., 2005). The equatorial proto-Atlantic depositional setting (500-1500 m depth) suggests persistent anoxia beyond the OAE-2.

2.2.2 Lipid Biomarker Extraction

Core samples (~150 mg) were powdered and transferred to combusted 4 mL vials. Samples were spiked with internal standards of 1 µg β-carotene for aromatic carotenoids and 100 ng C_{46} glycerol trialkyl glycerol tetraether (GTGT) for lipid recovery and normalizing metalloporphyrin concentrations. Samples were extracted with 1.5 mL dichloromethane:methanol (DCM:MeOH, 1:1 v/v), vortexed, ultrasonicated for 20 min, and centrifuged at 3000 rpm for 5 min to isolate the total lipid extract (TLE). The TLE was transferred to a combusted 2 mL vial, dried under a gentle N_2 stream, and the extraction repeated twice for a total of three extractions. The combined TLE was dried, weighed, dissolved in 1 mL MeOH, ultrasonicated for 5 min, centrifuged, and the supernatant transferred for LC-ESI-qTOF-MS analysis.

2.2.3 LC-ESI-qTOF-MS Analysis

Analysis followed Liu (2023) using an Aligent 1290 UPLC system coupled to a 6530 qTOF mass spectrometer via an Aligent Jet Stream dual electrospray ionization (AJS-ESI) interface. Nitrogen drying gas was set at 300°C and 8 $Lmin^{-1}$, with a nebulizer pressure of 35 psi. The qTOF parameters included a capillary voltage of 3.5 kV, fragmentor voltage of 175 V, skimmer voltage of 65 V, and octupole voltage of 750 V, operating in auto MS/MS mode (MS_1: *m/z* 100-2000; MS_2: *m/z* 50-2000). Samples (10 µL) were injected onto two Aligent Poroshell 120 EC-C_{18} columns (1.8 µm, 2.1 x 150 mm) in series at 35°C. The LC gradient (0.2 $mLmin^{-1}$) transitioned from 100% eluent A (95:5:0.04:0.10 methanol/H_2O/formic acid/14.8 M NH_3) to 90% A/10% B (50:50:0.04:0.10 hexane/2-propanol/formic acid/14.8 M NH_3) over 5 min, then to 35% B at 30 min, 50% B at 70 min, and re-equilibrated with 100% eluent A for 10 min.

2.2.4 Biomarker Identification and Quantification

Data were analyzed using Aligent MassHunter Qualitative Analysis software (v. B.08.00). The C_{40} aromatic carotenoids and metalloporphyrins were identified by accurate masses, MS^2 fragmentation patterns, and retention times. Isorenieratane was quantified by Connock et al., (2022) and Connock and Liu, (2023) so their values were utilized here. The VO- and Ni-porphyrins were verified by detecting chelated V^+ and Ni^+ ions under 200 eV collision-induced dissociation (CID) (Liu, 2023). Peaks were extracted via extracted ion chromatograms (EIC) and quantified relative to GTGT (metalloporphyrins) or β-carotene (isorenieratane), assuming equivalent response factors. Concentrations were normalized to total organic carbon (TOC).

2.3. Results and Discussion

2.3.1 C_{40} Aromatic Carotenoids and Photic Zone Euxinic (PZE)

Isorenieratane, a C_{40} aromatic carotenoid indicative of green sulfur bacteria (GSB) and PZE, exhibited low concentrations pre-OAE-2 (Figure 2.1), suggesting minimal PZE. Values of isorenieratane here were obtained from Connock et al., (2022). There is some slight variation in concentrations but they remain relatively low near background concentrations. Concentrations spiked at OAE-2 onset (426 mcd, meters composite depth) indicating that a strong stratification resulting in PZE at the beginning of OAE-2 took place. After this initial spike, isorenieratane concentrations dropped at 425.74 mcd indicating a collapse of PZE before rebounding at 424.84 mcd and dropping again at 423.89 mcd. This pattern appears as though OAE-2 at Demerara Rise is experiencing episodic PZE. However, these samples are discontinuous, missing data between them so it just appears to have large swings. Following the drop in concentrations of isorenieratane at 423.89 mcd, concentrations remain relatively elevated throughout, consistent with global anoxia trends (Erbacher et al., 2005) indicating a sustained, but fluctuating PZE. Post-OAE-2, isorenieratane levels returned to pre-OAE-2 values, apart for a spike at 421.19-421.04 mcd, which indicates a brief return to PZE.

2.3.2 Distribution of VO-, Ni- Porphyrins

The Demerara Rise samples contained VO^{2+}, Ni^{2+}, and free-base (FB) porphyrins across BiCAP, DPEP, and Etio classes (see Figure 2.2 for the major porphyrins detected). The VO-porphyrins include C_{31}-C_{33} BiCAP, C_{28}-C_{32} DPEP, and C_{28}-C_{32} Etio (Figure 2.2); Ni-porphyrins comprised C_{31}-C_{33} BiCAP, C_{28}-C_{32} DPEP, and C_{25}-C_{29} Etio (Figure 2.2); and FB porphyrins included

C_{31}-C_{32} BiCAP, C_{30}-C_{32} DPEP, and C_{29}-C_{31} Etio (Figure 2.2). Predominant compounds were C_{33} BiCAP (VO, Ni), C_{32} FB BiCAP, C_{32} VO-DPEP, C_{30} Ni-DPEP, C_{31} FB DPEP, C_{31} VO-Etio, C_{29} Ni-Etio, and C_{31} FB Etio, consistent with a chlorophyll-α origin.

Porphyrin concentrations followed a consistent depth profile: moderate levels pre-OAE-2, peaking at 428 mcd with some variability, declining during the OAE-2 (426-422 mcd)(Figure 2.1). and increasing post-OAE-2, with VO- and Ni-porphyrins peaking at 421.66 m, while FB porphyrins decreased. This pattern reflects oxic or suboxic surface waters pre- and post-OAE-2, supporting phytoplankton proliferations and chlorophyll/heme production, which are precursors to porphyrins. This interpretation is supported by the low concentrations of isorenieratane in pre- and post-OAE-2 samples, apart from the period between 421.19 and 421.04 mcd where isorenieratane has an abrupt increase indicating a short PZE event that is proceeded by a dramatic increase in primary productivity indicated by a spike in metalloporphyrins at 421.66 mcd (Figure 2.1). During OAE-2, a shallow persistent PZE likely suppressed phytoplankton activity, reducing porphyrin production. This reduction in primary productivity and change to a preservation dominant environment caused the positive carbon isotope excursion typically utilized to identify OAE-2. A minor porphyrin increase at 423.89 m, coinciding with an isorenieratane dip, suggests temporary PZE collapse, allowing brief phytoplankton resurgence before sustained PZE dominates again.

The VO/(VO+Ni) ratio was consistently high (>0.50) throughout most of the core (Figure 2.1), indicative of a reducing or sulfidic depositional environment (Lewan, 1984). However, it dipped to 0.49 at 425.74 mcd and 423.89 mcd during OAE-2 which was unexpected, given the widespread global anoxia during these periods. These dips likely reflect increased Ni-porphyrins

and reduction of VO-porphyrins, possibly due to shifts in phytoplankton communities or limited vanadium availability (Owens et al., 2016). The high ratio pre- and post-OAE-2 intervals, despite low C_{40} carotenoid levels indicating PZE collapse, suggests persistent anoxia in bottom waters below the photic zone. Previous analysis by Connock et al. (2022) found deep water proxies of dialkyl glycerol ethers (DAGEs) and extended archaeols ($C_{20/25}$, $C_{20/30}$, $C_{20/35}$), produced by sulfate-reducing bacteria and halophilic archaea, respectively, and have low concentrations pre- and post-OAE-2. These findings do not negate bottom water anoxia, meaning this explanation for the high ratio in these sections of the core is the most likely explanation. Notably, slight increases at OAE-2 onset and termination at 426 and 422.31 mcd mirror trends in the Woodford Shale (Parks and Liu, 2023), likely reflecting biotic responses to transitioning water column conditions from oxic to euxinic states.

2.3.3 Free-Base porphyrin Distribution

The FB porphyrins exhibited significantly higher concentrations than VO-or Ni-porphyrins throughout the Demerara Rise (Figure 2.1). This pattern can be attributed to two primary factors. First, the thermal immaturity and relatively young age of the Demerara Rise samples, which have undergone less diagenesis, reducing metal chelation and FB porphyrin degradation compared to older shales like the Woodford (Parks and Liu, 2023). Limited Diagenesis reduces the opportunity for metal chelation, thereby preserving a higher proportion of FB porphyrins and inhibiting their degradation into less stable forms. Second, a global reduction in oceanic metal ion availability during OAE-2 likely restricted the formation of metalloporphyrins (Owens et al., 2016). During the OAE-2, widespread anoxia and euxinia may have depleted bioavailable metals such as vanadium and nickel in the water column, limiting

their incorporation into porphyrin macrocycles. Consequently, the elevated FB porphyrin concentrations reflect a combination of minimal digenetic alteration and constrained metal availability, which favored the preservation of unchelated porphyrins in the sedimentary record.

The FB Etio porphyrins exhibited consistently lower concentrations relative to BiCAP and DPEP porphyrins throughout the Demerara Rise core, a pattern mirrored in VO-Etio but not Ni-Etio, where Etio concentrations were comparable to Ni-DPEP (Figure 2.3). The persistently low Etio concentrations may indicate limited production from heme or chlorophyll allomers via oxidative processes, potentially indicating that highly euxinic conditions during the OAE-2 suppressed oxidative pathways or the activity of heme-producing phototrophic organisms. However, this hypothesis is challenged by elevated porphyrin concentrations in pre- and post-OAE-2 intervals, which suggest oxygenated surface waters conducive to enhanced phototrophic production, implying sufficient conditions for chlorophyll and heme synthesis. An alternative explanation posits that FB Etio porphyrins, which lack the additional E and F ring structures of BiCAP and DPEP, are inherently less stable and more susceptible to degradation in the absence metal chelation. This instability is likely exacerbated by the reduced metal ion availability during OAE-2 (Owens et al., 2016), which limited the formation of stable metalloporphyrins. Consequently, the preferential degradation of FB Etio porphyrins, due to their simpler tetrapyrrole structure, likely contributed to their low concentrations, highlighting the combined influence of environmental conditions and molecular stability of porphyrin preservation in euxinic settings.

2.3.4 Selective Chelation and Proposed DPEP-focused Ratio

Consistent with findings from the Woodford Shale (Parks and Liu, 2023), a chelation bias was observed between VO^{2+} and Ni^{2+} with BiCAP and Etio porphyrins. The VO^{2+} preferentially chelates to BiCAP, while Ni^{2+} shows an affinity for Etio, as evidenced by relative percentage distributions. The VO-Etio porphyrins were notably scarce relative to total VO-porphyrins, and Ni-BiCAP concentrations were lower than Ni-DPEP or VO-BiCAP, though less extreme than VO-Etio (Figure 2.3). Cross-plots of VO/Ni vs. BiCAP/Etio ratios (Figure 2.4) across pre-OAE-2 (R^2=0.0853), OAE-2 (R^2=0.642), and post-OAE-2 (R^2=0.1907) confirmed this bias, though correlations were weaker than in the Woodford Shale due to low Etio concentrations and limited metal availability during OAE-2 (Owens et al., 2016). Despite lower R^2 values, the chelation bias remains evident, highlighting its potential to skew the VO/(VO+Ni) ratio's redox interpretations.

To address the observed chelation bias between vanadyl (VO) and nickel (Ni) with BiCAP and Etio porphyrins, we propose a refined VO/(VO+Ni) ratio that exclusively utilizes DPEP porphyrins. Relative percentage distributions show that DPEP porphyrins for both VO and Ni only vary slightly across the Demerara Rise core (Figure 2.3), indicating minimal chelation bias compared to BiCAP and Etio classes. By excluding BiCAP porphyrins, which are primarily influenced by non-redox-related processes such as herbivorous grazing, and Etio porphyrins, which are linked to oxidation or heme degradation (Boreham et al., 1989; Callot and Ocampo, 2000), the DPEP-focused ratio more accurately reflects the availability of redox-sensitive metals in the depositional environment. This refined ratio exhibits greater variability than the conventional VO/(VO+Ni) ratio (Figure 2.5), which incorporates all porphyrin classes and often

shows limited variation, thereby masking subtle redox fluctuations in euxinic black shales. Consequently, the DPEP-focused ratio enhances the resolution of paleoenvironmental reconstructions, enabling more precise identification of redox changes in anoxic depositional settings. A cross plot of the DPEP VO/(VO+Ni) vs VO/(VO+Ni) ratios is shown in Figure 2.6 confirms that the two ratios correlate since the linear regression has an R^2 of 0.6109.

2.4. Conclusions

Analysis of the Demerara Rise black shales confirm the selective chelation bias between VO-BiCAP and Ni-Etio porphyrins observed in the Woodford Shale (Parks and Liu, 2023), despite elevated FB porphyrin concentrations attributed to the thermal immaturity of the samples and reduced metal ion availability during OAE-2 (Owens et al., 2016). The VO/(VO+Ni) ratio indicates a persistently reducing depositional environment, with unexpected decreases during OAE-2 driven by increased Ni-porphyrins concentrations and shifts in phytoplankton community composition. High porphyrin concentrations in pre- and post-OAE-2 intervals suggest enhanced phytoplankton productivity under oxic or suboxic surface waters, whereas lower levels during the OAE-2 reflect suppression due to PZE. The weaker correlation in VO/Ni versus BiCAP/Etio cross-plots compared to the Woodford Shale results from low Etio concentrations and limited metal availability, yet the chelation bias remains evident. To address this bias, we propose a refined VO/(VO+Ni) ratio focused exclusively on DPEP porphyrins, which avoids the influence of BiCAP and Etio porphyrins formed through non-redox-related processes such as grazing and oxidation/heme degradation and exhibits stable relative percentages for VO and Ni, indicating minimal chelation bias. This DPEP-focused ratio demonstrates greater variability than the conventional VO/(VO+Ni) ratio, which includes all porphyrin classes and often lacks sufficient

variation to resolve subtle redox changes in euxinic black shales, thereby improving the precision of paleoenvironmental reconstructions.

2.5. References

Boreham, C.J., Fookes, C.J.R., Popp, B.N., Hayes, J.M., 1989. Origins of etioporphyrins in sediments: Evidence from stable carbon isotopes. Geochimica et Cosmochimica Acta 53, 2451–2455.

Callot, H.J., Ocampo, R., 2000. Geochemistry of Porphyrins. The Porphyrin Handbook, Academic Press.

Connock, G.T., Liu, X.-L., 2023. Tocopherols and associated derivatives track the phytoplanktonic response to evolving pelagic redox conditions spanning Oceanic Anoxic Event 2. Geobiology 00. doi:10.1111/gbi.12570

Connock, G.T., Owens, J.D., Liu, X.-L., 2022. Biotic induction and microbial ecological dynamics of Oceanic Anoxic Event 2. Communications Earth & Environment 3, 1–10.

Erbacher, J., Friedrich, O., Wilson, P.A., Birch, H., Mutterlose, J., 2005. Stable organic carbon isotope stratigraphy across Oceanic Anoxic Event 2 of Demerara Rise, western tropical Atlantic. Geochemistry, Geophysics, Geosystems 6. doi:10.1029/2004GC000850

Forster, A., Fredricks, H., Meyers, P.A., 2004. Molecular Biogeochemistry of Cretaceous Black Shales from the Demerara Rise: Preliminary Shipboard Results from Sites 1257 and 1258, ODP Leg 207, in: Proceedings of the Ocean Drilling Program, Initial Reports. doi:10.2973/odp.proc.ir.207.110.2004

Forster, A., Schouten, S., Baas, M., Sinninghe Damsté, J.S., 2007. Mid-Cretaceous (Albian–Santonian) sea surface temperature record of the tropical Atlantic Ocean. Geology 35, 919–922.

Hetzel, A., Böttcher, M.E., Wortmann, U.G., Brumsack, H.-J., 2009. Paleo-redox conditions during OAE 2 reflected in Demerara Rise sediment geochemistry (ODP Leg 207). Palaeogeography, Palaeoclimatology, Palaeoecology, Organic-carbon-rich sediments through the Phanerozoic: Processes, progress, and perspectives 273, 302–328.

Huseby, B., Barth, T., Ocampo, R., 1996. Porphyrins in Upper Jurassic source rocks and correlations with other source rock descriptors. Organic Geochemistry, Organic Geochemistry 25, 273–294.

Jenkyns, H.C., 2010. Geochemistry of oceanic anoxic events. Geochemistry, Geophysics, Geosystems 11. doi:10.1029/2009GC002788

Junium, C.K., Freeman, K.H., Arthur, M.A., 2015. Controls on the stratigraphic distribution and nitrogen isotopic composition of zinc, vanadyl and free base porphyrins through Oceanic Anoxic Event 2 at Demerara Rise. Organic Geochemistry 80, 60–71.

Junium, C.K., Mawson, D.H., Arthur, M.A., Freeman, K.H., Keely, B.J., 2008. Unexpected occurrence and significance of zinc alkyl porphyrins in Cenomanian–Turonian black shales of the Demerara Rise. Organic Geochemistry, Advances in Organic Geochemistry 2007 39, 1081–1087.

Junium, C.K., Meyers, S.R., Arthur, M.A., 2018. Nitrogen cycle dynamics in the Late Cretaceous Greenhouse. Earth and Planetary Science Letters 481, 404–411.

Lewan, M.D., 1984. Factors controlling the proportionality of vanadium to nickel in crude oils. Geochimica et Cosmochimica Acta 48, 2231–2238.

Lewan, M.D., Maynard, J.B., 1982. Factors controlling enrichment of vanadium and nickel in the bitumen of organic sedimentary rocks. Geochimica et Cosmochimica Acta 46, 2547–2560.

Liu, X.-L., 2023. Collision-induced dissociation as “mass spectrometric filter” for rapid screening of tetrapyrrole derivatives and their chelated metal species in complex biological and environmental samples. Rapid Communications in Mass Spectrometry 37, e9413.

Owens, J.D., Lyons, T.W., Li, X., Macleod, K.G., Gordon, G., Kuypers, M.M.M., Anbar, A., Kuhnt, W., Severmann, S., 2012. Iron isotope and trace metal records of iron cycling in the proto-North Atlantic during the Cenomanian-Turonian oceanic anoxic event (OAE-2). Paleoceanography 27. doi:10.1029/2012PA002328

Owens, J.D., Reinhard, C.T., Rohrssen, M., Love, G.D., Lyons, T.W., 2016. Empirical links between trace metal cycling and marine microbial ecology during a large perturbation to Earth’s carbon cycle. Earth and Planetary Science Letters 449, 407–417.

Parks, D.R., Liu, X.-L., 2023. Distributions of vanadyl and nickel porphyrins in the Woodford Shale and selective chelation of metal species by different tetrapyrrole configurations. Organic Geochemistry 186, 104693.

Scholle, P.A., Arthur, M.A., 1980. Carbon Isotope Fluctuations in Cretaceous Pelagic Limestones: Potential Stratigraphic and Petroleum Exploration Tool1. AAPG Bulletin 64, 67–87.

Stuart Walker, J., Keely, B.J., 2004. Distribution and significance of chlorophyll derivatives and oxidation products during the spring phytoplankton bloom in the Celtic Sea April 2002. Organic Geochemistry, Advances in Organic Geochemistry 2003. Proceedings of the 21st International Meeting on Organic Geochemistry 35, 1289–1298.

Sundararaman, P., Boreham, C.J., 1993. Comparison of nickel and vanadyl porphyrin distributions of sediments. Geochimica et Cosmochimica Acta 57, 1367–1377.

Treibs, A., 1936. Chlorophyll- und Häminderivate in organischen Mineralstoffen. Angewandte Chemie.

Turner, A., 1998. Recognition of photic zone anoxia from LC-MS studies of porphyrin distributions in ancient sediments (Doctoral dissertation). University of Bristol, Bristol, UK.

Woltering, M., Tulipani, S., Boreham, C.J., Walshe, J., Schwark, L., Grice, K., 2016. Simultaneous quantitative analysis of Ni, VO, Cu, Zn and Mn geoporphyrins by liquid chromatography-high resolution multistage mass spectrometry: Method development and validation. Chemical Geology 441, 81–91.

2.6 Figures

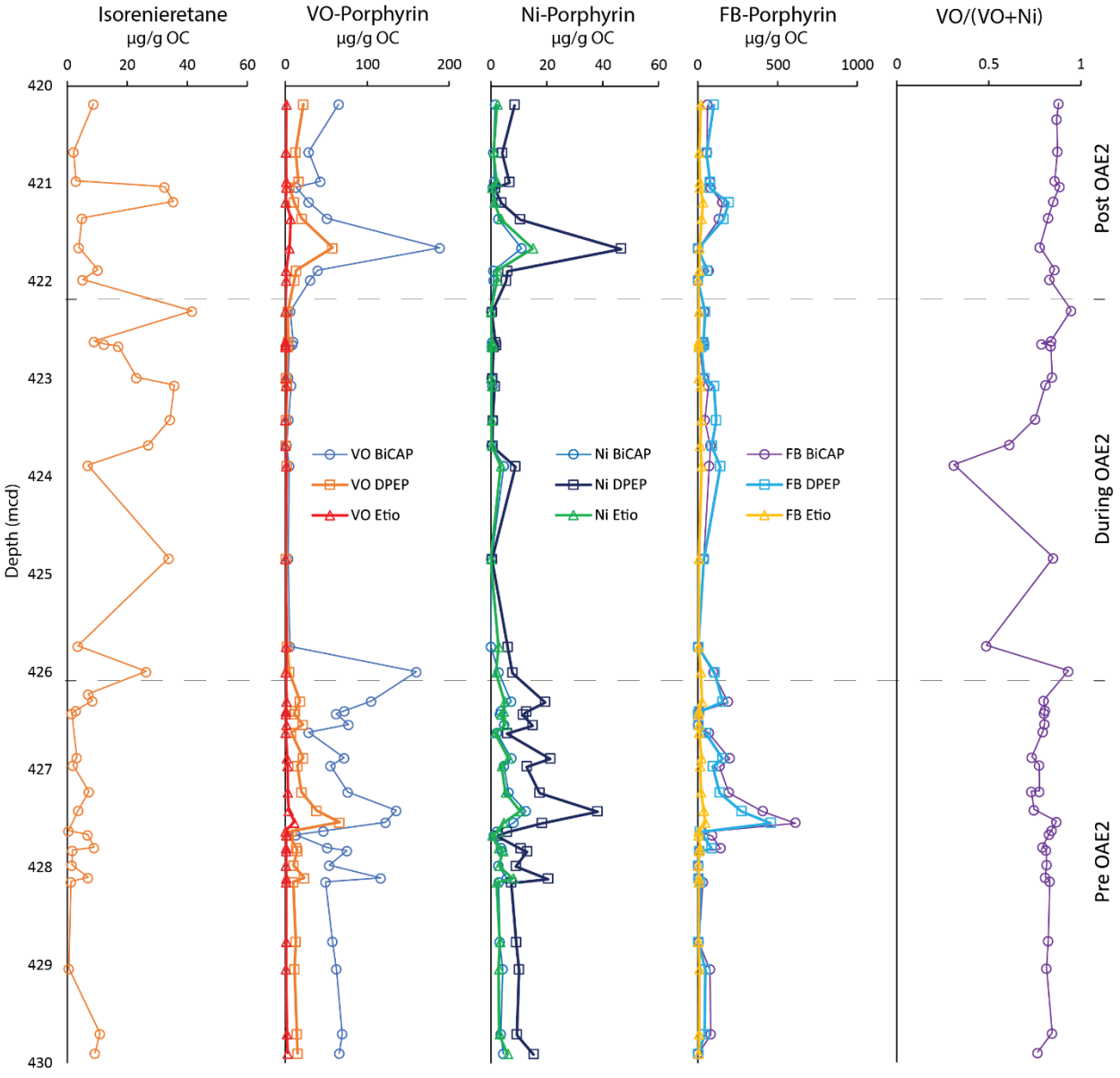


Figure 2.1 Depth profiles of isorenieratane, VO-, Ni-, and FB-porphyrins concentrations and the VO/(VO+Ni) ratio.

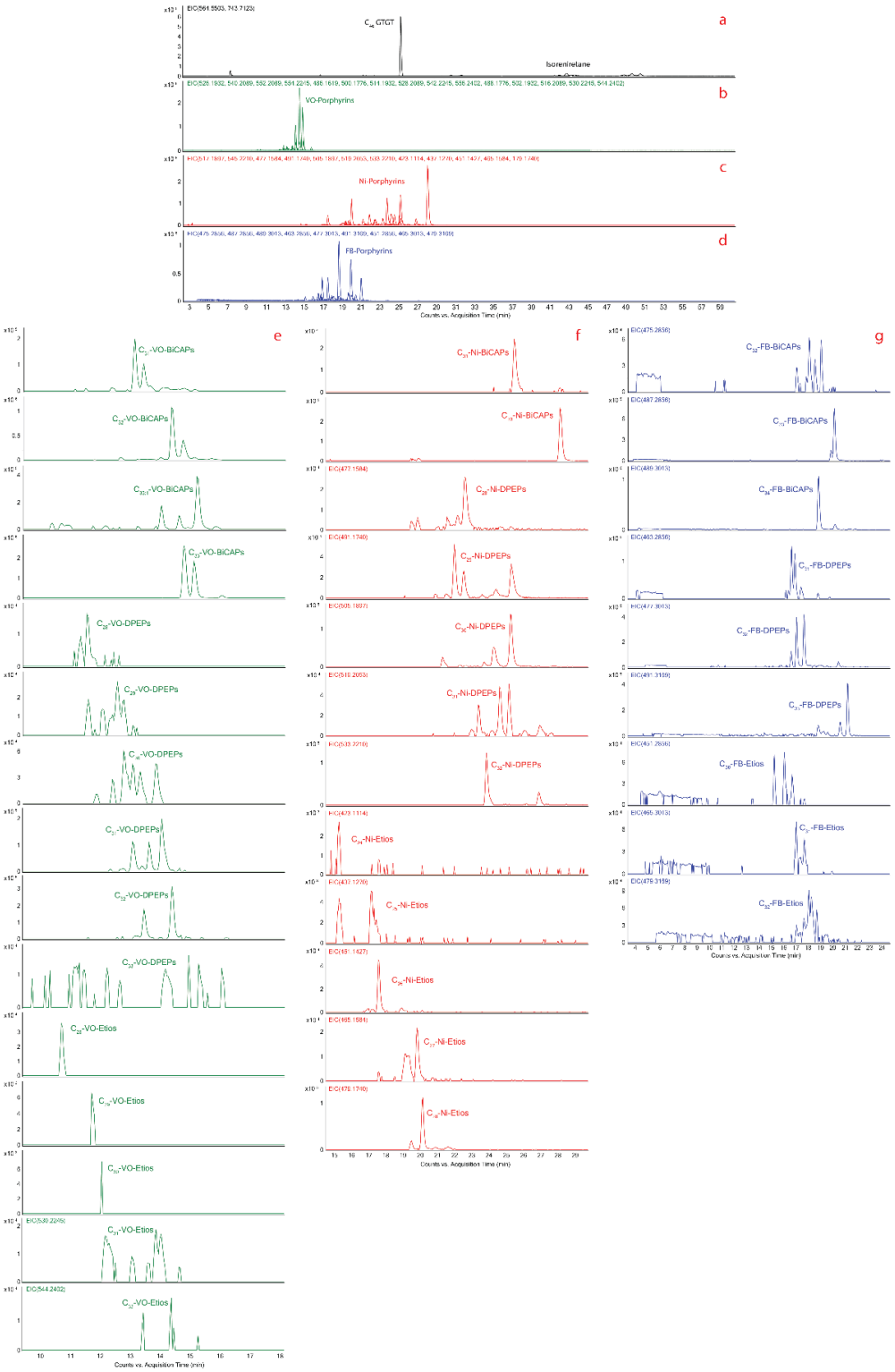


Figure 2.2 Extracted ion chromatograms (EICs) show the detection of the artificial standard, isorenieratane, major VO-, Ni-, and FB- porphyrins in the Demerara Rise. Sample 207-1258A 43-2 39-41 was used since it had relatively high curve areas across all measured molecules. (a) Combined EICs of C_{46}GTGT and isorenieratane. (b) Combined EICs of the 15 major VO-porphyrins detected. (c) Combined EICs of the 12 major Ni-porphyrins detected. (d) Combined EICs of the 9 major Free Base(FB)-porphyrins detected. (e) EICs show the detection of multiple isomers of VO-porphyrin. (f) EICs show the detection of multiple isomers of Ni-porphyrin. (g) EICs show the detection of multiple isomers of FB-porphyrin.

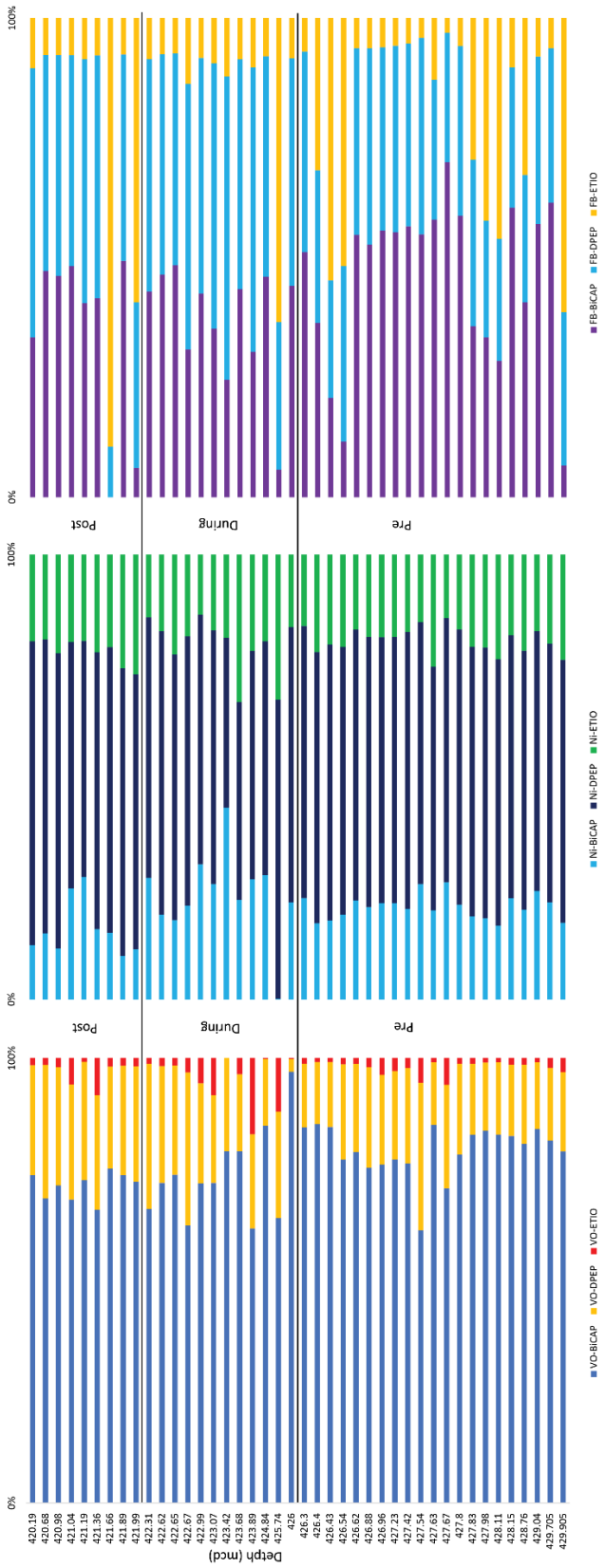


Figure 2.3 The relative abundance of BiCAP, DEPE, and Etio configurations in VO-, Ni-, and FB-porphyrins.

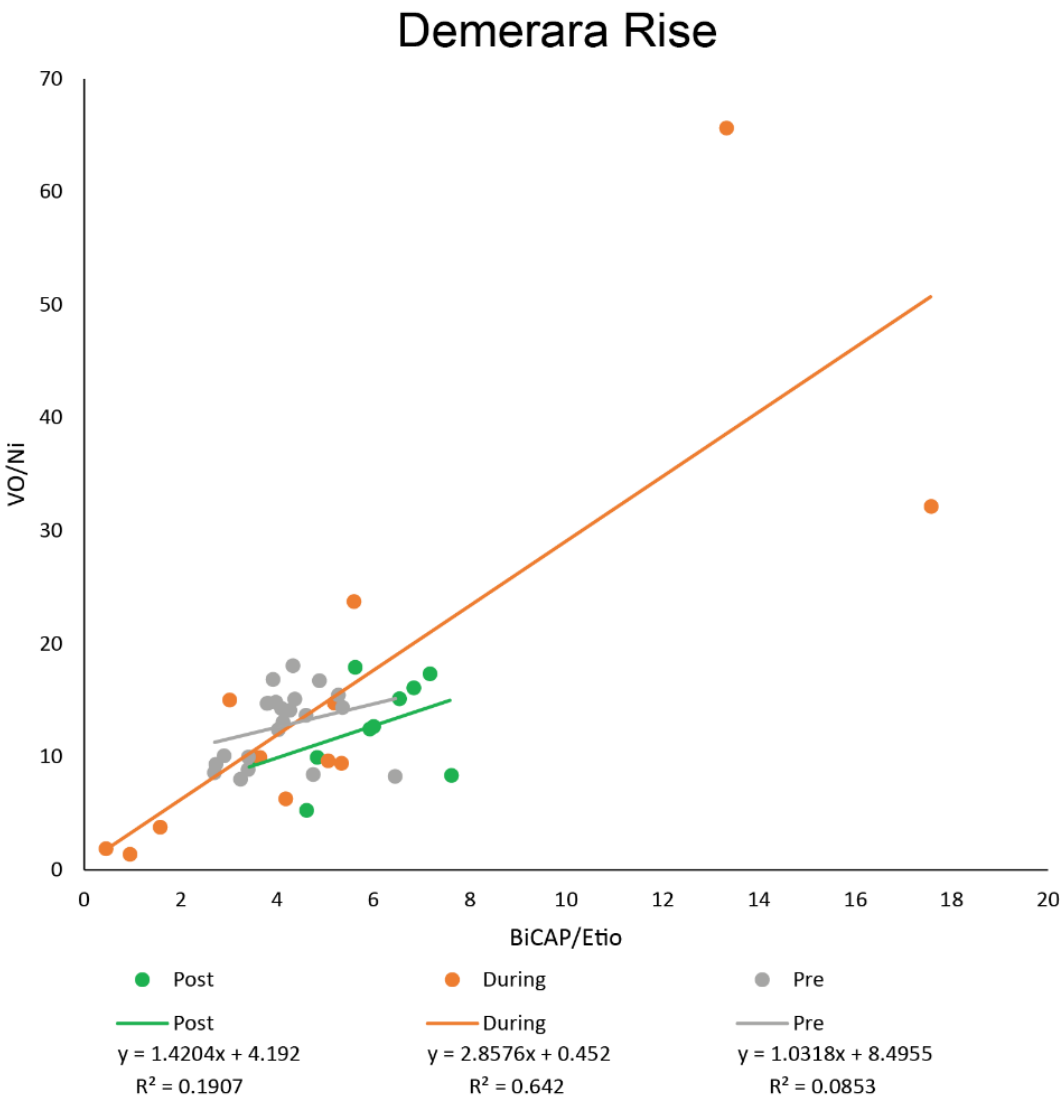


Figure 2.4 Cross plot show the correlations between VO/Ni and BiCAP/Etio for the Demerara Rise separated into the three sections pre- during and post- OAE-2 in the Demerara Rise.

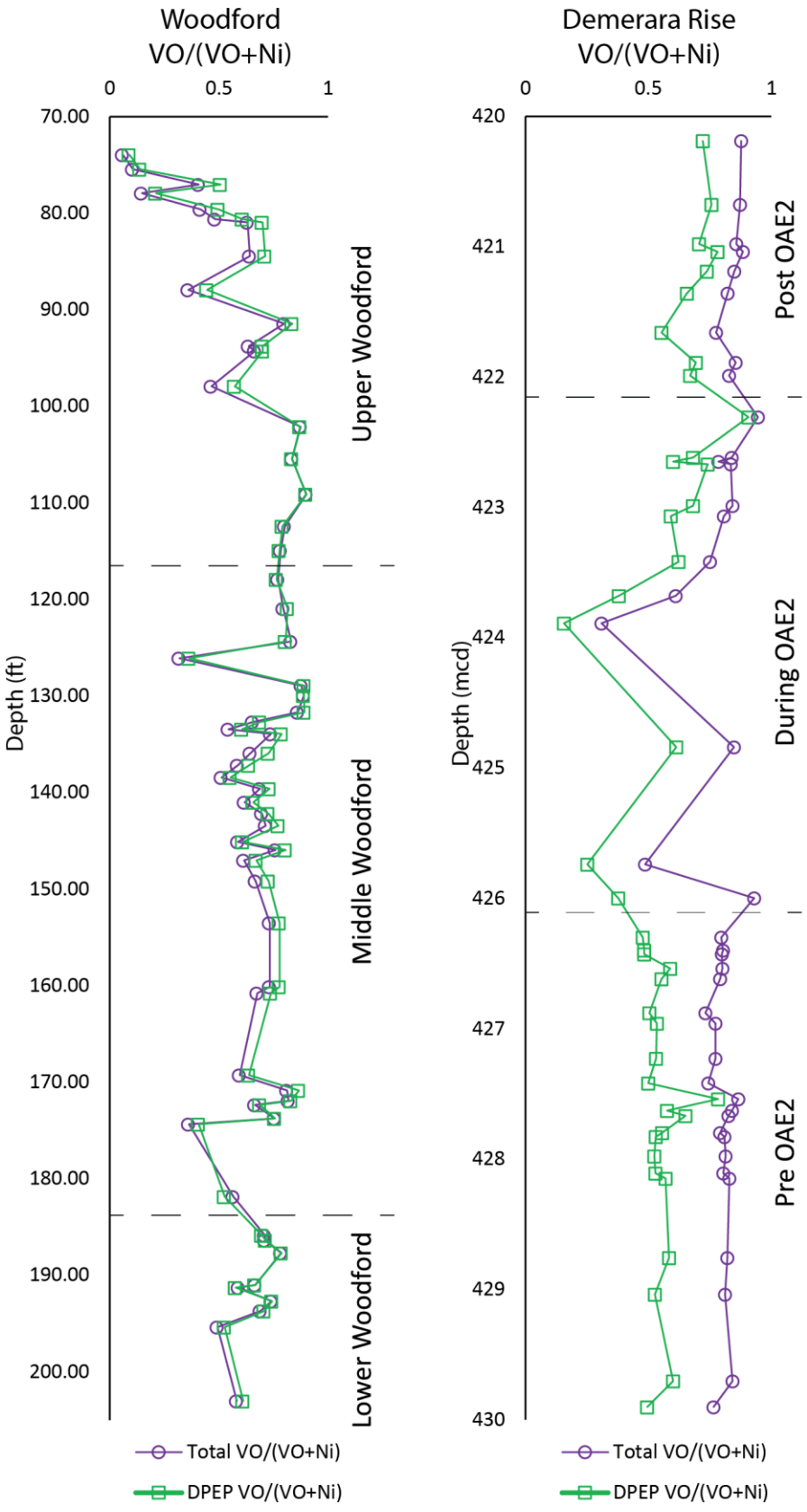


Figure 2.5 VO/(VO+Ni) ratios for both total porphyrin and DPEP porphyrin for the Woodford Shale and Demerara Rise

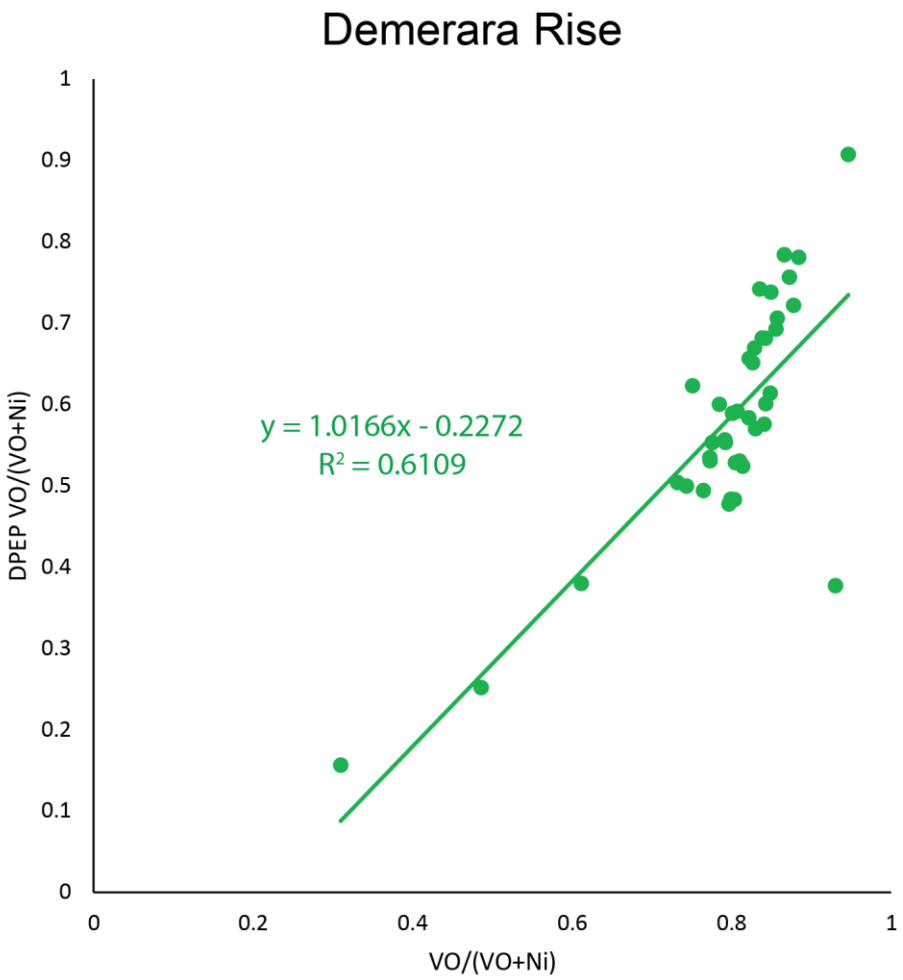


Figure 2.6 Cross plot shows the correlation between the VO/(VO+Ni) ratio and the DPEP VO/(VO+Ni) ratio for the Demerara Rise.

2.6 Supplemental

Sample	Depth	rock	TOC wt%	OC	Isorenieretane	VO-BICAP	VO-DPEP	VO-EtIo	VO Porph	Ni-BICAP	Ni-DPEP	Ni-EtIo	Ni Porph	VO/(Ni+VO)	FB-BICAP	FB-DPEP	FB-EtIo	FB Porph
	(mcd)	(g)		(g)	(ng/g OC)	(ng/g OC)	(ng/g OC)	(ng/g OC)	(ng/g OC)	(ng/g OC)	(ng/g OC)	(ng/g OC)	(ng/g OC)		(ng/g OC)	(ng/g OC)	(ng/g OC)	(ng/g OC)
207-1258B 45R-3 1-2	420.19	0.167	14.73	0.0246	8.65	65239.08	21822.26	1443.04	88504.38	1516.04	8417.14	2407.45	12340.63	0.8776	59391.01	99866.29	18705.41	177962.70
207-1258A 42-5 51-53	420.68	0.1251	16.45	0.0206	2.03	28330.50	12414.81	657.02	41402.33	902.42	3996.12	1158.55	6057.09	0.8724	57065.10	54576.44	9288.50	120930.04
207-1258B 45R-3 80-81	420.98	0.1344	11.34	0.0152	2.82	42674.19	15884.45	1249.80	59808.44	1143.84	6611.22	2206.55	9961.61	0.8572	76763.14	76595.13	12856.22	166214.49
207-1258A 42-5 87-88	421.04	0.1346	6.27	0.0084	32.40	13122.12	4978.91	1146.23	19247.27	630.79	1398.03	497.22	2526.04	0.8840	80858.68	73690.50	13046.75	167595.93
207-1258A 42-5 102-103	421.19	0.1453	5.65	0.0082	35.29	28506.68	10425.38	343.18	39275.24	1924.13	3705.85	1354.46	6984.44	0.8490	153858.01	193280.88	32463.75	379602.64
207-1258A 42-5 119-121	421.36	0.1573	8.39	0.0132	4.83	50780.61	19848.07	6483.91	77112.60	2650.60	10390.12	3672.06	16712.78	0.8219	131276.67	160155.84	24690.39	316122.89
207-1258A 42-6 17-18	421.66	0.1199	7.76	0.0093	3.76	188652.67	57581.35	4907.27	251141.29	10906.42	46539.45	15117.29	72563.16	0.7758	0.00	1291.68	10944.50	12236.18
207-1258B 45-4 30-31	421.89	0.1409	10.4	0.0147	10.12	39584.57	13178.60	932.35	53695.52	893.55	5847.35	2317.10	9058.00	0.8557	67688.17	59022.63	10464.91	137175.71
207-1258B 45R-4 40-41	421.99	0.1413	8.4	0.0119	5.04	30393.62	10891.83	806.13	42091.58	986.28	5377.88	2347.37	8711.53	0.8285	175.03	984.31	1690.16	2849.50
207-1258A 42-6 82-83	422.31	0.1349	19.86	0.0268	41.53	5947.65	2934.84	116.84	8999.33	140.08	299.64	72.43	512.15	0.9462	40142.38	45447.92	7997.88	93588.19
207-1258A 42-6 113-114	422.62	0.1316	18.84	0.0248	8.90	9309.43	3400.29	233.20	12942.91	475.44	1588.84	429.87	2494.15	0.8384	35781.97	35438.32	5844.21	77064.50
207-1258B 45R-4 106-107	422.65	0.1492	14.63	0.0218	12.20	8214.54	2731.89	192.42	11138.85	546.68	1821.60	687.13	3055.42	0.7847	41251.62	37615.53	6293.95	85161.10
207-1258A 42-6 118-119	422.67	0.1385	25.11	0.0348	16.98	4809.50	2648.11	251.08	7708.69	321.54	921.96	280.42	1523.92	0.8349	11675.51	21024.75	5198.92	37899.18
207-1258A 42-7 10-11	422.99	0.129	21.61	0.0279	22.98	3198.97	997.96	253.23	4450.17	254.03	466.89	113.04	833.96	0.8422	35437.13	41038.63	6948.73	83424.49
207-1258B 45R-4 148-149	423.07	0.1362	13.55	0.0185	35.65	6907.67	1894.66	803.61	9605.94	597.53	1308.82	392.53	2298.87	0.8069	64868.10	101988.60	17470.69	184327.39
207-1258A 42-7 53-54	423.42	0.1664	18.58	0.0309	34.17	3789.26	1000.93	0.00	4790.19	684.63	606.06	297.46	1588.15	0.7510	44283.75	114364.04	21990.47	180638.26
207-1258A 42-7 79-80	423.68	0.1596	8.35	0.0133	26.97	1542.45	337.89	71.04	1951.38	277.73	551.46	410.83	1240.02	0.6115	78682.88	86753.29	15636.86	181073.02
207-1258A 42-7 100-101	423.89	0.1206	17.27	0.0208	6.82	4707.57	1615.48	1306.74	7629.79	4600.95	8718.62	3686.49	17006.06	0.3097	71496.05	140058.92	24277.17	235832.15
207-1258C 17R-1 5-6	424.84	0.1345	20.81	0.0280	33.73	3229.88	568.28	11.12	3809.27	190.67	357.48	132.95	681.10	0.8483	37244.01	37225.23	6473.93	80943.17
207-1258C 17R-1 95-96	425.74	0.1207	12.37	0.0149	3.46	5401.60	2016.77	1013.97	8432.33	18.79	5990.31	2911.62	8920.72	0.4859	482.47	2586.71	5330.61	8399.79
207-1258C 17R-1 121-122	426	0.1251	12.31	0.0154	26.26	160167.14	4641.07	455.38	165263.59	2710.58	7664.93	2025.78	12401.29	0.9302	97705.30	104957.42	18692.81	221355.53
207-1258C 17R-2 12-13	426.3	0.1229	7.11	0.0087	8.32	104900.45	17716.53	1573.49	124190.46	7243.51	19377.88	5085.41	31706.80	0.7966	189178.17	155019.94	25893.03	370091.14
207-1258C 17R-2 22-23	426.4	0.1459	9.69	0.0141	2.80	72159.46	11791.92	753.88	84705.26	3553.43	12619.14	4546.01	20718.58	0.8035	8296.74	7272.48	7243.48	22812.70
207-1258C 17R-2 25-26	426.43	0.1432	11.04	0.0158	1.46	61953.54	10697.52	661.12	73312.18	3282.76	11441.12	3737.79	18461.67	0.7988	1982.86	2339.29	5225.61	9547.76
207-1258A 42-CCW 4-5	426.54	0.1167	9.44	0.0110		76975.34	21371.32	1426.08	99772.74	4730.27	14911.20	5154.02	24795.49	0.8009	1566.45	4935.30	6980.27	13482.01
207-1258A 43-1 14-15	426.62	0.1267	15.18	0.0192		28291.23	7089.80	471.01	35852.04	2100.06	5726.40	1587.57	9414.03	0.7920	70127.06	49987.99	8044.32	128159.38
207-1258C 17R-2 70-71	426.88	0.124	4.47	0.0055	3.13	71888.54	21554.49	2004.38	95447.41	7279.03	21212.77	6476.32	34968.12	0.7319	199064.75	154984.88	23695.01	377744.65
207-1258A 43-1 41-42	426.96	0.1333	5.81	0.0077	1.85	55186.58	14646.20	2757.94	72590.73	4639.05	12755.35	3973.21	21367.61	0.7726	136241.58	93614.64	14926.35	244782.56
207-1258A 43-1 75-76.5	427.23	0.1218	4.55	0.0055	7.14	76314.93	19632.33	2911.73	98858.99	6311.45	17374.08	5371.63	29057.16	0.7728	194313.74	136664.42	20203.67	351181.83
207-1258C 17R-3 4-5	427.42	0.1377	1.8	0.0025	3.59	135439.81	38024.56	3970.23	177434.60	12490.83	38085.99	10668.16	61244.98	0.7434	407559.83	274705.74	38155.16	720420.73
207-1258A 43-1 106-107	427.54	0.1998	0.48	0.0010		122172.05	65989.28	11073.29	199234.62	8027.37	18178.07	4684.30	30889.74	0.8658	611642.82	456929.24	46292.97	
207-1258C 17R-3 25-26	427.63	0.131	11.73	0.0154	0.40	46498.02	7701.98	520.54	54720.54	2086.14	5678.97	2619.67	10384.78	0.8405	23840.14	12005.32	5306.24	41151.70
207-1258A 43-1 119-120	427.67	0.1962	3.29	0.0065	6.73	12762.71	4207.67	1089.35	18059.73	1003.66	2253.93	544.31	3801.91	0.8261	89340.44	34565.97	3904.21	127810.62
207-1258A 43-2 4-5	427.8	0.1314	5.11	0.0067	9.90	51136.82	13347.34	827.08	65311.25	3676.14	10653.50	2898.62	17228.26	0.7913	142872.51	86312.50	14268.36	243453.38
207-1258C 17R-3 45-46	427.83	0.1382	10.92	0.0151	1.69	75165.98	14577.18	1171.88	90915.05	3990.01	12914.31	4429.96	21334.28	0.8099	8943.81	8724.48	7403.38	25071.67
207-1258C 17R-CC 2-3	427.98	0.1351	11.85	0.0160	1.43	53466.84	9809.58	664.39	63940.81	2674.14	8905.79	3053.99	14633.93	0.8138	2878.08	2100.48	3650.97	8629.53
207-1258C 17R-CC 15-16	428.11	0.1299	13.96	0.0181	6.89	116458.64	22893.62	1297.96	140650.22	5667.30	20434.11	8046.25	34147.66	0.8046	4806.32	4307.55	7784.81	16898.69
207-1258A 43-2 39-41	428.15	0.1371	12.85	0.0176	1.17	49143.56	9573.44	887.81	59604.81	2783.05	7220.26	2211.90	12215.21	0.8299	31942.73	15509.39	5440.98	52893.10
207-1258A 43-2 100-105	428.76	0.1227	11.08	0.0136		57561.53	12655.60	1083.40	71300.53	3131.46	9029.99	3350.19	15511.64	0.8213	5290.17	3455.68	4258.34	13004.18
207-1258A 43-3 2-3	429.04	0.1182	12.04	0.0142	0.44	62319.37	11101.22	728.98	74149.57	4183.67	10004.33	2950.27	17138.27	0.8123	76772.18	47055.64	10781.28	134609.10
207-1258A 43-3 68.5-70	429.705	0.1461	7.26	0.0106	10.86	69397.10	13897.29	1884.98	85179.37	3478.51	9232.61	3188.66	15899.78	0.8427	80533.73	42324.29	8235.98	131093.99
207-1258A 43-3 88.5-90	429.905	0.1421	8.75	0.0124	9.14	66072.74	14886.11	2683.11	83641.96	4464.29	15235.07	6093.96	25793.32	0.7643	662.94	3210.51	6146.84	10020.28

Supplementary 2.1 The raw data of depth profiles presented in Figure 2.1.

Chapter 3 The occurrence of diverse metalloporphyrins in the Eagle Ford and their geochemical significance

Authors: Derek Parks[1*], Xiao-Lei Liu[1], Katherine L. French[2]

Affiliations: [1]School of Geosciences, University of Oklahoma, Norman, Oklahoma 73019, USA. [2]U.S. Geological Survey, Central Energy Resources Science Center, Denver, CO 80225, USA.

Abstract: This study explores the distribution and geochemical significance of diverse metalloporphyrins, specifically vanadyl (VO), nickel (Ni), gallium (Ga), and iron (Fe) complexes, in organic-rich black shales from the Late Cretaceous Eagle Ford Formation in South Texas. Using advanced RPLC-ESI-qTOF-MS techniques on samples from the USGS Gulf Coast-3 core, the research investigates biomarker and metalloporphyrin patterns to reconstruct paleoenvironmental conditions. The VO- and Ni-porphyrin profiles, showed a chelation bias that was similarly observed in the Woodford Shale but prove to still be a reliable indicator of redox changes when utilizing the VO/(VO+Ni) ratio to track anoxic and oxic intervals. Gallium porphyrins, a novel observation in marine shales of the Eagle Ford, suggest increased terrigenous input and exhibit unique chelation behavior, while Fe-porphyrins reveal shifts in redox and sulfur dynamics through the pattern of porphyrin chelation. Stratigraphic variations of these compounds, together with isorenieratane and novel porphyrin ratios, provide fresh insights into water column chemistry, and the interplay between marine and terrestrial influences. The findings demonstrate the value of multiple proxy examinations for deciphering complex depositional histories and refining geochemical models of ancient sedimentary environments.

3.1 Introduction

The Eagle Ford Formation was deposited along the southwestern margin of the Western Interior Seaway as a nearshore epeiric shelf environment during the late Cretaceous (Surles, 1987; Liro et al., 1994). This broad, shallow marine system experienced frequent fluctuations in sea level and sediment influx, with organic-rich muds accumulating in transgressive systems tracts across both carbonate and siliclastic settings (French et al., 2024). Unlike the Demerara Rise, which represents an open-ocean upwelling margin, and the Woodford Shale, which formed along a late Devonian passive margin with strong upwelling and euxinia, the Eagle Ford's proximity to the landmasses and deltaic sources resulted in generally higher rates of sedimentation and variable oxygenation. The contrast between these three systems establishes

a diverse set of paleoenvironments in which organic-rich shales formed, each with different implications for source rock development and redox proxy interpretations.

Significantly, although the Eagle Ford records sedimentation through the Cenomanian-Turonian Ocean Anoxic Event 2 (OAE-2) (Eldrett et al., 2017; French et al., 2024), it displays evidence of persistent oxic to suboxic bottom water conditions during this interval (French et al., 2024), a contrast to the global expansion of marine anoxia apparent at the Demerara Rise and in many Woodford Shale sections. Redox proxies indicate that the Eagle Ford's OAE-2 interval was characterized by continued oxygenation, likely facilitated by active water mass exchange, shallow water depths, and proximity to terrestrial input (French et al., 2024). This stands in contrast to the classic anoxic-euxinic conditions of the Demerara Rise OAE-2 shales and many Woodford intervals, where organic matter was preserved under stable stratification and limited oxygenation. As such, the Eagle Ford provides a unique counterpoint among the examined shales of both the open-ocean Demerara rise and the more restricted, upwelling-dominated Woodford Shale.

Sedimentary porphyrins, or geoporphyrins, represent some of the earliest identified biomarkers in petroleum organic matter, first recognized by Treibs (1936). These compounds, derived from the degradation of chlorophyll, bacteriochlorophylls, and hemes encompass three primary structural classes- BiCAP, DPEP, and Etio (Huseby et al., 1996; Turner, 1998; Callot and Ocampo, 2000; Stuart Walker and Keely, 2004). Geoporphyrins form through the loss of magnesium and ester-bonded isoprenoids from chlorophyll precursors, alongside the cleavage or reduction of functionalized side chains such as vinyl, hydroxyethyl, and acetyl groups. Further diagenesis may lead to dealkylation of the tetrapyrrole core, yielding porphyrins with reduced

carbon numbers (Callot and Ocampo, 2000). Metalation during diagenesis transforms free-base geoporphyrins into metalloporphyrins, a process influenced by metal availability in the sedimentary environment (Huseby et al., 1996; Junium et al., 2008, 2015). This complexation stabilizes the porphyrin macrocycle through flattening, reducing reactivity and enhancing geologic preservation (Junium et al., 2015). Geoporphyrins can chelate various metals, including Fe, Ga, Cu, Mn, Co, Ti, Zn, V, and Ni, with nickel (Ni^{2+}) and vanadyl (VO^{2+}) complexes being most prevalent, while Fe- and Ga- porphyrins are less commonly reported (Callot and Ocampo, 2000; Junium et al., 2008; Woltering et al., 2016), they have been previously reported to exist in the Eagle Ford (Zheng et al., 2018). The Eagle Ford seems to be unique for marine sedimentary environments with the detection of Fe- and specifically Ga- porphyrins, since these are these are typically associated with coals (Bonnett and Czechowski, 1980, 1984; Bonnett and Burke, 1985; Bonnett et al., 1987). The ratio of VO- to Ni- porphyrins serves as a proxy for depositional redox conditions, with high VO/(VO+Ni) ratios (>0.50) and elevated sulfur content (>1wt%) indicating anoxic or euxinic environments where Ni^{2+} precipitates as nickel sulfide, favoring VO^{2+} complexation (Lewan and Maynard, 1982; Lewan, 1984). In contrast, oxidative conditions allow Ni^{2+} to compete effectively, increasing Ni-porphyrin abundance due to its higher equilibrium constant (Moldowan et al., 1985; Chen and Philp, 1991).

Gallium and iron porphyrins, though less studied, offer significant potential for refining paleoenvironmental and diagenetic interpretations. Gallium porphyrins are particularly valuable due to gallium's association with aluminosilicate minerals, such as clays, which are abundant in shales like the Eagle Ford. Gallium's chelation to porphyrins likely occurs during early diagenesis, reflecting the availability of Ga^{3+} in pore waters influenced by clay mineral adsorption or

weathering inputs (Filby and Van Berkel, 1987). This makes Ga-porphyrins a potential tracer of terrigenous sediment supply and diagenetic fluid chemistry, providing insights into the interplay between marine and terrestrial inputs during deposition. Furthermore, Ga-porphyrins may indicate specific redox conditions, as gallium's mobility is sensitive to pH and Eh variations (Yuan et al., 2021), potentially complementing the VO/(VO+Ni) proxy. Iron porphyrins, derived primarily from heme precursors or secondary chlorophyll degradation, offer additional clues about redox dynamics and organic matter sources. The Fe-porphyrins are particularly sensitive to redox transitions as Fe^{3+} availability is controlled by the precipitation of iron oxides or sulfides under varying Eh conditions (Fletcher et al., 1983). Their presence in sediments may reflect suboxic to anoxic transitions, where iron remains bioavailable before being sequestered as pyrite in highly reducing environments. Additionally, Fe-porphyrins can serve as biomarkers for heme-rich inputs, such as from microbial or faunal activity, thus shedding light on the ecological dynamics of the depositional environment (Tahoun et al., 2021). The combined analysis of Ga- and Fe-porphyrins alongside VO- and Ni-porphyrins enables a more nuanced reconstruction of paleoredox gradients, sediment provenance, and diagenetic pathways, enhancing our understanding of the Eagle Ford's geochemical evolution.

This study applies the previously reported RPLC-ESI-qTOF-MS method (Liu, 2023) to investigate the distribution of VO-, Ni-, Fe-, and Ga-porphyrins in the organic rich black shales of the Late Cretaceous Eagle Ford Formation in South Texas. The Eagle Ford, a prolific hydrocarbon reservoir, is characterized by high total organic carbon (TOC) and favorably low thermal maturity, making it an ideal candidate for examining metalloporphyrin distributions. Our analysis aims to elucidate the interplay of redox variation, selective metal chelation, and

tetrapyrrole structures, providing new insights into the paleoenvironmental conditions of this significant formation.

3.2 Materials and methods

3.2.1 Site of study and rock sample preparation

The Eagle Ford Group is a marine mudrock sequence deposited during the Late Cretaceous on the southeastern margin of the Western Interior Seaway (WIS) of North America (Surles, 1987; Liro et al., 1994). It is divided into two subunits labeled the lower and upper Eagle Ford. This informal boundary occurs within OAE-2 (Eldrett et al., 2017). This study uses the Gulf Coast-3 (GC-3) core sampled by the U.S. Geological Survey (USGS) in 2018. GC-3 is located approximately 30 miles south of Del Rio, Tx and 35 miles east of the Shell Iona-1 core at 29°16’25.9”N, 100°17’23.9”W (Figure 3.1). GC-3 records a Cenomanian-Turonian carbonate platform between the WIS and northern Gulf of Mexico deposited in a clastic sediment starved setting on the eastern rim of the Maverick basin. Samples and sample powdering was graciously provided to us by Dr. Kathrine French of the USGS, Denver, CO.

3.2.2 Extraction for lipid biomarker analysis

Approximately 100 mg of crushed Eagle Ford shale was transferred into a combusted 4 mL vial, and then spiked with artificial standards, 100 ng of C_{46} glycerol trialkyl glycerol tetraether (C_{46} GTGT), 1000 ng of VO-tetraphenylporphyrin (VO-TPP), and 1000 ng of Ni-TPP. Despite the lack of glycerol tetraether lipids in the Eagle Ford, we routinely included C_{46} GTGT as an internal standard to monitor the general lipid recovery of extraction. The samples then had 1.5 mL of DCM and MeOH solution (1:1, v/v) added to them and mixed with a vortexer for a few

seconds, and then sonicated in a water bath for 20 min for lipid extraction. After the extraction, samples were centrifuged for 5 min at 3000 rpm. The solvent extract was transferred into a combusted and weighted 4 mL vial which was then concentrated under a gentle N_2 stream. The same extraction process was repeated for a total of two times, then it was repeated for another two times using acetone for a total of four extractions. After the fourth extraction, the solvent of combined extract was dried completely and the vial and the total lipid extract (TLE) were weighed. After weighing the TLE, 1 mL of 1:1 Acetone:MeOH was added to the 4 mL vial to dissolve the TLE and 500 µL was transferred to a 2 mL vial. The 2 mL vial was then placed under N_2 until the sample was completely dried. Then 1 mL of MeOH was added into the dried 2 mL vial, and the vial was then ultrasonicated for 5 min and centrifuged for 5 min at 3000 rpm. The clear supernatant was then transferred into a new clean 2 mL vial for injection.

3.2.3 RPLC-ESI-qTOF-MS

Analysis was done on an Aligent 1290 series UPLC system coupled with an Aligent 6530 qTOF mass spectrometer through an Aligent jet stream dual electrospray ionization (AJS-ESI) interface. The LC-MS setup follows method description reported in (Liu, 2023). An ESI drying gas N_2 was used with a temperature set to 300°C, the flow rate of N_2 was 8 L min^{-1} with the nebulizer gas (N_2) pressure at 35 psi. The qTOF parameters were set to: capillary voltage 3.5 kV, fragmentor voltage 175 V, skimmer voltage 65 V, and octupole voltage 750 V in auto MS/MS scanning mode with an MS range of *m/z* 50-2000 and an MS/MS range of *m/z* 20-2000. The collision gas used for collision induced dissociation (CID) was N_2. Depending on the application of the CID, voltage of the collision cell was set at 40 or 200 eV. Compound separation was achieved by injecting 10 µL of sample onto an ACE UltraCore Super C_{18} column (5 µm, 2.1x250

mm, ACE, Aberdeen, UK) maintained at 45°C. The LC program was set to have a flow rate of 0.2 mL min^{-1}, from 95% A and 5% B to 40% A and 60% B in 35 min and then re-equilibrated with 95% A and 5% B at a flow rate of 0.4 mL min^{-1} for 5 min. Eluent A was 95:5:0.04:0.10 of methanol/H_2O/formic acid/14.8 M NH_3(aq.), eluent B was 50:50:0.04:0.10 of hexane/2-propanol/formic acid/14.8 M NH_3(aq.).

3.2.4 Lipid biomarker identification and quantification

Data analysis was performed using Aligent MassHunter Qualitative Analysis software (version B.08.00). C_{40} aromatic carotenoids and metalloporphyrins were identified by their accurate masses, characteristic MS^2 fragmentation patterns, and relative retention times. The occurrence of isorenieratane in the Eagle Ford has been reported by (French et al., 2024), and their identification is confirmed in this study. The identification of VO-, Ni-, Ga-, and Fe-porphyrins is further verified by the direct detection of chelated-to-porphyrin metal ions, V^+, Ni^+, Ga^+, and Fe^+, under 200 eV CID (see discussion in Liu, 2023). For quantification, targeted biomarker peaks were extracted and then integrated in EIC (extracted ion chromatogram). Concentrations of metalloporphyrins in samples were normalized to TOC and calculated using the injected internal standards, VO-TPP for VO-porphyrins, Ni-TPP for Ni-porphyrins, and Ni-TPP for Ga- and Fe-porphyrins chosen due to the good recovery of Ni-TPP, by assuming the same response factor of analytes as their corresponding artificial standards. We utilized the C_{46} GTGT to estimate the concentration variation of C_{40} aromatic carotenoids since previous work has shown poor recovery of the usual β-carotene standard but shown good data using GTGT (Parks and Liu, 2023).

3.3 Results and Discussions

3.3.1 C_{40} aromatic carotenoids and PZE

Isorenieratane concentrations exhibit significant variability throughout the core, with elevated values at the base decreasing to background levels at 182 ft (55.5 m) and remaining consistently low through the majority of the overlying succession. A notable but transient increase occurs at 140 ft (42.7 m) before returning to the previously established baseline. This stratigraphic pattern corresponds closely with previously documented observations indicating that the basal portion of the core was deposited under euxinic conditions, while the collapse of photic zone euxinia (PZE) resulting in subsequent oxygenation during and following the Oceanic Anoxic Event 2 (French et al., 2024). The observed relationship reflects the ecological dependency of green sulfur bacteria (Chlorobiaceae), which produce isorenieratane as a light-harvesting pigment under strictly anoxygenic photosynthetic conditions requiring the presence of hydrogen sulfide and light penetration. The collapse of PZE eliminates the specific environmental conditions necessary for the survival of these photoautotrophic sulfur bacteria, consequently reducing the source organisms responsible for isorenieratane production. A distinct increase during OAE-2, more clearly resolved in the expanded depth profile at 82 ft (25 m) (Figure 3.3), indicates a brief episode of moderate PZE, suggesting transient re-establishment of reducing conditions within the euphotic zone.

3.3.2 The distributions of VO- and Ni-porphyrins and redox variation

Geoporphyrins associated with VO^{2+} and Ni^{2+} consist of tetrapyrrole cores of BiCAP, DPEP, and Etio configurations. There were multiple derivatives of each category detected for

both VO- and Ni- porphyrins (see Figure 3.2 for major metalloporphyrins detected). The VO-porphyrins contain carbon numbers of C_{31}-C_{33} BiCAP, C_{29}-C_{32} DPEP, and C_{27}-C_{32} Etio. The Ni-porphyrins consist of C_{31}-C_{32} BiCAP, C_{30}-C_{32} DPEP, and C_{27}-C_{32} Etio (Figure 3.2). The predominant compounds within each category are C_{33} BiCAP, C_{32} DPEP, and C_{32} and C_{30} Etio (Figure 3.2). The dominance of C_{33}-BiCAP and C_{32}-DPEP is consistent with their proposed origin from chlorophyll-α and is similar to overserved occurrences in the Woodford Shale (Parks and Liu, 2023). C_{32}-Etio likely is produced by the reduction and decarboxylation of heme-*b* (Figure 1.1), but can also be produced by the degradation of chlorophyll-α allomers such as 15-OH-lactone-pheophytin-α. However, this degradation primarily derives C_{31}-Etio and since C_{31} is not one of the dominant compounds, it is likely C_{32} resulted from the degradation of heme.

Within the Eagle Ford Formation, VO- and Ni- porphyrin concentrations demonstrate elevated values prior and during the Mid-Cenomanian Event (MCE). The Ni-porphyrin concentrations reach maximum values during the MCE at 206 ft (62.8 m), coinciding with relatively high VO-porphyrin abundances (Figure 3.3). Following the termination of the MCE, both VO- and Ni-porphyrin concentrations exhibit a systematic decrease, maintaining moderately elevated values until the onset of OAE-2. During the initiation of OAE-2, concentrations decline further, reaching minimum values throughout the event interval. This reduction in detectable metalloporphyrins chelated to both vanadyl and nickel reflects diminished preservation potential during OAE-2 in the Eagle Ford Formation, as evidenced by correspondingly low total organic carbon (TOC) values in these samples (Figure 3.3). The reduced preservation potential can be attributed to water column oxygenation experienced during OAE-2 (Denne et al., 2014; Lowery et al., 2017; French et al., 2024).

The VO/(VO+Ni) ratio maintains elevated values (>0.5) throughout most of the succession until the onset of the OAE-2, where it exhibits a systematic decrease, with values dropping below 0.5 at 102 ft (31.1 m) coinciding with the initiation of the OAE-2 (Figure 3.3). This pattern corroborates previous research suggesting oxic conditions during the OAE-2 in the Eagle Ford Formation and validates the continued utility of the VO/(VO+Ni) ratio as a paleoredox proxy despite documented issues with selective metal chelation in other sedimentary sequences (Parks and Liu, 2023). The ratio also indicates the transient return of euxinic conditions during OAE-2, reaching a local maximum at 82 ft (25 m), which corresponds with the observed increase in isorenieratane at the same depth interval (Figure 3.3). This spike in the ratio is also observed in multiple other biomarkers including the TOC, porphyrins, isorenieratane, and the Pr/Ph ratio which coincides with a transition from transgression through the entire core to a reversion to a short regression (French et al., 2024).

The general stratigraphic distribution patterns of both VO- and Ni-porphyrins exhibit similar profiles to isorenieratane, indicating that preservation potential within the core is significantly influenced by water column stratification and the development of euxinic conditions. Under oxygenated water column conditions, enhanced organic matter oxidation resulted in diminished preservation of detectable porphyrin compounds.

Heme in ocean water is produced in concentrations that reflect primary productivity of phytoplankton and zooplankton, utilized for oxygen transport in cellular respiration (Louropoulou et al., 2019). Heme-derived porphyrins in the form of C_{32} etioporphyrin (Etio) display comparable depth profiles for both VO- and Ni-chelated compounds, mirroring the total metalloporphyrin distributions. Since C_{31}-Etio is not one of the dominant members it is likely

that the majority of C_{32}-Etio is derived from the degradation of heme-*b* rather than chlorophyll. The parallel stratigraphic patterns between heme-derived Etio and other porphyrin types indicate that the observed metalloporphyrins are primarily sourced from phytoplankton, similar to heme-derived Etio, rather than from alternative sources. The heme-derived Etio/total porphyrin ratio exhibits moderately elevated values during the MCE but demonstrates a decreasing trend up-section (Figure 3.4). This pattern follows the general trend of the concentrations of both heme-derived porphyrins and total porphyrins apart from an increase in total porphyrin concentration at 82 ft (25 m). The ratio decreases until the onset of OAE-2 and increases right before OAE-2 at 102 ft (31.1 m) and then decreases again through OAE-2 and begins increasing again after 80 ft (24.4 m) (Figure 3.4). The pattern of the C_{32}-Etio/total porphyrin ratio is roughly inverse to the VO/(VO+Ni) ratio (Figure 3.3) within the onset and OAE-2. This inversion of the VO/(VO+Ni) ratio is likely due to oxygenation since it resembles the trends of the Pr/Ph ratio (Figure 3.3). Variation in the C_{32}-Etio/total porphyrin ratio are small, appearing significant only because of the scale of the profile in Figure 3.4. This confirms that they are closely tied to the producer of other porphyrins, being phytoplankton in this setting.

3.3.3 Ga- and Fe-porphyrins

Gallium porphyrins were detected in these samples, representing an unusual occurrence for marine porphyrins but corroborating other results for the Eagle Ford by Zheng et al. (2018). Notably, no Ga-etioporphyrins were detected; only bixycloalkanoporphyrin (BiCAP) and deoxophylloerythroethioporphyrin (DPEP) structures were observed to complex with gallium. The Ga-porphyrins contain carbon numbers C_{31}-C_{33} BiCAP, C_{30}-C_{32} DPEP with C_{33} BiCAP and C_{32} DPEP being the predominant compounds (Figure 3.2).

Gallium porphyrins follow similar distributional trends to VO- and Ni-porphyrins, exhibiting elevated concentrations at the base of the core and during the MCE (Figure 3.3). However, unlike VO- and Ni-porphyrins, Ga-porphyrin concentrations decrease more precipitously at the termination of the MCE and remain at background levels throughout the middle portion of the core. Concentrations exhibit a notable spike at 140 ft (42.7 m), corresponding to concurrent increases in VO- and Ni-porphyrin abundances in the same interval, before gradually decreasing into the pre-OAE-2 interval and returning to low concentrations (Figure 3.3). Given the proximity of the Eagle Ford depositional setting to the Cretaceous paleo-shoreline, gallium porphyrins may serve as indicators of terrestrial input, as gallium can be mobilized from continental sources during weathering processes and gallium found in seawater is primarily derived from aeolian and fluvial inputs (Orians and Bruland, 1988; Shiller, 1998; Yuan et al., 2021). Gallium here could be indicating enhanced terrestrial inputs resulting in both the increase of Ga-porphyrins and the corresponding enhanced preservation of OM observed as a result of possible algal blooms from fertilization.

Iron porphyrins in the Eagle Ford Formation exhibit distinctive chelation behavior throughout the succession. Iron exclusively complexes with BiCAP structures through most of the core until the initiation of OAE-2, when chelation extends to DPEP and Etio structures. The Fe-porphyrins contain carbon numbers C_{32}-C_{33} BiCAP, C_{28}-C_{33} DPEP, and C_{27}-C_{32} Etio (Figure 3.2). The predominant compounds are C_{33} BiCAP, C_{32} DPEP, and C_{31} and C_{30} Etio. For the Fe-BiCAPs the second major peak is the Fe-BiCAP not the first, similarly for C_{33}-Fe-DPEP the first peak is an isotope of VO-porphyrin and the second peak is Fe-DPEP.

When comparing this pattern to the S/Fe ratio in Figure 3.5 Fe begins to complex with DPEP and Etio when the ratio begins to decrease. The beginning of when DPEP and Etio begins chelating with Fe is more easily seen on the relative percent chart in Figure 3.6. The S/Fe ratio begins decreasing at 136 ft (41.5 m) which is the same depth that the first Fe-Etioporphyrin is observed (Figure 3.5). While the S/Fe ratio does not reach below the pyrite ratio until 118 ft (36 m) it does indicate lower sulfur that is present for much of the rest of the core which could explain the change in chelation habit of the iron. We suggest that the driving factor for iron chelation to DPEP and Etio is the sulfur concentration in the water column. When sulfur is high it forms pyrite with iron preventing chelation to DPEP and Etio. This is also seen in yet unpublished data for the Green River Shale, a lacustrine environment lacking sulfur, where iron is observed to chelate to DPEP and Etio but no detected Fe-BiCAP is present. The lack of observed Fe-BiCAP in the lacustrine environment can be explained by the provenance of BiCAP being herbivorous grazing of phytoplankton and lack of those organisms present. We propose a new ratio, the Fe-BiCAP/total Fe-porphyrin ratio, in conjunction with the VO/(VO+Ni) ratio has a possibility to provide better clarification of environmental factors such as the redox and sulfur content conditions than the VO/(VO+Ni) ratio alone. Comparing the two in Figure 3.5 they have similar depth profiles but the Fe-BiCAP/Fe-porphyrin ratio begins decreasing before the VO/(VO+Ni) ratio, indicating that a change in water column chemistry is already beginning. The new ratio does not show utility in euxinic conditions since the ratio is just 1 as only Fe-BiCAP is detected but as conditions begin to become less sulfidic and more oxic the ratio provides an earlier indicator of those changes than the VO/(VO+Ni) ratio alone. This novel ratio seems fallible in some cases. For example, at 198 ft (60.4 m) the S/Fe ratio dips to 1.22, almost

reaching the 1.15 pyrite ratio and is lower than the ratio at 136 ft (41.5 m) where the Fe-BiCAP/Fe-porphyrin ratio begins detecting a change. This short dip is seen in other biomarkers such as isorenieratane, the porphyrins, and TOC indicating a rapid loss of preservation likely due to an oxic event. This might be explained by the lack of preservation and short nature of the oxic event as to why the ratio does not show a change here but the VO/(VO+Ni) ratio shows an increase here, counter to what is expected. Perhaps there are other factors at play preventing these ratios from showing this change.

3.3.4 Metalloporphyrin relative abundance and the implications

Throughout the Eagle Ford Formation, VO-BiCAP exhibits preferential chelation until the onset of OAE-2, where its relative abundance begins to decrease systematically (Figure 3.6). This pattern corresponds with documented water column oxygenation during the OAE-2 in the Eagle Ford Formation. Conversely, Ni-Etio demonstrates consistent preferential chelation throughout the entire succession without systematic changes correlating with OAE-2 initiation. The selective chelation of VO- and Ni-porphyrins to BiCAP and Etio structures, respectively, observed in the Eagle Ford Formation confirms similar chelation biases documented in the Woodford Shale and Demerara Rise, demonstrating consistent behavior across diverse depositional settings (Parks and Liu, 2023). This selective chelation was explained by mechanical differences in the porphyrin molecules and the bonding configuration of the chelated metals. The BiCAP is more ridged due to its two extra E and F ring structures (Figure 1.1), preventing chelation with nickel which prefers a square planar configuration in the plane of the porphyrin, while vanadyl with its square pyramidal configuration can be outside of the plane of the porphyrin and not require the same bond angles and lengths that are required by nickel. The Etio lacks the two extra E and F

rings so it can more easily conform and shift to the bond lengths and angles required to chelate nickel which results in the lack of Ni-BiCAP and the favor and VO-BiCAP.

Gallium porphyrins, as discussed previously, likely indicate terrestrial inputs, and their chelation preferences are not controlled by the same structural or redox mechanisms governing VO- and Ni-porphyrin behavior. Notably, gallium does not appear to chelate with Etio structures, suggesting some degree of structural selectivity, although this cannot be explained through the same mechanisms as VO- and Ni- structural selectivity. Gallium typically has an octahedral coordination structure when chelating with most ligands (de la Fuente et al., 2023; Pantović et al., 2024), but when coordinated to more ridged molecules the geometry can change with gallium being outside the plane of coordination resulting in a more square pyramidal coordination (Price et al., 2020; de la Fuente et al., 2023) similar to what is observed with vanadyl possibly explaining the preference to chelate to BiCAP and DPEP.

Iron demonstrates exclusive chelation to BiCAP throughout the core succession until OAE-2 onset and duration, supporting the hypothesis that iron chelation to DPEP and Etio is controlled by excess sulfur in the water column. The absence of Fe-DPEP and Fe-Etio complexation until oxygenation commences corresponds to the loss of excess sulfide. The beginning of this change is easily seen in Figure 3.6 as Etio begins to be chelated. Iron chelates in an octahedral coordination with a square planar configuration within the plane of the porphyrin (Khorasani-Motlagh et al., 2009). This supports the idea that the lack of chelation to DPEP and Etio through much of the sequence is due to changes in water chemistry instead of a structural aspect like is observed with VO- and Ni-porphyrins.

3.3.5 Ash bed indications and the biologic response

Volcanic ash input has traditionally been considered a major contributor to iron supply in surface ocean systems (Berger and Wefer, 1991). However, recent research emphasizes the importance of iron sources from benthic supplies derived from continental margin sediments (Lam et al., 2020). Volcanic ash beds identified within the GC-1 core do not exhibit direct correlations with detected Fe-porphyrin concentrations (Figure 3.7), nor do they correlate with increases of other biomarkers that would indicate an algal bloom from the available nutrients. While some ash bed occurrences precede Fe-porphyrin increases, they do not appear to initiate the observed iron concentration changes as there is an increase beginning before the ash bed. This lack of direct correlation does not necessarily indicate that volcanic ash beds are not sources of bioavailable iron for the Eagle Ford system; rather, it suggests that ash deposition did not trigger measurable biological responses preserved in the biomarker record. Biological responses appear to lag significantly behind all documented ash bed occurrences in the Eagle Ford Formation, which is unusual given that enhanced preservation and primary productivity typically increase following the introduction of nutrient-rich volcanic ash (Langmann et al., 2010).

3.4 Conclusion

The stratigraphic distribution of isorenieratane aligns with previous findings (French et al., 2024), indicating that the MCE and pre-OAE-2 intervals represent euxinic conditions within the Eagle Ford Formation, transitioning toward oxic conditions, followed by diminished isorenieratane concentrations during OAE-2 consistent with water column oxygenations. The VO- and Ni-porphyrins demonstrate chelation bias similar to observations from the Woodford

Shale (Parks and Liu, 2023) and Demerara Rise, with selective chelation occurring not only in euxinic and anoxic intervals but also in oxygenated strata. Despite this documented chelation bias, the VO/(VO+Ni) ratio remains valid as a proxy for euxinia and oxygenation. The ratio maintains elevated values (>0.5) throughout most of the core succession and decreases only during OAE-2, where values below 0.5 indicate oxygenated environmental conditions. The ratio also records the brief return of photic zone euxinia during OAE-2, evidenced by increased isorenieratane at 82 ft (25 m). Gallium porphyrins detected in these samples likely represent terrestrial sources and lack detectable Etio structures, possibly explained by structural selectivity mechanisms similar to those governing VO- and Ni-porphyrin behavior. The source of gallium in the Eagle Ford Formation requires identification in future studies to determine the environmental significance of their detection. Iron porphyrins exclusively chelate to BiCAP until OAE-2 onset and duration, when chelation extends to DPEP and Etio structures. This pattern likely results from the loss of excess sulfur in the Eagle Ford Formation, as DPEP and Etio chelation with iron occurs only during expanded oxygenated desulfurized water column conditions. The preferential chelation of iron among BiCAP, DPEP, and Etio structures could serve as a sulfide proxy using the Fe-BiCAP/Fe-porphyrin ratio and in conjunction with the VO/(VO+Ni) ratio could serve as a valuable tool in identifying sulfide and redox changes in the paleo-water column, pending future research to develop a mechanistic understanding of the controlling processes.

3.5 References

Berger, W.H., Wefer, G., 1991. Productivity of the glacial ocean: Discussion of the iron hypothesis. Limnology and Oceanography 36, 1899–1918.

Bonnett, R., Burke, P.J., 1985. Iron porphyrins in coal from the United States. Geochimica et Cosmochimica Acta 49, 1487–1489.

Bonnett, R., Burke, P.J., Czechowski, F., 1987. Metalloporphyrins in Lignite, Coal, and Calcite, in: Metal Complexes in Fossil Fuels, ACS Symposium Series. American Chemical Society, pp. 173–185.

Bonnett, R., Czechowski, F., 1980. Gallium porphyrins in bituminous coal. Nature 283, 465–467.

Bonnett, R., Czechowski, F., 1984. Metalloporphyrins in coal. 1. Gallium porphyrins in bituminous coals. Journal of the Chemical Society, Perkin Transactions 1 125–131.

Callot, H.J., Ocampo, R., 2000. Geochemistry of Porphyrins. The Porphyrin Handbook, Academic Press.

Chen, J.H., Philp, R.P., 1991. Porphyrin distributions in crude oils from the Jianghan and Biyang basins, China. Chemical Geology, Trace Metals in Petroleum Geochemistry 91, 139–151.

de la Fuente, M.C., Ageitos, L., Lages, M.A., Martínez-Matamoros, D., Forero, A.M., Balado, M., Lemos, M.L., Rodríguez, J., Jiménez, C., 2023. Structural Requirements for Ga3+ Coordination in Synthetic Analogues of the Siderophore Piscibactin Deduced by Chemical Synthesis and Density Functional Theory Calculations. Inorganic Chemistry 62, 7503–7514.

Denne, R.A., Hinote, R.E., Breyer, J.A., Kosanke, T.H., Lees, J.A., Engelhardt-Moore, N., Spaw, J.M., Tur, N., 2014. The Cenomanian–Turonian Eagle Ford Group of South Texas: Insights on timing and paleoceanographic conditions from geochemistry and micropaleontologic analyses. Palaeogeography, Palaeoclimatology, Palaeoecology, Selected Papers, Geologic Problem Solving with Microfossils3 413, 2–28.

Eldrett, J.S., Dodsworth, P., Bergman, S.C., Wright, M., Minisini, D., 2017. Water-mass evolution in the Cretaceous Western Interior Seaway of North America and equatorial Atlantic. Climate of the Past 13, 855–878.

Filby, R.H., Van Berkel, G.J., 1987. Geochemistry of Metal Complexes in Petroleum, Source Rocks, and Coals: An Overview, in: Metal Complexes in Fossil Fuels, ACS Symposium Series. American Chemical Society, pp. 2–39.

Fletcher, W.K., Holmes, G.S., Lewis, A.G., 1983. Geochemistry and biological availability of iron and trace elements in the upper Fraser River estuary. Marine Chemistry, Symposium on Marine Chemistry 12, 195–217.

French, K.L., Flaum, J.A., Birdwell, J.E., 2024. An integrated perspective of paleoenvironmental change in the Western Interior Seaway before and during OAE-2 reveals how organic-

rich mudstones form in dynamic environments. Earth and Planetary Science Letters 642, 118850.

Huseby, B., Barth, T., Ocampo, R., 1996. Porphyrins in Upper Jurassic source rocks and correlations with other source rock descriptors. Organic Geochemistry, Organic Geochemistry 25, 273–294.

Junium, C.K., Freeman, K.H., Arthur, M.A., 2015. Controls on the stratigraphic distribution and nitrogen isotopic composition of zinc, vanadyl and free base porphyrins through Oceanic Anoxic Event 2 at Demerara Rise. Organic Geochemistry 80, 60–71.

Junium, C.K., Mawson, D.H., Arthur, M.A., Freeman, K.H., Keely, B.J., 2008. Unexpected occurrence and significance of zinc alkyl porphyrins in Cenomanian–Turonian black shales of the Demerara Rise. Organic Geochemistry, Advances in Organic Geochemistry 2007 39, 1081–1087.

Khorasani-Motlagh, M., Noroozifar, M., Saffari, J., Naeimi, A., Patrick, B.O., 2009. Synthesis, molecular structure, and properties of six-coordinate iron(III) porphyrin, [OEPFe(Pz)2]ClO4. Inorganica Chimica Acta 362, 2861–2867.

Lam, P.J., Heller, M.I., Lerner, P.E., Moffett, J.W., Buck, K.N., 2020. Unexpected Source and Transport of Iron from the Deep Peru Margin. ACS Earth and Space Chemistry 4, 977–992.

Langmann, B., Zakšek, K., Hort, M., Duggen, S., 2010. Volcanic ash as fertiliser for the surface ocean. Atmospheric Chemistry and Physics 10, 3891–3899.

Lewan, M.D., 1984. Factors controlling the proportionality of vanadium to nickel in crude oils. Geochimica et Cosmochimica Acta 48, 2231–2238.

Lewan, M.D., Maynard, J.B., 1982. Factors controlling enrichment of vanadium and nickel in the bitumen of organic sedimentary rocks. Geochimica et Cosmochimica Acta 46, 2547–2560.

Liro, L.M., Dawson, W.C., Katz, B.J., Robison, V.D., 1994. Sequence Stratigraphic Elements and Geochemical Variability within a 44.

Liu, X.-L., 2023. Collision-induced dissociation as “mass spectrometric filter” for rapid screening of tetrapyrrole derivatives and their chelated metal species in complex biological and environmental samples. Rapid Communications in Mass Spectrometry 37, e9413.

Louropoulou, E., Gledhill, M., Browning, T.J., Desai, D.K., Barraqueta, J.-L.M., Tonnard, M., Sarthou, G., Planquette, H., Bowie, A.R., Schmitz, R.A., LaRoche, J., Achterberg, E.P., 2019. Regulation of the Phytoplankton Heme b Iron Pool During the North Atlantic Spring Bloom. Frontiers in Microbiology 10. doi:10.3389/fmicb.2019.01566

Lowery, C.M., Cunningham, R., Barrie, C.D., Bralower, T., Snedden, J.W., 2017. The Northern Gulf of Mexico During OAE2 and the Relationship Between Water Depth and Black Shale Development. Paleoceanography 32, 1316–1335.

Moldowan, J.M., Seifert, W.K., Gallegos, E.J., 1985. Relationship Between Petroleum Composition and Depositional Environment of Petroleum Source Rocks1. AAPG Bulletin 69, 1255–1268.

Orians, K.J., Bruland, K.W., 1988. The marine geochemistry of dissolved gallium: A comparison with dissolved aluminum. Geochimica et Cosmochimica Acta 52, 2955–2962.

Pantović, B.V., Ašanin, D.P., Perdih, F., Radanović, D.D., Turel, I., Djuran, M.I., Glišić, B.Đ., 2024. Gallium(III) complexes with 1,3-pdta-type of ligands: The influence of an alkyl substituent in 1,3-propanediamine chain and the metal counter cation on the structural properties of the complex. Polyhedron 258, 117045.

Parks, D.R., Liu, X.-L., 2023. Distributions of vanadyl and nickel porphyrins in the Woodford Shale and selective chelation of metal species by different tetrapyrrole configurations. Organic Geochemistry 186, 104693.

Price, T.W., Yap, S.Y., Gillet, R., Savoie, H., Charbonnière, L.J., Boyle, R.W., Nonat, A.M., Stasiuk, G.J., 2020. Evaluation of a Bispidine-Based Chelator for Gallium-68 and of the Porphyrin Conjugate as PET/PDT Theranostic Agent. Chemistry (Weinheim an Der Bergstrasse, Germany) 26, 7602–7608.

Shiller, A.M., 1998. Dissolved gallium in the Atlantic Ocean. Marine Chemistry 61, 87–99.

Stuart Walker, J., Keely, B.J., 2004. Distribution and significance of chlorophyll derivatives and oxidation products during the spring phytoplankton bloom in the Celtic Sea April 2002. Organic Geochemistry, Advances in Organic Geochemistry 2003. Proceedings of the 21st International Meeting on Organic Geochemistry 35, 1289–1298.

Surles, M.A., 1987. Stratigraphy of the Eagle Ford Group (Upper Cretaceous) and its source-rock potential in the East Texas Basin. Baylor Geological Studies Bulletin 45.

Tahoun, M., Gee, C.T., McCoy, V.E., Sander, P.M., Müller, C.E., 2021. Chemistry of porphyrins in fossil plants and animals. RSC Advances 11, 7552–7563.

Treibs, A., 1936. Chlorophyll- und Häminderivate in organischen Mineralstoffen. Angewandte Chemie.

Turner, A., 1998. Recognition of photic zone anoxia from LC-MS studies of porphyrin distributions in ancient sediments (Doctoral dissertation). University of Bristol, Bristol, UK.

Woltering, M., Tulipani, S., Boreham, C.J., Walshe, J., Schwark, L., Grice, K., 2016. Simultaneous quantitative analysis of Ni, VO, Cu, Zn and Mn geoporphyrins by liquid chromatography-high resolution multistage mass spectrometry: Method development and validation. Chemical Geology 441, 81–91.

Yuan, W., Chen, J., Teng, H., Chetelat, B., Cai, H., Liu, J., Wang, Z., Bouchez, J., Moynier, F., Gaillardet, J., Schott, J., Liu, C., 2021. A Review on the Elemental and Isotopic Geochemistry of Gallium. Global Biogeochemical Cycles 35, e2021GB007033.

Zheng, F., Hsu, C.S., Zhang, Y., Sun, Y., Wu, Y., Lu, H., Sun, X., Shi, Q., 2018. Simultaneous Detection of Vanadyl, Nickel, Iron, and Gallium Porphyrins in Marine Shales from the Eagle Ford Formation, South Texas. Energy & Fuels 32, 10382–10390.

3.6 Figures

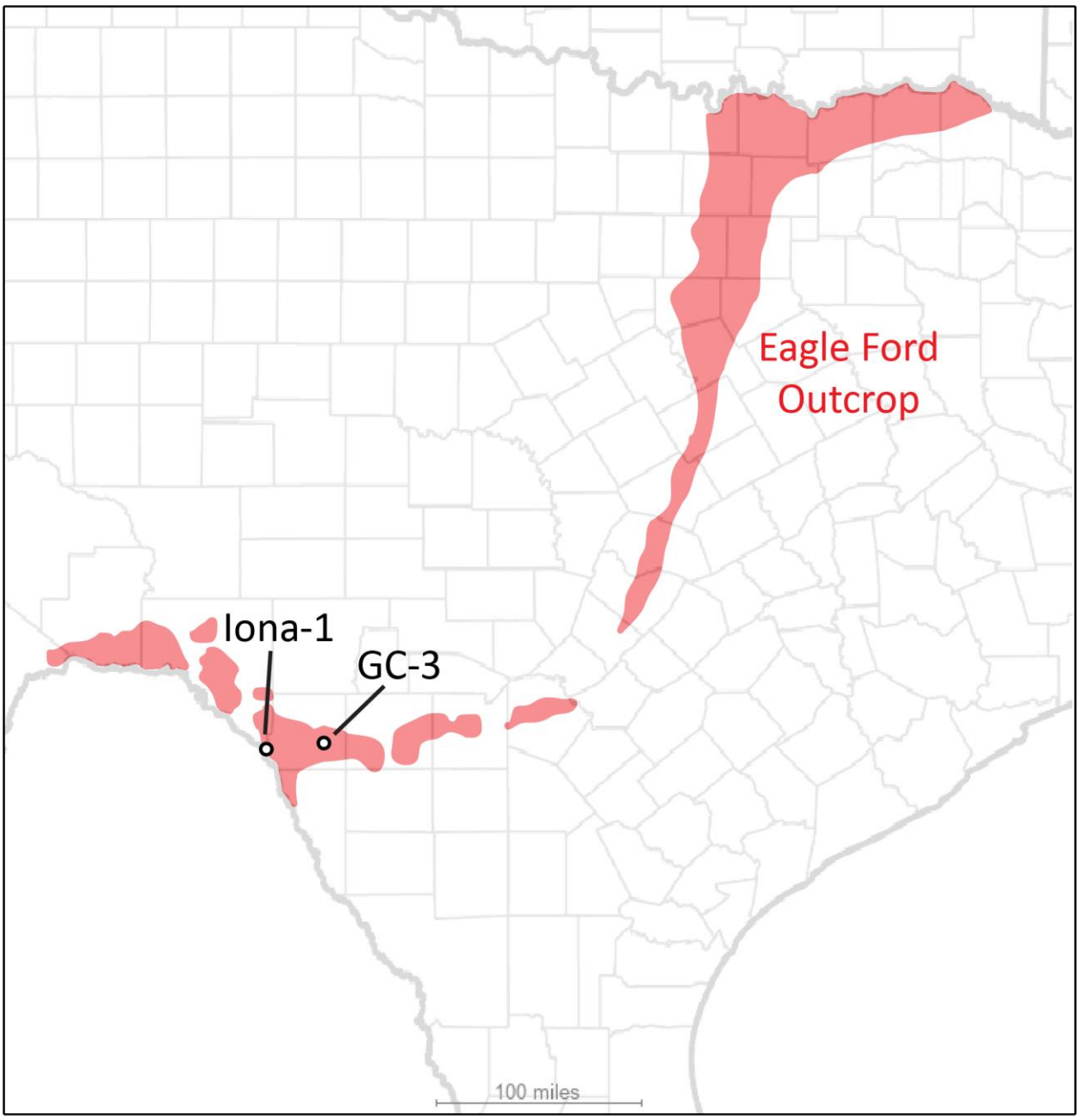
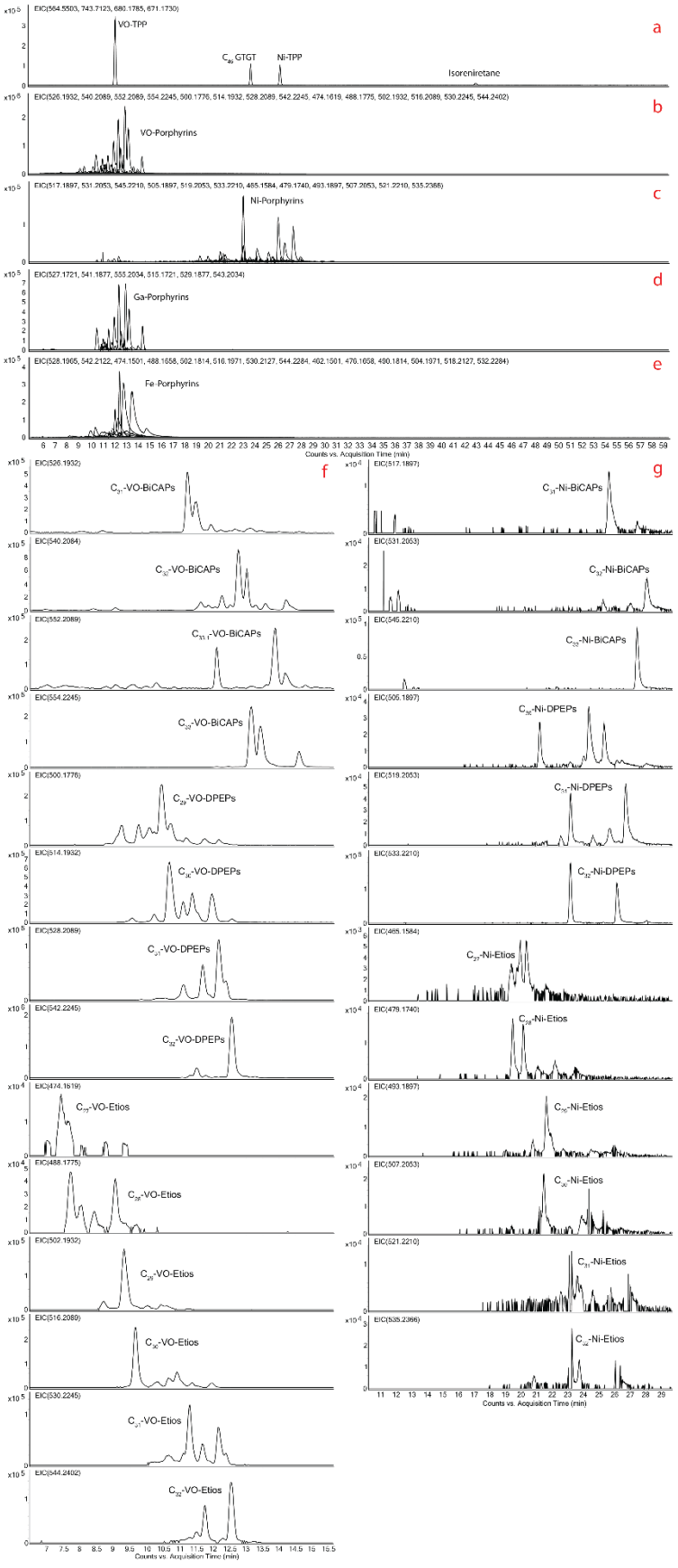


Figure 3.1 Map of Texas showing the locations for the Shell Iona-1 and USGS Gulf Coast-3 (GC-3) cores overlayed on the Eagle Ford Shale outcrop.


a
VO-TPP
C40 GTGT
Ni-TPP
Isoreniretane
b
VO-Porphyrins
c
Ni-Porphyrins
d
Ga-Porphyrins
e
Fe-Porphyrins
Counts vs. Acquisition Time (min)
f
C31-VO-BiCAPs
C32-VO-BiCAPs
C33,1-VO-BiCAPs
C32-VO-BiCAPs
C29-VO-DPEPs
C30-VO-DPEPs
C31-VO-DPEPs
C32-VO-DPEPs
C27-VO-Etios
C28-VO-Etios
C29-VO-Etios
C30-VO-Etios
C31-VO-Etios
C32-VO-Etios
Counts vs. Acquisition Time (min)
g
C31-Ni-BiCAPs
C32-Ni-BiCAPs
C33-Ni-BiCAPs
C28-Ni-DPEPs
C31-Ni-DPEPs
C32-Ni-DPEPs
C27-Ni-Etios
C28-Ni-Etios
C29-Ni-Etios
C30-Ni-Etios
C31-Ni-Etios
C32-Ni-Etios
Counts vs. Acquisition Time (min)

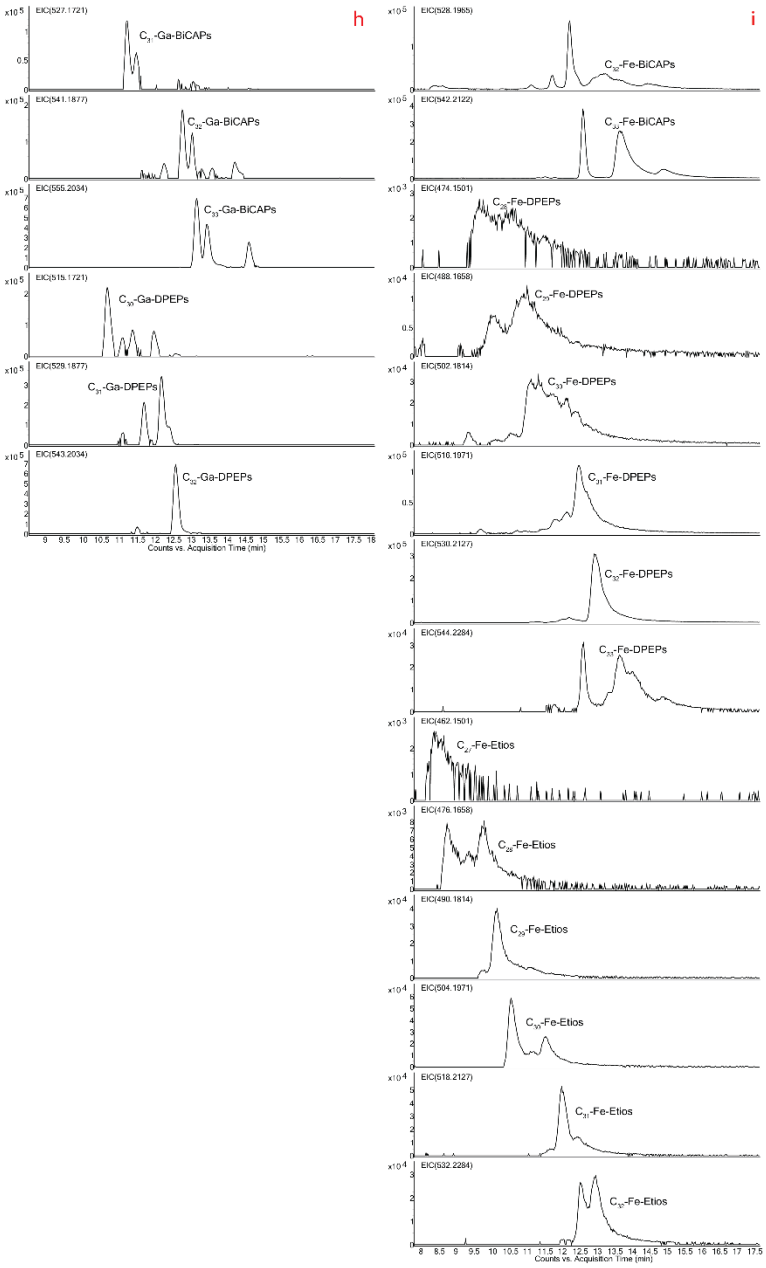


Figure 3.2 Extracted ion chromatograms (EICs) show the detection of artificial standards, isorenieratane, major VO-, Ni-, Ga- and Fe- porphyrins in the Eagle ford. The artificial standards and isorenieratane used sample EF022, VO- and Ni- porphyrins used sample EF025, Ga-porphyrins used sample EF012, and Fe-porphyrins used sample EF004. (a) Combined EICs of C_{46} GTGT, VO-TPP, Ni-TPP, and isorenieratane. (b) Combined EICs of the 14 major VO-porphyrins detected. (c) Combined EICs of the 12 major Ni-porphyrins detected. (d) Combined EICs of the 6 major Ga-porphyrins detected. (e) Combined EICs of the 14 major Fe-porphyrins detected. (f) EICs show the detection of multiple isomers of VO-porphyrins. (g) EICs show the detection of multiple isomers of Ni-porphyrin. (h) EICs show the detection of multiple isomers of Ga-porphyrins. (i) EICs show the detection of multiple isomers of Fe-porphyrin.

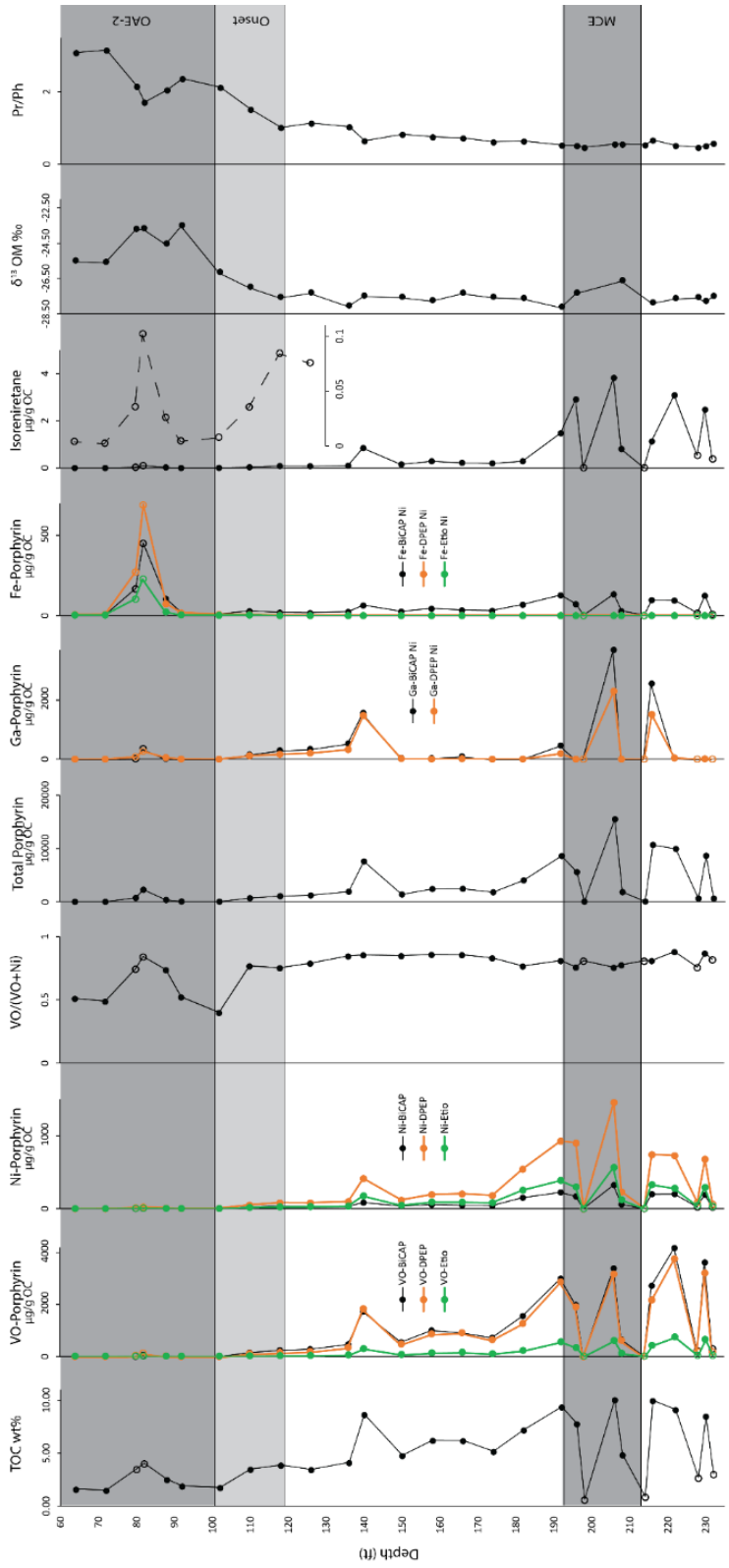


Figure 3.3 Depth profiles of Isorenieratane (with a zoom in to see OAE-2 easier), VO-porphyrin, Ni-porphyrin, Ga-porphyrin, Fe-porphyrin, the VO/(VO+Ni) ratio, and total porphyrin. TOC wt%, δ^{13} OM‰, and Pr/Ph ratios are data sourced from (French et al., 2024).

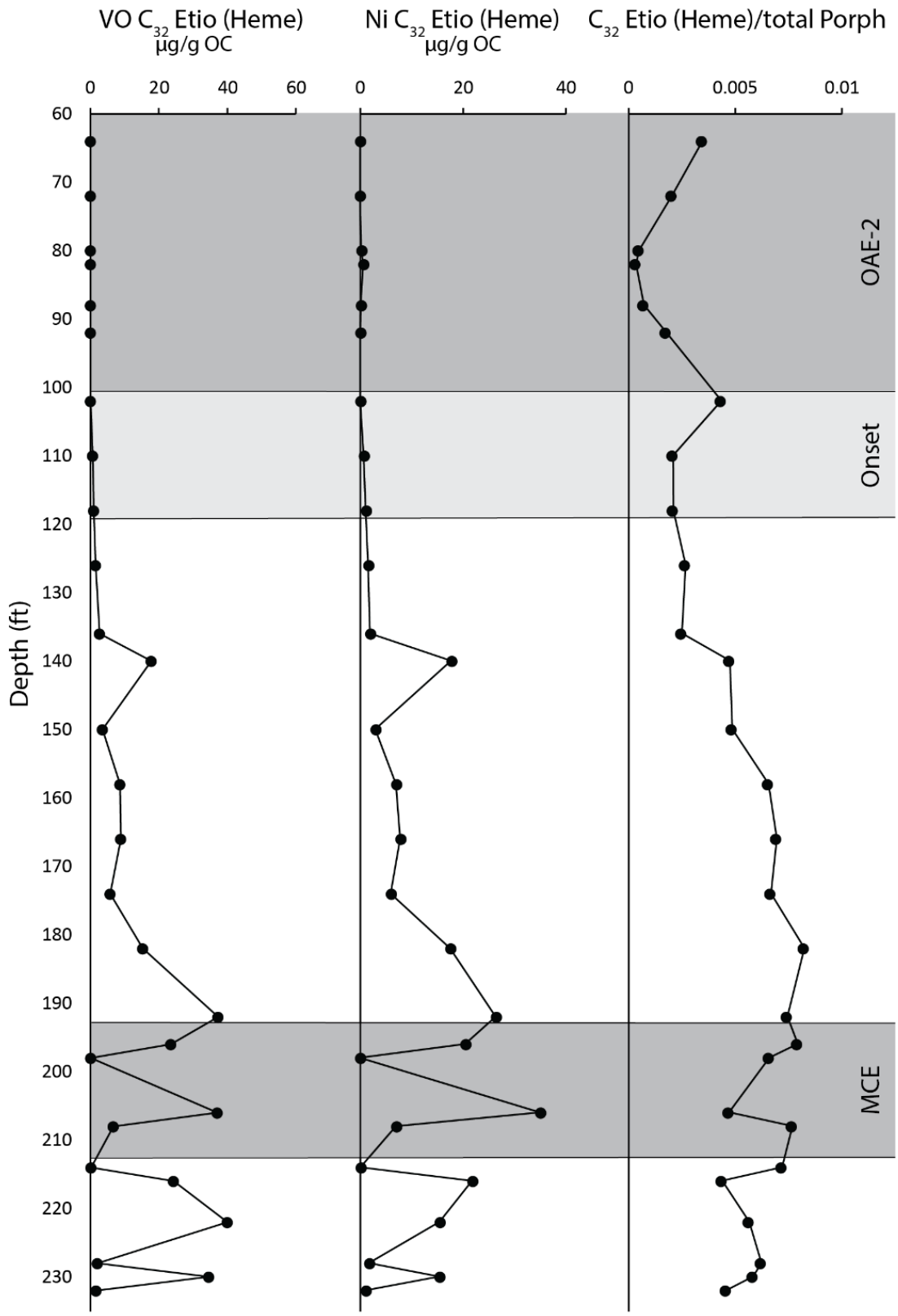


Figure 3.4 Depth profiles of C_{32}-Etio derived from the degradation of heme-*b* and the C_{32}Etio(heme)/total porphyrin ratio.

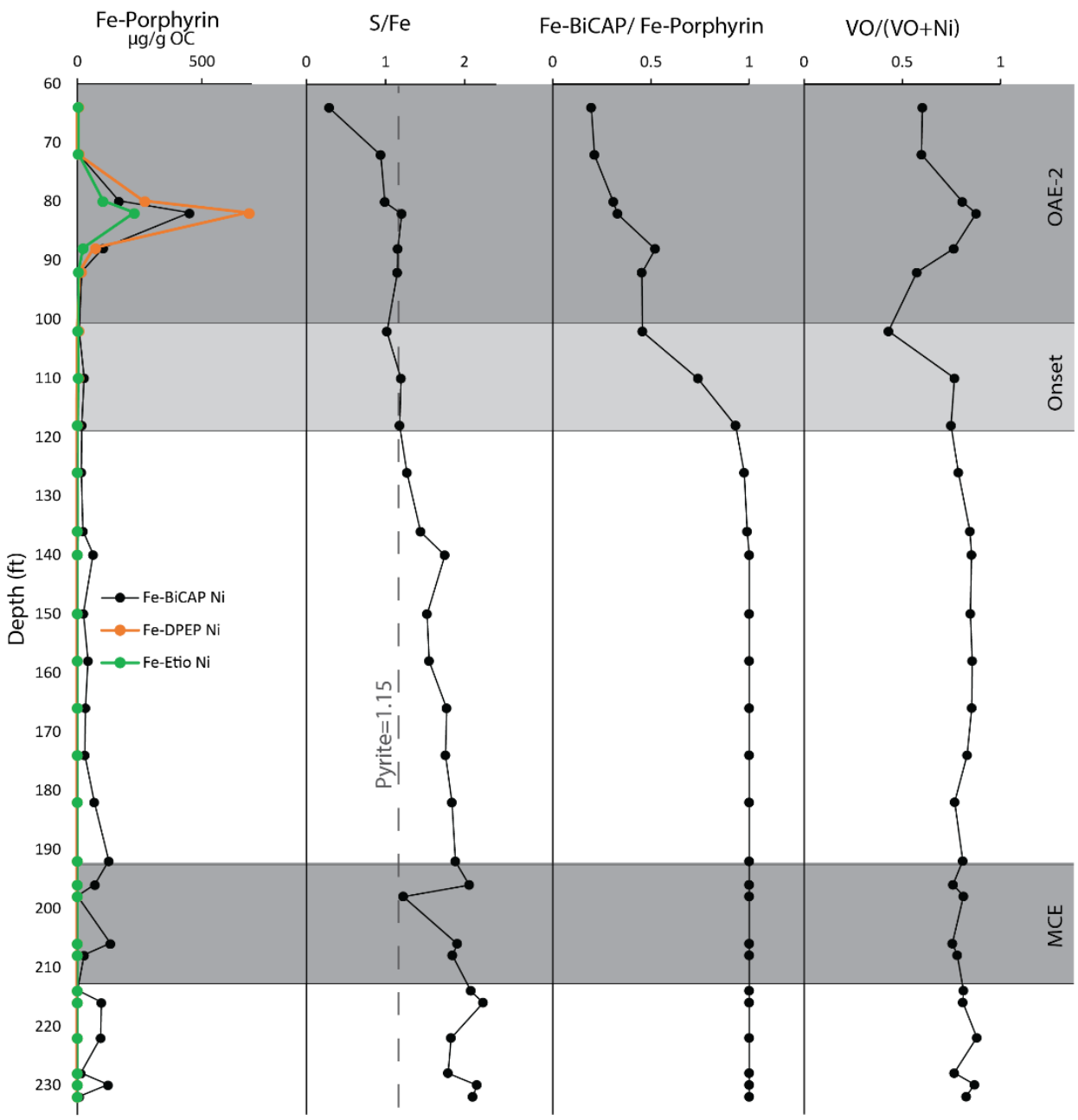


Figure 3.5 Depth profiles of Fe-porphyrin, the S/Fe ratio (French et al., 2024), the Fe-BiCAP/Fe-porphyrin ratio, and the VO/(VO+Ni) ratio. The dotted line on the S/Fe ratio represents the pyrite ratio at 1.15 where pyrite is formed.

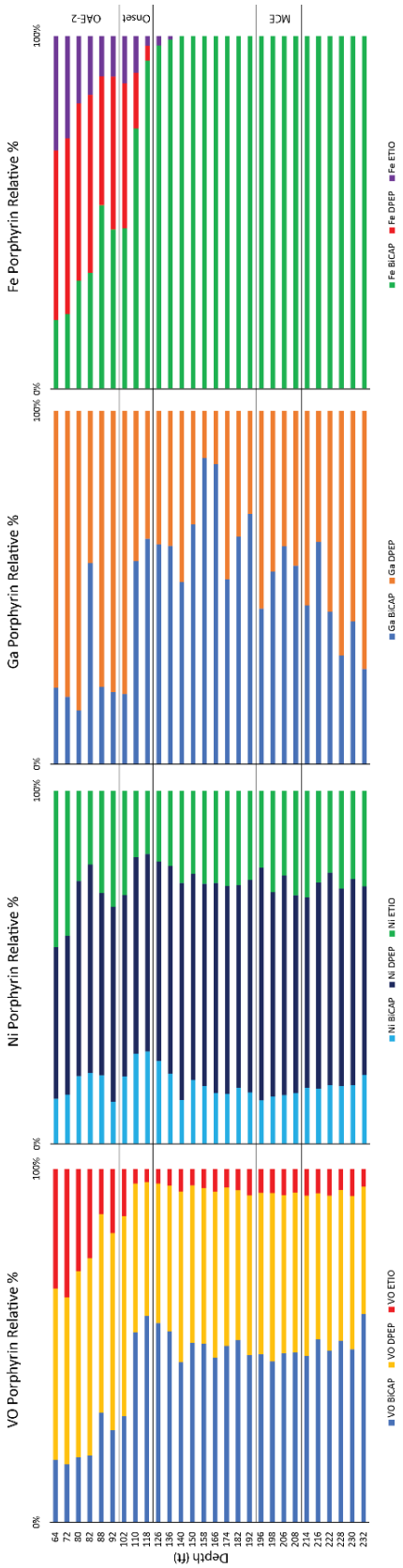


Figure 3.6 The relative abundance of BiCAP, DPEP, and Etio configurations for VO-, Ni-, Ga-, and Fe-porphyrins.

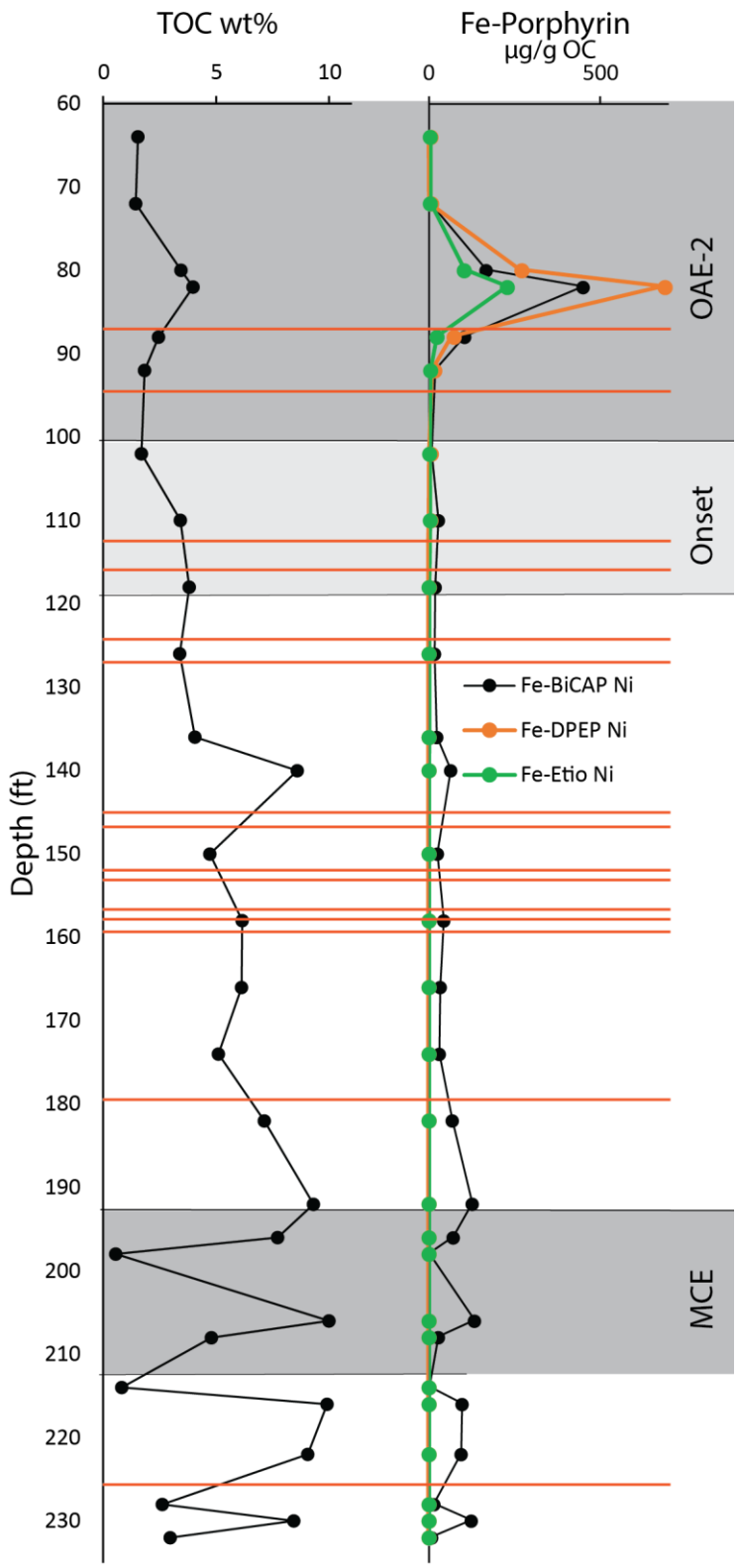


Figure 3.7 Depth profiles of the TOC wt% (French et al., 2024) and Fe-porphyrin with reported ash beds marked by orange lines.

3.7 Supplemental

Sample	Depth	Depth2	rock	TOC wt%	OC wt	Isorenieratane	VO-BiCAP	VO-DPEP	VO-Etio	VO Porph	Ni-BiCAP	Ni-DPEP	Ni-Etio	Ni Porph	Ga-BiCAP	Ga-DPEP	Ga Porph	Fe-BiCap	Fe-DPEP	Fe-Etio	Fe Porph	VO/(VO+Ni)
	(ft)	(m)	(g)		(g)	(ng/g OC)	(ng/g OC)	(ng/g OC)	(ng/g OC)	(ng/g OC)	(ng/g OC)	(ng/g OC)	(ng/g OC)	(ng/g OC)	(ng/g OC)	(ng/g OC)	(ng/g OC)	(ng/g OC)	(ng/g OC)	(ng/g OC)	(ng/g OC)	
EF001	64	19.5	0.1261	1.54	0.0819	4.18	308.15	845.24	588.83	1742.23	151.54	507.27	496.05	1154.86	313.41	1136.11	1449.52	2488.79	6146.68	4135.14	12770.62	0.6014
EF002	72	21.9	0.1059	1.45	0.0730	2.49	309.48	895.55	687.53	1892.56	185.18	592.18	501.19	1278.55	339.91	1446.48	1786.39	3207.12	7535.85	4382.68	15125.65	0.5968
EF003	80	24.4	0.1184	3.45	0.0343	35.79	15485.68	44526.85	24446.19	84458.72	4016.83	11537.02	4959.60	20513.44	14399.71	80742.66	95142.37	166756.21	271518.18	103397.65	541672.04	0.8046
EF004	82	25	0.1151	3.98	0.0289	102.22	46559.79	137224.75	62133.56	245918.10	7145.42	21082.79	7011.72	35239.93	351715.07	266506.24	618221.30	449930.67	689621.74	228464.40	1368016.81	0.8747
EF005	88	26.8	0.1098	2.46	0.0446	26.02	16922.08	30683.47	6940.60	54546.16	3372.17	8945.59	4793.97	17111.73	14503.63	52142.47	66646.10	104299.65	73014.00	22905.86	200219.51	0.7612
EF006	92	28	0.1108	1.84	0.0602	4.68	1861.50	3989.17	1297.96	7148.62	654.36	3016.40	1650.13	5320.89	2012.77	7834.49	9847.26	17519.38	16771.54	4457.34	38748.27	0.5733
EF007	102	31.1	0.1110	1.7	0.0653	7.89	1818.13	3424.58	804.82	6047.53	1563.70	4175.11	2308.64	8047.45	896.40	3631.88	4528.28	7717.62	6936.09	2279.43	16933.15	0.4291
EF008	110	33.5	0.1020	3.42	0.0298	35.46	156896.65	123153.12	11938.92	291988.68	23202.84	50326.18	16565.66	90094.68	154640.93	114279.23	268920.16	27130.73	5791.18	3820.63	36742.55	0.7642
EF009	118	36	0.1198	3.81	0.0314	84.40	247927.64	161200.23	15408.70	424536.57	37583.65	80287.59	25370.73	143241.97	297144.26	168711.29	465855.55	17857.12	824.26	522.51	19203.89	0.7477
EF010	126	38.4	0.1073	3.4	0.0316	75.73	288308.68	202110.67	20956.42	511375.77	33103.93	79811.21	27427.60	140342.75	340053.37	206126.02	546179.39	15644.28	0.00	425.76	16070.04	0.7847
EF011	136	41.5	0.1087	4.07	0.0267	96.39	468473.99	356811.35	40588.81	865874.15	32376.46	95365.04	33433.79	161175.29	526976.25	325688.80	852665.05	22603.88	0.00	253.56	22857.43	0.8431
EF012	140	42.7	0.1040	8.59	0.0121	841.98	1721989.87	1840687.85	240709.98	3803387.70	83728.31	412750.76	166420.92	662899.98	1565538.50	1474554.64	3040093.14	62936.60	0.00	0.00	62936.60	0.8516
EF013	150	45.7	0.1140	4.72	0.0242	154.06	551830.52	484944.38	49892.36	1086667.25	36189.24	117219.62	45278.74	198687.60	41057.27	19396.59	60453.85	24386.91	0.00	0.00	24386.91	0.8454
EF014	158	48.2	0.1120	6.15	0.0182	284.01	1002349.25	873621.54	105964.42	1981935.20	55414.16	193499.82	85229.24	334143.21	38587.79	5900.49	44488.27	43160.56	0.00	0.00	43160.56	0.8557
EF015	166	50.6	0.1218	6.12	0.0199	222.65	909788.35	918853.23	124446.71	1953088.28	49012.84	202120.70	85010.59	336144.12	97290.61	17162.74	114453.36	32457.77	0.00	0.00	32457.77	0.8532
EF016	174	53	0.1080	5.1	0.0212	197.25	725742.36	652043.43	76064.80	1453850.59	43096.74	179542.75	77383.26	300022.75	3672.28	3346.51	7023.79	29718.71	0.00	0.00	29718.71	0.8289
EF017	182	55.5	0.1135	7.14	0.0159	287.06	1553189.85	1275473.52	180407.24	3009070.61	150356.29	541572.79	228539.72	920468.80	6915.85	3829.26	10745.11	68047.37	0.00	0.00	68047.37	0.7658
EF018	192	58.5	0.1216	9.31	0.0131	1474.15	2993216.16	2863377.00	473546.80	6330139.95	223366.49	925014.86	361782.27	1510163.62	463726.90	190509.53	654236.43	126120.64	0.00	0.00	126120.64	0.8074
EF019	196	59.7	0.1179	7.73	0.0153	2910.71	1982328.93	1908916.53	280970.41	4172215.87	168520.44	899815.56	269084.93	1337420.93	2365.96	3011.86	5377.82	70507.31	0.00	0.00	70507.31	0.7573
EF020	198	60.4	0.1021	0.56	0.1823	13.66	9385.56	9831.57	1398.60	20615.72	676.79	2927.20	1228.72	4832.71	140.60	117.44	258.04	687.99	0.00	0.00	687.99	0.8101
EF021	206	62.8	0.1108	10	0.0111	3820.20	3384521.66	3166258.73	520716.91	7071497.30	323686.67	1453762.89	522285.13	2299734.69	3694691.05	2297038.11	5991729.16	132593.76	0.00	0.00	132593.76	0.7546
EF022	208	63.4	0.1063	4.8	0.0221	805.74	663958.80	626542.00	91514.61	1382015.41	59222.27	231035.96	102086.74	392344.97	1669.89	1304.38	2974.27	27065.86	0.00	0.00	27065.86	0.7789
EF023	214	65.2	0.1064	0.83	0.1282	14.19	19680.83	18938.25	3142.15	41761.23	1626.83	5496.47	2627.78	9751.07	213.83	261.77	475.60	1131.00	0.00	0.00	1131.00	0.8107
EF024	216	65.8	0.1270	9.91	0.0128	1130.05	2715464.73	2170502.02	357467.57	5243434.31	199314.77	740487.72	311382.05	1251184.54	2554744.52	1509485.97	4064230.49	96641.97	0.00	0.00	96641.97	0.8074
EF025	222	67.7	0.1103	9.05	0.0122	3086.09	4161622.27	3756361.12	642776.56	8560759.95	201395.25	726830.82	251631.94	1179858.01	33373.61	43926.01	77299.61	93918.82	0.00	0.00	93918.82	0.8789
EF026	228	69.5	0.1200	2.62	0.0458	534.84	237751.71	197333.70	27454.97	462540.38	24811.06	84964.31	33631.41	143406.78	210.57	475.94	686.51	14339.05	0.00	0.00	14339.05	0.7633
EF027	230	70.1	0.1035	8.44	0.0123	2473.01	3609275.56	3205667.11	560309.59	7375252.26	192383.45	677201.27	263028.16	1132612.88	6006.19	8845.82	14852.01	122881.24	0.00	0.00	122881.24	0.8669
EF028	232	70.7	0.1189	2.98	0.0399	385.90	299381.28	183342.52	25489.77	508213.57	22398.12	61428.13	24113.56	107939.81	203.93	554.20	758.13	7318.68	0.00	0.00	7318.68	0.8248

Supplementary 3.1 The raw data of depth profiles presented in Figure 3.3

Chapter 4 Integrative Discussion of Selective Bias Observed in Metalloporphyrin Chelation

Authors: Derek Parks[1*], Xiao-Lei Liu[1]

Affiliations: [1]School of Geosciences, University of Oklahoma, Norman, Oklahoma 73019, USA.

Abstract: Metalloporphyrins, particularly vanadyl (VO) and nickel (Ni) complexes, are widely applied as redox-sensitive proxies using the VO/(VO+Ni) ratio, yet this proxy implicitly assumes uniform metal access and non-selective chelation across porphyrin classes. Earlier works have show this assumption to be invalid, with VO and Ni exhibiting distinct, structure-dependent chelation preferences among bicycloalkanoporphyrins (BiCAP), deoxophylloerythroetioporphyrins (DPEP), and etioporphyrins (Etio), introducing a possible bias to metalloporphyrin-based paleoredox interpretations. Here, we integrate datasets from the Woodford Shale, Demerara Rise, and Eagle Ford Shale to test the persistence, variability, and mechanistic causes of the bias across contrasting ages, redox conditions, and metal-ion regimes. All three shale members exhibit a consistent tendency for VO to preferentially chelation BiCAP and Ni to preferentially chelate Etio, with DPEP showing limited selectivity. Statistical analyses show strong correlations between VO/Ni and BiCAP/Etio ratios (R^2 up to 0.75; correlation coefficients up to 0.86), confirming the systematic nature of this selectivity, though this correlation diminishes under metal-limited conditions such as during OAE-2 and with metal competition from gallium (Ga) and iron (Fe). A mechanistic interpretation attributes this selectivity to differences in coordination geometry and macrocycle rigidity: Ni^{2+} favors a square-planar complex which is compatible with the flexible Etio macrocycle, whereas VO^{2+} forms square-pyramidal complexes that align with the structurally constrained BiCAP macrocycle. These findings demonstrate that metalloporphyrin distributions encode a coupled signal of redox state, metal availability, and porphyrin class concentrations. Future work combining expanded shale datasets and molecular imaging (NMR, X-ray crystallography) will be critical to directly visualize coordination geometries and confirm the proposed structural basis for selective metalation, as well as refining models for sedimentary metalloporphyrin signatures in paleoenvironmental reconstructions.

4.1 Introduction

All three previous chapters delve into the relationship among metalloporphyrins, specifically vanadyl (VO) and nickel (Ni) porphyrins. These two metalloporphyrins have long served as geochemical proxies for redox conditions, using the VO/(VO+Ni) ratio. High ratios (>0.50) and elevated sulfur content (>1wt%) indicate anoxic or euxinic depositional environments resulting from Ni^{2+} precipitation as nickel sulfide, which in turn favors VO^{2+} complexation (Lewan and Maynard, 1982; Lewan, 1984; Huseby et al., 1996). Conversely, lower

ratios (<0.50) are interpreted as oxic, allowing Ni^{2+} to compete for chelation and thereby increasing Ni-porphyrin abundance due to its higher equilibrium constant (Moldowan et al., 1985; Chen and Philp, 1991).

While these explanations have proven useful and broadly accepted across the literature, recent analysis of the Woodford Shale revealed a more nuanced chelation bias among the detected porphyrin classes: bicycloalkanoporphyrins (BiCAP), deoxophylloerythroethioporphyrin (DPEP), and etioporphyrin (Etio). This observed bias calls into question the adequacy of the VO/Ni chelation explanation, as each class of porphyrin originates from distinct biosynthetic and diagenetic mechanisms, which may confound proxy interpretations. Specifically, it was determined that VO- preferentially chelates to BiCAP with only minor chelation to Etio, and Ni- preferentially chelates to Etio, again with minimal interaction with BiCAP. The detection of such chelation bias implies that the conventional ratio may be skewed in settings where certain porphyrin production pathways dominate.

Upon observing this bias in the Woodford Shale (Parks and Liu, 2023), we extended our investigation to include additional black shales, aiming to determine whether the phenomenon was consistent or an outlier. The Woodford Shale, from the Late Devonian-Early Mississippian (Comer, 1991), is notably ancient. In contrast, the Demerara Rise was selected as a representative of shales deposited during OAE-2 (mid-Cretaceous-mid-Paleogene), while the Eagle Ford Shale, also from OAE-2 but with records of oxic conditions during this event, provides a compelling counterexample to prevailing global trends in ocean redox. Notably, chelation bias was observed in both the Demerara Rise and Eagle Ford, albeit with less intensity than in the Woodford Shale, indicating that the phenomenon is pervasive rather than anomalous,

confirming previous observations of the bias as well (Sundararaman and Boreham, 1993; Qian et al., 2010)

4.2 Conceptual Integration

The chelation bias manifested consistently across all shale members examined, the Woodford Shale, Demerara Rise, and Eagle Ford. Each demonstrated a distinct proclivity for VO chelation to BiCAP and Ni chelation to Etio. In the Woodford Shale relative percentages strongly favor VO-BiCAP and Ni-Etio, with both VO- and Ni-DPEP not displaying pronounced preferences (Figure 4.1A). The Demerara Rise continues to show robust VO-BiCAP selectivity, and a relative decrease in VO-DPEP compared to the Woodford. Unlike in the Woodford, the Demerara Rise exhibits a less distinct Ni-Etio bias, though Ni-Etio remains favored compared to VO-Etio (Figure 4.1B). The Eagle Ford's chelation distribution reflects dominance of VO-BiCAP and similar ratios for the DPEP class as observed in the Woodford, but also displays a rise in VO-Etio in response to prevailing oxic conditions during OAE-2. The Ni-Etio prominence in the Eagle Ford is less than in the Woodford, yet exceeds that in the Demerara Rise (Figure 4.1C).

To further address the chelation bias, correlation analysis comparing the VO/Ni ratio and BiCAP/Etio ratio were performed. The Woodford Shale demonstrates a robust positive correlation ($R^2 = 0.75$), with a regression slope of 1.28 (Figure 4.2A). The Demerara Rise, while retaining a significant positive correlation, shows a lower $R^2 = 0.54$ and a slope of 0.21 (Figure 4.2B). The Eagle Ford exhibits only a weakly positive correlation ($R^2 = 0.19$, slope of 0.35, Figure 4.2C), suggestive of additional factors influencing chelation patterns. Notably, the Demerara Rise contains an additional metalloporphyrin iron (Fe), reported in (Connock et al., 2022), along

with free base (FB) porphyrins, while the Eagle Ford contains both iron (Fe) and gallium (Ga) that compete for chelation.

The re-examination of the Eagle Ford data, with samples dominated by Fe or Ga porphyrins removed EF001 (64ft)-EF012 (140ft), EF021 (206ft), and EF024 (206ft) based off of Figure 4.3, yields an improved cross-plot (R^2 = 0.24, slope 0.70, Figure 4.2D), though the correlation remains comparatively low.

To more thoroughly examine the relationship between the VO/Ni and BiCAP/Etio ratios, the correlation coefficient was calculated as described in Equation 1 below. Analogous to the R^2 statistic, the correlation coefficient exhibits greater strength as its value approaches +1 or -1, while values closer to 0 indicate weaker relationships. For the Woodford Shale, the resulting correlation coefficient was 0.86, thereby affirming a strong association between these variables. In the Demerara Rise, the calculated correlation coefficient was 0.74, which similarly reflects a strong correlation. By comparison, the Eagle Ford produced a correlation value of 0.43, which, while lower, still suggests a meaningful relationship. When all data from the Woodford Shale, Demerara Rise, and Eagle Ford are aggregated, the overall correlation coefficient is calculated to be 0.68, corroborating the presence of a robust correlation across all sample sets considered.

Equation 4.1:

$$Correl(X,Y) = \frac{\sum(x-\bar{x})\,(y-\bar{y})}{\sqrt{\sum(x-\bar{x})^2 \sum(y-\bar{y})^2}} \quad \bar{x}\ and\ \bar{y}\ are\ averages$$

While Ni and VO are generally favored in chelation over to Ga or Fe, available thermodynamic data on the formation of VO-, Ni-, or Ga- porphyrin complexes remain limited,

especially regarding the influence of varying porphyrin substrates on the overall formation energy. Thus, some inferential reasoning is required to interpret these results. Broadly, Ni and VO are the most preferred metals for chelation, with Fe and Ga following in respective favorability (Coutsolelos et al., 1986; Pleyer et al., 2022; Farooq et al., 2023). Although all these metals demonstrate thermodynamic favorability, inevitable competition among them for complexation with available porphyrins reduces the observed correlation strength in systems that are not VO and Ni dominated. Furthermore, global declines in oceanic metal ion concentrations during OAE-2 (Owens et al., 2016) likely restricted the breadth of metalloporphyrin production, providing further context for reduced correlation values during these intervals.

Importantly, the Woodford Shale is characterized exclusively by VO and Ni porphyrins and its deposition corresponded to intervals with relatively stable concentrations of globally available metal ions, thus providing a clear record of chelation bias. By contrast, both the Demerara Rise and Eagle Ford were deposited during intervals of reduced oceanic metal ion availability, factors that collectively contribute to diminished correlation coefficients observed in these settings.

4.3 Mechanistic and Structural Implications

The observed chelation bias necessitates a mechanistic explanation. In this study, a structural mechanism is proposed to account for the selective chelation exhibited by the various porphyrin classes and their corresponding metals. This selectivity stems from the fundamental difference in the coordination chemistry of Ni^{2+} and VO^{2+}, leading each metal to form distinct

coordination geometries upon binding to porphyrin ligands. Nickel(II) preferentially adopts a square-planar configuration, situating the nickel atom within the plane defined by the four nitrogen atoms of the porphyrin macrocycle (Figure 4.4; Kim et al., 1996). In contrast, vanadyl (VO^{2+}) assumes a five-coordinate square-pyramidal geometry, wherein the vanadium atom resides above the porphyrin plane, with the oxygen occupying an axial position (Figure 4.4; Drew et al., 1984).

This difference in coordination geometry has significant implications for chelation selectivity. The etioporphyrin (Etio), lacking the E and F rings present in the BiCAP structure (Figure 4.5), is more conformationally flexible, allowing the macrocycle to pucker and accommodate the bond angles and lengths required for the square-planar coordination preferred by nickel. Conversely, the more rigid BiCAP macrocycle, by virtue of its structural constraints, is more adverse to undergoing such conformational adjustment, making it less amenable to nickel chelation and more likely to favor vanadyl chelation, which occurs above the plane of the macrocycle and is comparatively less sensitive to bond length and angle precision.

A comparable structural explanation may be invoked for the gallium porphyrins detected in the Eagle Ford. Gallium commonly exhibits a six-coordinate octahedral arrangement (de la Fuente et al., 2023; Pantović et al., 2024). However, in the presence of rigid porphyrin scaffolds, gallium can assume a square-pyramidal geometry (Price et al., 2020; de la Fuente et al., 2023)

Similar to vanadyl, which explains its exclusive detection in BiCAP and DPEP complexes, with no observed gallium chelation to the more flexible Etio structure.

4.4 Outlook and Future Directions

Future research exploring this discovery could proceed along several avenues. Primarily, additional analyses on other black shale formations are recommended to further validated the observed chelation bias. As was previously discussed, the Woodford Shale exhibits the most distinct chelation selectivity and the strongest correlation between the VO/Ni and BiCAP/DPEP ratios; the Demerara Rise displays a moderate correlation; and the Eagle Ford shows a relatively low R^2 value but a correspondingly improved calculated correlation coefficient, consistent with the relative abundances depicted in Figure 4.1. The aggregated dataset reveals a high overall correlation, underscoring the statistical significance of this relationship. The acquisition of more extensive datasets is crucial for bolstering the robustness of these conclusions. Thus, incorporating a broader range of shale members would enable the construction of a comprehensive catalog amenable to rigorous statical examination across diverse depositional environments and geographical locations.

A secondary, yet more technically challenging, direction for future inquiry involves molecular imaging of metalloporphyrins. Such imaging would offer direct structural evidence to either support or refute the hypothesis that the observed chelation bias stems from intrinsic differences in molecular geometry. Two methodologies present themselves as viable candidates. The first, Nuclear Magnetic Resonance (NMR) spectroscopy (Coutsolelos et al., 1986; de la Fuente et al., 2023), though less frequently applied to metalloporphyrins, excels in

elucidating organic molecular structures and could thus provide valuable insight into porphyrin conformations. The second, and arguably superior, technique for resolving metal coordination geometries is X-ray crystallography, which has a more established history in metalloporphyrin structure determination (Drew et al., 1984; Kim et al., 1996; Pantović et al., 2024). X-ray crystallography offers the distinct advantage of immobilizing the molecular structure within a crystalline lattice, thereby preventing conformational fluctuations during analysis. Nevertheless, X-ray crystallography carries inherent drawbacks, chief among them are the difficulties associated with crystal growth, including the substantial time investment and the necessity of ample sample material, which exceeds that required for NMR. Despite these challenges, X-ray crystallography remains the preferred method for detailed structural characterization.

Initial efforts might focus on synthetic porphyrin complexes chelated to vanadyl and nickel to conclusively establish coordination geometries. Such artificial metalloporphyrins are commercially accessible, facilitating the development of standardized crystal growth protocols. Following successful imaging of synthetic complexes, compound-specific imaging of natural metalloporphyrins could be pursued. Given the substantial sample volumes that would be required, core samples may be inadequate. Thus, freshly exposed outcrops, where larger quantities of material can be obtained, likely represent the most promising sources. Upon isolation and crystallization of sufficient quantities of geoporphyrins, X-ray crystallographic analysis could proceed. Alternatively, if sample availability restricts crystallographic studies, NMR spectroscopy stands as a feasible approach to structural elucidation. Ultimately, direct imaging of metalloporphyrin structures would yield compelling evidence to either confirm or

negate the hypothesis that chelation selectivity of vanadyl for BiCAP and nickel for Etio is dictated by differences in structural conformation by revealing bond angles and lengths in situ.

4.5 Summary

In summary, this chapter presents integrative evidence demonstrating that selective chelation of vanadyl (VO) and nickel (Ni) to bicycloalkanoporphyrins (BiCAP) and etioporphyrins (Etio), respectively, constitutes a pervasive and mechanistically meaningful phenomenon within black shale geochemistry. This selective bias challenges conventional interpretations of metalloporphyrin-based redox proxies that rely on ratios of VO and Ni, as these proxies can be skewed by differential production pathways, preservation dynamics, and structural diversity of porphyrin classes across various depositional environments.

The research shows that the chelation bias is consistently observed across diverse formations, including the Woodford Shale, the Demerara Rise, and the Eagle ford, despite differences in age, depositional redox conditions, and metal availability. Statistically significant correlations between VO/Ni and BiCAP/Etio ratios, though variable in strength due to competing metalloporphyrins (such as iron and gallium complexes) and global shifts in marine metal ion concentrations during OAE-2, support the hypothesis that chelation selectivity is a fundamental and reproducible geochemical process rather an anomalous occurrence.

Mechanistically, the selectivity is attributed to intrinsic difference in the coordination geometry of Ni^{2+} and VO^{2+}. Nickel adopts a square-planar geometry necessitating the structural flexibility of Etio for proper coordination, whereas vanadyl's square-pyramidal configurations aligns effectively with the more rigid BiCAP structure. Similar geometric constraints explain the

distribution of gallium porphyrins, which preferentially chelate BiCAP and DPEP but not Etio. This conceptual framework hinges on molecular geometry that govern metal-porphyrin complex formation, offering a refined understanding of metal complexation in sedimentary organic matter.

Looking forward, future studies should extend empirical investigations to a broader suite of black shale members for statistical validation across different stratigraphic and geographic contexts. Molecular imaging techniques such as Nuclear Magnetic Resonance (NMR) and X-ray crystallography hold promise for direct visualization of metalloporphyrin structures and coordination geometries, providing definitive evidence to confirm or refute the structural basis of the observed chelation bias. Work with synthetic metalloporphyrins complexes may provide a controlled means for methological development and proof of concept prior to imaging natural samples, which require large quantities of sediment due to low porphyrin concentrations.

Collectively, this integrative approach not only advances paleoenvironmental reconstructions based on metalloporphyrin proxies but also deepens our grasp of the interplay between biological production, geochemical processes, and molecular structure in natural organic matter diagenesis. If the mechanistic hypothesis is corroborated through forthcoming imaging and expanded geochemical datasets, it could lead to the development of refined models for interpreting sedimentary metalloporphyrin signatures in ancient depositional environments.

4.6 References

Chen, J.H., Philp, R.P., 1991. Porphyrin distributions in crude oils from the Jianghan and Biyang basins, China. Chemical Geology, Trace Metals in Petroleum Geochemistry 91, 139–151.

Comer, J., 1991. Stratigraphic Analysis of the Upper Devonian Woodford Formation, Permian Basin, West Texas and Southeastern New Mexico, Report Investigation. University of Texas at Austin, Bureau of Economic Geology. doi:10.23867/RI0201D

Connock, G.T., Owens, J.D., Liu, X.-L., 2022. Biotic induction and microbial ecological dynamics of Oceanic Anoxic Event 2. Communications Earth & Environment 3, 1–10.

Coutsolelos, A., Guilard, R., Bayeul, D., Lecomte, C., 1986. Gallium(III) porphyrins: synthesis and physicochemical characteristics of halogeno gallium(III) porphyrins—X-ray crystal structure of chloro-(5,10,15,20-tetraphenylporphyrinato) gallium(III). Polyhedron 5, 1157–1164.

de la Fuente, M.C., Ageitos, L., Lages, M.A., Martínez-Matamoros, D., Forero, A.M., Balado, M., Lemos, M.L., Rodríguez, J., Jiménez, C., 2023. Structural Requirements for Ga3+ Coordination in Synthetic Analogues of the Siderophore Piscibactin Deduced by Chemical Synthesis and Density Functional Theory Calculations. Inorganic Chemistry 62, 7503–7514.

Drew, M.G.B., Mitchell, P.C.H., Scott, C.E., 1984. Crystal and molecular structure of three oxovanadium(IV) porphyrins: oxovanadium tetraphenylporphyrin(I), oxovanadium(IV) etioporphyrin(II) and the 1:2 adduct of (II) with 1,4-dihydroxybenzene(III). Hydrogen bonding involving the VO group. Relevance to catalytic demetallisation. Inorganica Chimica Acta 82, 63–68.

Farooq, M.T., Jiarasuksakun, T., Kaemawichanurat, P., 2023. Entropy analysis of nickel(II) porphyrins network via curve fitting techniques. Scientific Reports 13, 17317.

Huseby, B., Barth, T., Ocampo, R., 1996. Porphyrins in Upper Jurassic source rocks and correlations with other source rock descriptors. Organic Geochemistry, Organic Geochemistry 25, 273–294.

Kim, J.S., Reibenspies, J.H., Darensbourg, M.Y., 1996. Characteristics of Nickel(0), Nickel(I), and Nickel(II) in Phosphino Thioether Complexes: Molecular Structure and S-Dealkylation of (Ph2P(o-C6H4)SCH3)2Ni0. Journal of the American Chemical Society 118, 4115–4123.

Lewan, M.D., 1984. Factors controlling the proportionality of vanadium to nickel in crude oils. Geochimica et Cosmochimica Acta 48, 2231–2238.

Lewan, M.D., Maynard, J.B., 1982. Factors controlling enrichment of vanadium and nickel in the bitumen of organic sedimentary rocks. Geochimica et Cosmochimica Acta 46, 2547–2560.

Moldowan, J.M., Seifert, W.K., Gallegos, E.J., 1985. Relationship Between Petroleum Composition and Depositional Environment of Petroleum Source Rocks1. AAPG Bulletin 69, 1255–1268.

Munoz, G., K. Gunessee, B., Bégué, D., Bouyssiere, B., Baraille, I., Vallverdu, G., Silva, H.S., 2019. Redox activity of nickel and vanadium porphyrins: a possible mechanism behind petroleum genesis and maturation? RSC Advances 9, 9509–9516.

Owens, J.D., Reinhard, C.T., Rohrssen, M., Love, G.D., Lyons, T.W., 2016. Empirical links between trace metal cycling and marine microbial ecology during a large perturbation to Earth's carbon cycle. Earth and Planetary Science Letters 449, 407–417.

Pantović, B.V., Ašanin, D.P., Perdih, F., Radanović, D.D., Turel, I., Djuran, M.I., Glišić, B.Đ., 2024. Gallium(III) complexes with 1,3-pdta-type of ligands: The influence of an alkyl substituent in 1,3-propanediamine chain and the metal counter cation on the structural properties of the complex. Polyhedron 258, 117045.

Parks, D.R., Liu, X.-L., 2023. Distributions of vanadyl and nickel porphyrins in the Woodford Shale and selective chelation of metal species by different tetrapyrrole configurations. Organic Geochemistry 186, 104693.

Pleyer, H.L., Moeller, R., Fujimori, A., Fox, S., Strasdeit, H., 2022. Chemical, Thermal, and Radiation Resistance of an Iron Porphyrin: A Model Study of Biosignature Stability. Astrobiology 22, 776–799.

Price, T.W., Yap, S.Y., Gillet, R., Savoie, H., Charbonnière, L.J., Boyle, R.W., Nonat, A.M., Stasiuk, G.J., 2020. Evaluation of a Bispidine-Based Chelator for Gallium-68 and of the Porphyrin Conjugate as PET/PDT Theranostic Agent. Chemistry (Weinheim an Der Bergstrasse, Germany) 26, 7602–7608.

Qian, K., Edwards, K.E., Mennito, A.S., Walters, C.C., Kushnerick, J.D., 2010. Enrichment, Resolution, and Identification of Nickel Porphyrins in Petroleum Asphaltene by Cyclograph Separation and Atmospheric Pressure Photoionization Fourier Transform Ion Cyclotron Resonance Mass Spectrometry. Analytical Chemistry 82, 413–419.

Sundararaman, P., Boreham, C.J., 1993. Comparison of nickel and vanadyl porphyrin distributions of sediments. Geochimica et Cosmochimica Acta 57, 1367–1377.

4.7 Figures

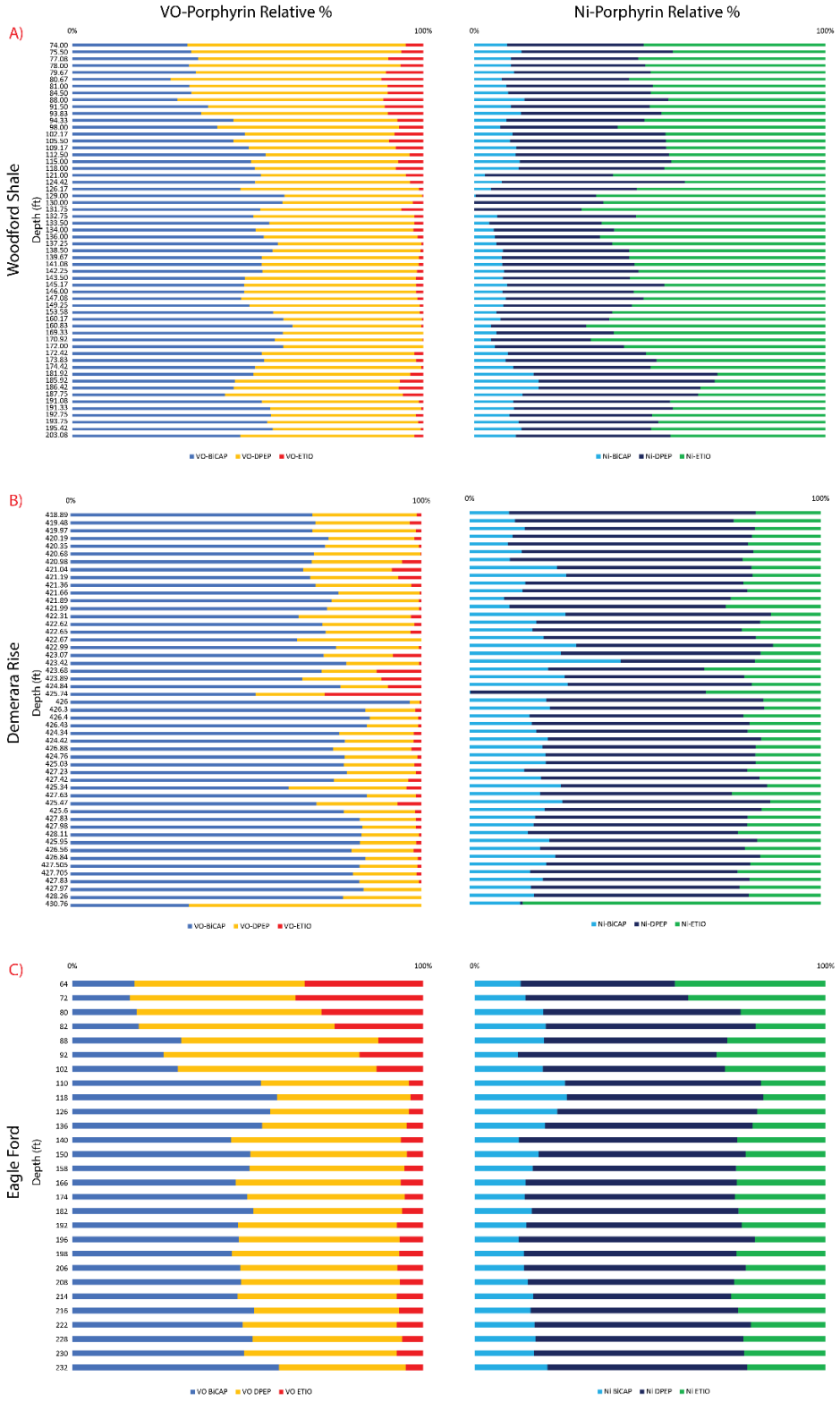


Figure 4.1 Relative percent of vanadyl (VO) and nickel (Ni) porphyrin for A) the Woodford Shale, B) the Demerara Rise, and C) the Eagle Ford.

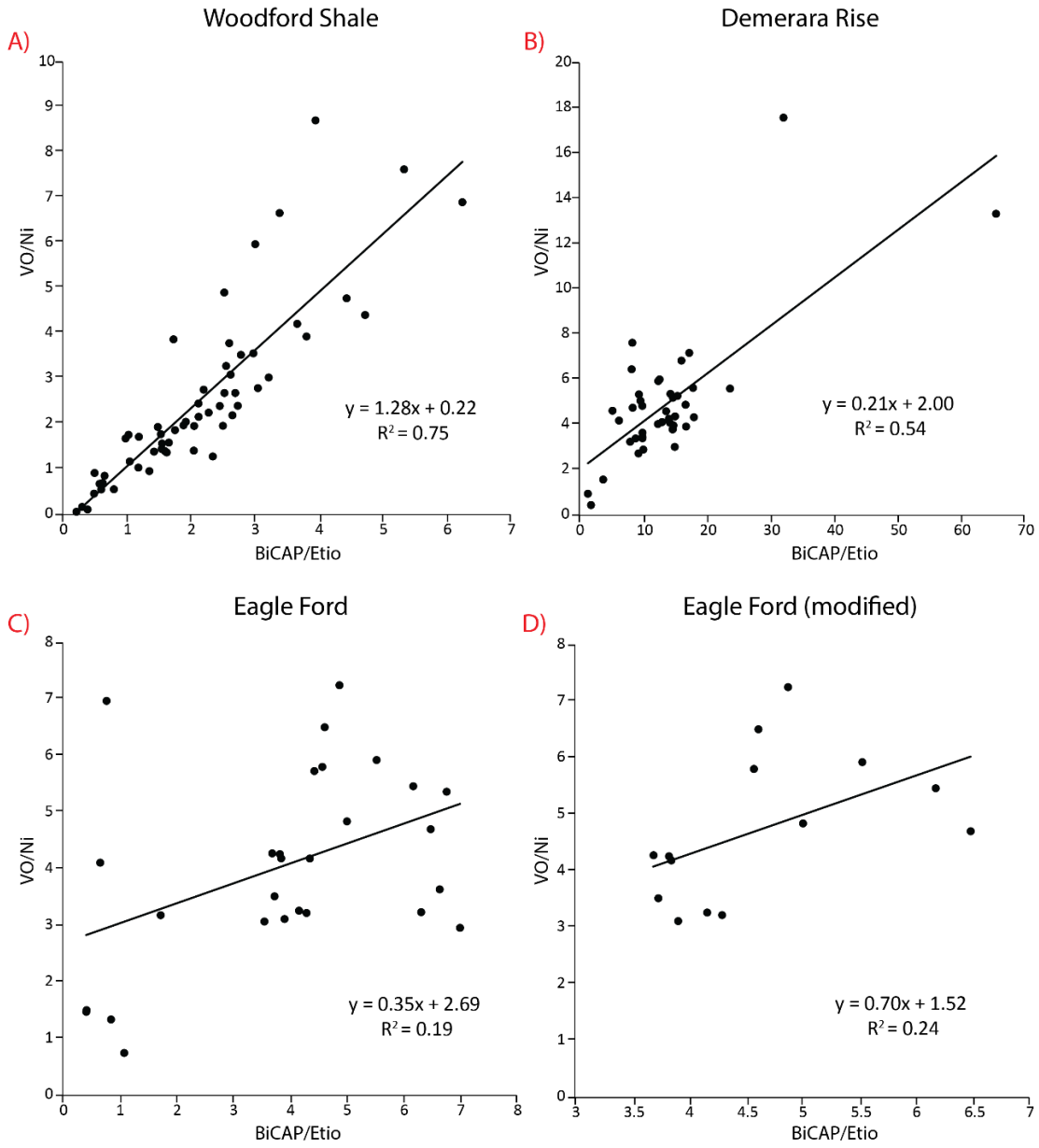


Figure 4.2 Cross plots showing the relationship between the VO/Ni ratio and the BiCAP/Etio ratio for **A)** the Woodford Shale, **B)** the Demerara Rise, **C)** the Eagle Ford, and **D)** the Eagle Ford with samples EF001 (64ft)-EF012 (140ft), EF021 (206ft), and EF024 (206ft) removed.

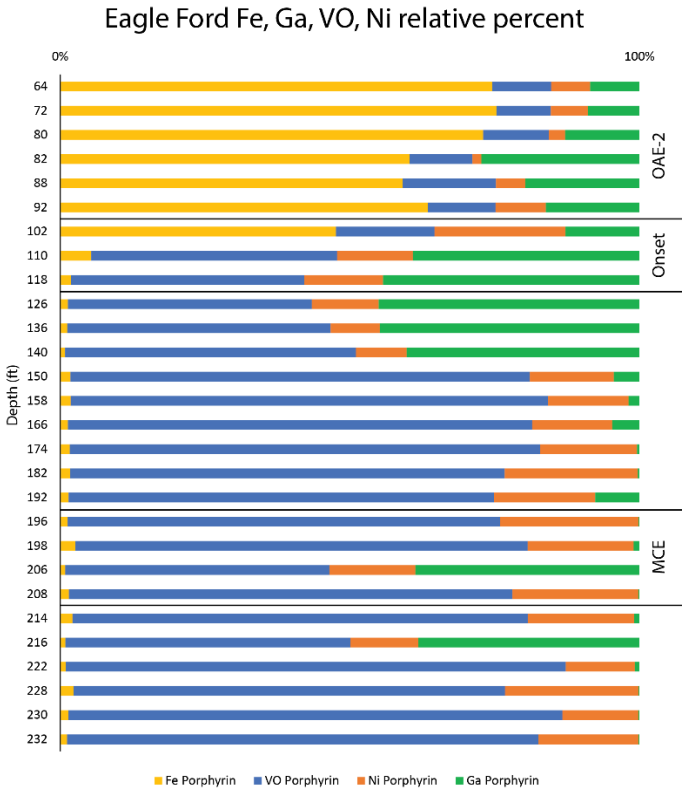


Figure 4.3 Relative percent of all metalloporphyrins detected in the Eagle Ford consisting of iron (Fe), gallium (Ga), vanadyl (VO), and nickel (Ni).

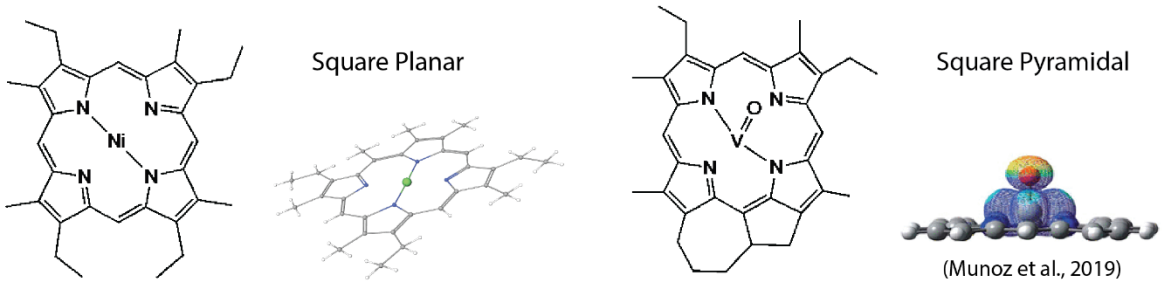


Figure 4.4 Shows the stick structure of Ni-Etio and VO-BiCAP and the theoretical structure of Ni-Etio and the structure of VO chelated to a simple porphyrin (Munoz et al., 2019).

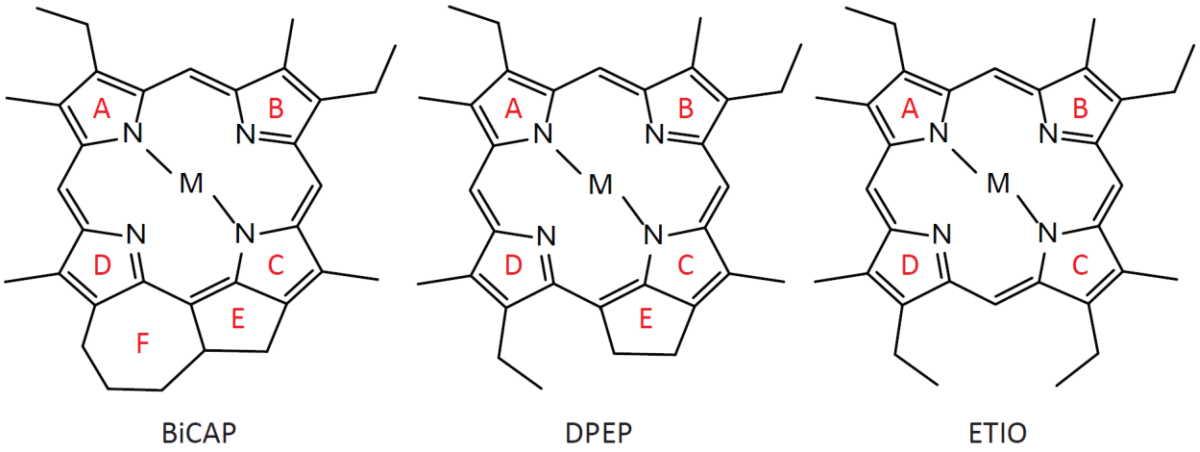


Figure 4.5 General structures and labeled rings for BiCAP, DPEP, and Etio

Concluding remarks and future work

The findings presented in this work highlight the significant advancements enabled by the application of reverse-phase liquid chromatography coupled with quadrupole time-of-flight mass spectrometry (RPLC-ESI-qTOF-MS) in unraveling the complex distributions and interactions of metalloporphyrins in sedimentary black shales. This analytical method's sensitivity and resolution facilitated the unprecedented detection and structural differentiation of vanadyl (VO), nickel (Ni), gallium (Ga), and iron (Fe) porphyrins across multiple stratigraphic intervals including the Woodford Shale, Demerara Rise, and Eagle Ford Formation. A key discovery is the consistent chelation bias exhibited by VO preferentially chelating bicycloalkanoporphyrins (BiCAP) and Ni favoring etioporphyrins (Etio), a phenomenon that potentially could influence traditional interpretations of paleoredox proxies based solely on VO and Ni ratios. This work emphasizes that metalloporphyrin distributions reflect a complex interplay between metal availability, porphyrin molecular structure, depositional redox conditions, and diagenetic pathways, necessitating integration of molecular-level understanding in paleoenvironmental reconstructions.

The elucidation of these chelation biases across diverse depositional environments advances the conceptual frameworks for interpreting biomarker data, providing a more accurate lens through which to assess paleoredox variability and sedimentary chemistry. Inclusion of additional metalloporphyrins such as those complexed with gallium and iron further enriches geochemical understanding, broadening the scope of molecular proxies available for reconstructing ancient environmental conditions. Moreover, coupling these geochemical insights with complementary biomarker classes like carotenoids enhances understanding of microbial community dynamics and photic zone euxinia across geologic timescales.

Future research directions must prioritize expanding the breadth of shale members characterized to better understand the interactions of metalloporphyrins. It would also be useful to attempt to expand the repertoire of characterized metalloporphyrin complexes beyond VO and Ni to include other transition metals that may offer insights into different aspects of porphyrin chemistry and redox conditions. Experimental investigations simulating metalation reactions, degradation pathways, and microbial transformations of porphyrins under controlled environmental conditions are crucial to decipher the biogeochemical mechanisms underpinning these molecular fossils. Isotopic labeling experiments and integration with molecular biology techniques offer promising avenues to link sedimentary metalloporphyrin variations with specific microbial processes and depositional controls.

This dissertation sets a foundation for a more nuanced understanding of metalloporphyrin geochemistry, revealing the importance of molecular structure and metal coordination in interpreting the rock record. It opens pathways for critical refinement of

biomarker proxies that will strengthen interpretations of ancient environmental and redox dynamics, ultimately contribution to more predictive models of Earth's past and future environmental conditions.